Modeling multi-fluid flow over and within porous media: Application of Smoothed Particle Hydrodynamics

Hossein Basser
S.T., M. Eng.

A thesis submitted for the degree of Doctor of Philosophy
at Monash University in 2018
Department of Civil Engineering

Copyright notice

Abstract

Multi-fluid flow over and within porous media occurs frequently in nature and plays an important role in engineering applications, such as seawater intrusion into fresh groundwater aquifers, carbon dioxide migration in groundwater aquifers and oil and water flow in petroleum reservoirs. The discontinuity in the properties of different fluids and the presence of porous media lead to complex behaviours that can be difficult to model. The challenges in modelling these types of flows are tracking the interface between fluids, handling the abrupt discontinuity in the material properties, describing the complex geometries and free surfaces, and dealing with the interaction between the flow and porous media.

There are a number of different numerical methods to solve the equations deriving these flows. In this thesis, Smoothed Particle Hydrodynamics (SPH) is chosen due to its advantages in the mentioned challenges as well as limited number of studies applying SPH to multi-fluid flows in porous media. Therefore, the overarching aim of the thesis is to develop an SPH model of multi-fluid flow in porous media with applications to seawater intrusion. The main objectives are (i) selecting a suitable SPH scheme, (ii) developing a SPH multi-fluid solver in porous media, (iii) and investigating the flexibility of the model in engineering applications.

An Explicit Incompressible SPH scheme (EISPH) and a compressible SPH scheme (δ-SPH) were used to investigate their robustness in modelling fluid flow in porous media. The comparison showed that both schemes led to similar and satisfactory results, with the EISPH scheme producing pressure values closer to theoretical values. Furthermore, EISPH employs physical viscosity term, while δ-SPH uses artificial viscosity and a diffusive term in the continuity equation, which require *ad hoc* numerical parameters. Therefore, EISPH was selected to develop the multi-fluid solver used here for simulating flow in porous media.

EISPH was then applied to simulate multi-fluid lock-exchange over and within porous media. The EISPH method led to results that are overall similar to observed experimental data. The model was able to reproduce the behavior of the flow within media with different

porosities. In addition, the model reproduced behavior of multi-fluid flow at the interface between different fluids, such as reproducing Kelvin-Helmholtz instabilities and diffusion of salt.

The multi-fluid solver was then used to simulate the dynamics of a freshwater lens in an island and saltwater upconing below a groundwater well. The second application required the simulation of groundwater pumping, which needed to introduce a sink term in the continuity equation. The modelling of sinks in SPH is still unexplored, and new methods are then developed.

Specifically, three methods to model water pumping from an aquifer are proposed and compared. The chosen model is tested against data from published laboratory-scale experiments and other numerical models. The inclusion of a sink for water particles to simulate pumping did not affect the stability of the simulations, although one of the three methods led to results that better compared to experimental data.

The results presented in this thesis show that SPH can be used to satisfactory simulate multi-fluid flow across different media. Furthermore, this thesis lays a foundation to use SPH in applications associated with water pumping.

To summarize, the main contributions of this study are i) to combine SPH technique of modeling fluid flow in porous media and multi-fluid flow to generate a model capable of modeling multi-fluid flow in porous media ii) to develop a SPH method to simulate mass sink in a porous medium, with application to water pumping from ground water aquifers.

Declaration

This thesis contains no material which has been accepted for the award of any other degree or diploma at any university or equivalent institution and that, to the best of my knowledge and belief, this thesis contains no material previously published or written by another person, except where due reference is made in the text of the thesis.

Hossein Basser
25 Sep 2018

List of Publications

The following list of publications the lead author of which is the candidate were extracted from the research conducted during PhD candidature i.e. from March 2015 to September 2018. This includes 1 published journal paper in a Q1 journal and 1 other paper submitted to a Q1 journal.

Published Journal Article

SPH modelling of multi-fluid lock-exchange over and within porous media
Advances in Water Resources, Volume 108, Pages 15-28
Basser, H., Rudman, M., Daly, E.

Currently Under Preparation

Smoothed Particle Hydrodynamics modelling of fresh and salt water dynamics in porous media
Submitted to Journal of Hydrology
Basser, H., Rudman, M., Daly, E.

Thesis including published works Declaration

I hereby declare that this thesis contains no material which has been accepted for the award of any other degree or diploma at any university or equivalent institution and that, to the best of my knowledge and belief, this thesis contains no material previously published or written by another person, except where due reference is made in the text of the thesis.

This thesis includes 1 published paper. The core of the thesis is hydraulics. The ideas, development and writing up of all the material in this thesis were the principal responsibility of myself, the candidate, working within the Department of Civil Engineering under the supervision of Dr. Edoardo Daly and Prof. Murray Rudman.

In the case of Chapters 4, my contribution to the work involved the following:

Chapter	**Publication title**	**Publication status**	**Nature and % of student's contribution**	**Co-author name(s), Nature and % of Co-author's contribution**	**Co-author Monash student**
4	SPH modelling of multi-fluid lock-exchange over and within porous media	Published: Advances in Water Resources, 2017.	Development of ideas; Establishing methodologies; Analysis,; Write-up and revision 60%.	1. Dr. Edoardo Daly: developing ideas, input into manuscript, revision, 30%. 2. Prof. Murray Rudman: developing ideas, input into manuscript, revision, 10%. .	No

I have not renumbered sections of the published paper in order to generate a consistent presentation within the thesis.

Student signature: Hossein Basser Date: 01/10/2018

The undersigned hereby certify that the above declaration correctly reflects the nature and extent of the student and co-authors' contribution to this work.

Main Supervisor signature: Edwards Daly Date: 09/10/2018

Acknowledgements

Hereby I would like to acknowledge support of people who helped me during this exciting journey and preparation of this thesis. To Dr. Edoardo Daly and Prof. Murray Rudman, my supervisors, I extend my profound appreciation for their professional guidance throughout this research program. I also would like to thank my previous supervisor, Dr. Chunhui Lu for his support at initial stage of my PhD.

I would like to extend my sincere gratitude to Dr. Alireza Valizadeh, Dr. Ha Hong Bui and Dr. Vincent Lemiale for being part of my panel committee and for their professional comments.

I would like to thank Prof J. J. Monaghan for useful discussions.

I am also indebted to the Monash University's scholarships; Monash Graduate Scholarships, and Monash International Postgraduate Research Scholarships, for the financial support in diverse ways. This research would not have been possible without financial support from Monash.

I also thank my colleagues and friends for academic-related discussions and their support during the past 4 years.

Finally, I would like to express my heartfelt gratitudes to my beloved family, especially my wife; who supported me during this journey.

Table of Contents

Page

List of Figures **xv**

1 Introduction **1**

2 Literature review, research gaps and aims **5**

2.1 Fluid flow over and within porous media 5

2.1.1 Governing equations 6

2.1.2 Numerical simulations 11

2.2 Multi-fluid flow 13

2.2.1 Governing equations 14

2.2.2 Numerical simulation of multi-fluid flow 16

2.3 Research gaps 17

2.4 Aims 18

3 An overview of Smoothed Particle Hydrodynamics **21**

3.1 Governing equations 21

3.2 SPH formulations 22

3.2.1 Spatial volume 24

3.2.2 Kernel function 25

3.3 SPH approximations 27

3.3.1 Continuity equation for an incompressible fluid 28

3.3.2 Continuity equation for a compressible fluid 28

3.3.3 Momentum equation 29

3.3.4 Diffusion equation 30

3.4 Boundaries 31

3.4.1 Solid boundaries 31

3.4.2 Free and no slip boundary conditions 32

3.4.3 Free surface . . . 32
3.4.4 Interface conditions . . . 33
3.4.5 Inflow boundaries . . . 34
3.5 Particle search . . . 34
3.5.1 All pair search . . . 35
3.5.2 Linked list algorithm . . . 36
3.6 Numerical schemes . . . 36
3.6.1 EISPH . . . 37
3.6.2 δ-SPH . . . 41
3.7 A comparison between EISPH and δ-SPH . . . 42
3.7.1 Vertical percolation into a porous medium . . . 42
3.8 Sink approximations . . . 47
3.8.1 Solely Particle Removal (SPR) . . . 48
3.8.2 Mass Reduction and Particle Removal (MRPR) . . . 48
3.8.3 Constant Mass Reduction (CMR) . . . 49

4 SPH modelling of multi-fluid lock-exchange over and within porous media 51
4.1 Introduction . . . 51
4.2 Published paper . . . 52
4.3 Additional results . . . 67
4.3.1 Comparing EISPH results with an analytical solution . . . 68
4.3.2 Normal stress continuity . . . 70
4.4 Conclusion . . . 72

5 Applications of the multi-fluid SPH solver in porous media 75
5.1 Introduction . . . 75
5.2 Submitted paper . . . 75
5.3 Summary . . . 113

6 Conclusions 115
6.1 Thesis limitations . . . 118
6.2 Future works . . . 119
6.2.1 Interface between media with different porosities . . . 119
6.2.2 Sink simulations . . . 121

Bibliography 123

List of Figures

Figure **Page**

2.1 Velocity profile above and within the porous medium assumed by *Beavers and Joseph* (1967). 7
2.2 Actual velocity profile for a coupled parallel flows in a channel and a porous medium (*Neale and Nader*, 1974). 8
2.3 Averaging volume of a system consisted of solid and fluid phases (*Whitaker*, 1986). 9
2.4 Schematic view of a lock-exchange flow (*Rotunno et al.*, 2011). 14

3.1 Spatial volume of a particle within a (a) free flow domain ($\epsilon = 1$) and (b) a porous medium, (c) volume of fluid within a particle (*Pahar and Dhar*, 2016a). 25
3.2 Support domain of the kernel function, with radius λh, for particle i. 26
3.3 The (a) cubic and (b) quintic, kernel functions and their derivatives used in this study (*Liu and Liu*, 2003). 27
3.4 Schematic representation of (a) virtual, fluid and ghost particles (Ghost particles are only shown for the fluid particles adjacent to the lower horizontal solid boundary), and (b) application of free-slip and no-slip boundary conditions. 33
3.5 Definition of the transition layer between a free flow and a porous medium with porosity ϵ_m. The depth of the transition layer, δ_ϵ, equals the diameter of the support domain of the kernel function, $2\lambda h$. 34
3.6 Schematic view of an inflow boundary condition. 35
3.7 A schematic view of the all-pair search algorithm to find the nearest neighbouring particles to approximate the variables in particle i (Section 3.5.1). . 35
3.8 (a) Link list and (b) the improved linked list algorithm to find the nearest neighbouring particles (Section 3.5.2). 36
3.9 (a) Schematic view of the experimental tank. (b) The extension of the fluid from the free flow domain to the porous medium and the theoretical pressure distribution (Section 3.7.1) 43

3.10 Simulated pressure distribution in the column of glycerine percolating through a porous medium 0.25 m deep with a) EISPH and b) δ-SPH. 45
3.11 Comparison of the time evolution of pressure between EISPH and δ-SPH at (a) 0.02 m above and (b) 0.02 m below the porous medium. 46
3.12 (a) Time evolution of drainage of glycerine over the porous medium and (b) porosity times percolated depth of glycerine within the porous medium in the test case in Fig. 3.10 46
3.13 The procedure for the reduction of mass due to a sink point using (a) Solely Particle Removal (SPR), (b) Mass Reduction and Particle Removal (MRPR) and (c) Constant Mass Reduction (CMR). 49

4.1 Non-dimensional remaining mass of the current over the porous medium, with smoothing length varying in different media 67
4.2 Schematic view of the case study in section 4.3.1 (*Peng et al.*, 2017; *Khayyer et al.*, 2018). 69
4.3 Pressure distribution for different hydraulic conductivity values, and at different times, section 4.3.1. (The snapshots are shown at different times for different hydraulic conductivities to present an equal head difference between the left and right tubes) 70
4.4 Comparison of the EISPH time evolution of the water level difference with the analytical solution in Eq. (4.1), Enhanced ISPH (*Khayyer et al.*, 2018) and WCSPH (*Peng et al.*, 2017), as a function of time for hydraulic conductivity of a) 0.001, b) 0.005, c) 0.01 and d) 0.05, section 4.3.1. 71
4.5 Comparison of the EISPH time evolution of the water level difference with the analytical solution in Eq. (4.1), as a function of time for different initial particle spacing, section 4.3.1. 72
4.6 Pressure distribution around the interface between the free flow domain and the porous medium 72
4.7 Time evolution of the pressure values 1 mm above and below the interface. . 73

6.1 Kernel function summation (W_s) for the scenario with (a) constant smoothing length, (b) variable smoothing length. 120
6.2 A sink at the origin (*Nakayama*, 2018). 122

CHAPTER 1

Introduction

Multi-fluid flow occurs in a wide range of industrial and natural processes. These flows mostly occur over and within porous media and play an important role in engineering applications. For example, the interaction between stream-flow and a river bed affects flow structure over the bed, solute and heat transfer, and river ecosystem. Flow in porous media is important in engineering applications, such as irrigation, seawater intrusion, and transport of contaminants following their spillage over a porous medium.

In a multi-fluid flow, heterogeneity often arises from the variation of fluid density and viscosity. Density variation may be due to differences in temperature or salinity. A common example of a multi-fluid flow is the lock-exchange gravity current, which usually results from flow of two fluids with different densities (*Simpson*, 1982; *Huppert*, 2006). This flow often occurs over or within porous media in situations such as a freshwater river flowing into an ocean, oil spills on water bodies, sea-water intrusion in groundwater, and water treatment (*Zhao et al.*, 2013; *Meiburg et al.*, 2015). Several factors govern the hydrodynamics of multi-fluid flows in porous media, i.e. gravity and pressure-gradient forces, viscous and turbulent stresses, diffusion, surface-tension, and flow characteristics at the interface between the free flow and the porous medium (*Rotunno et al.*, 2011; *Thomas and Marino*, 2011).

A discontinuity in the fluid properties (e.g. density, viscosity, or temperature) at the interface between fluids can cause a great deal of complexity from a mathematical and computational perspective. Furthermore, extra complexities are added by the presence of

porous media and the porous materials interaction with the fluid system. Tracking the interface between phases and the description of complex geometries and free surfaces are also challenging in modelling multi-fluid flow in porous media. The methods most commonly used for simulating multi-fluid flows are grid-based, such as the finite-difference method (FDM) and the finite volume method (FVM) (*Birman et al.*, 2005; *Bonometti and Balachandar*, 2008). However, grid-based methods lead to difficulties in generating complex grids, modelling free surfaces and interfaces between different phases, and deformable boundaries (*Liu and Liu*, 2003). Mesh-free numerical methods represent an alternative. A variety of mesh-free numerical methods have been developed, such as the molecular dynamics method (*Li et al.*, 2010), discrete element method (*Yeganeh-Bakhtiary et al.*, 2009), the moving least squares method (*Shobeyri and Afshar*, 2010), and Smoothed Particle Hydrodynamics (*Gingold and Monaghan*, 1977). In a particle method, the computational domain is filled with a set of particles and each particle carries fluid or solid properties such as density, viscosity, and velocity. The governing equations drive the dynamics of particles and their properties. Compared with grid based methods, particle methods facilitate tracking free surface and interfaces between different fluids and media (*Shao*, 2012; *Akbari*, 2014).

The SPH method is a fully Lagrangian meshless method which has reached a certain degree of maturity, showing acceptable accuracy for a wide range of applications from fluid flow dynamics to astronomical studies (*Liu and Liu*, 2003).

In SPH, treating the fluid as either weakly-compressible or incompressible, led to development of different schemes that employ different approaches in predicting flow's pressure field (*Monaghan*, 1994; *Cummins and Rudman*, 1999; *Hosseini et al.*, 2007; *Molteni and Colagrossi*, 2009). Although recent studies have improved the prediction of the pressure field in weakly-compressible SPH scheme (WCSPH) (*Molteni and Colagrossi*, 2009), the incompressible schemes (ISPH) have been proven to produce a more accurate flow pressure field (*Violeau and Rogers*, 2016). However, ISPH schemes require larger computational time as the Poisson equation should be solved implicitly (*Nomeritae et al.*, 2016). To tackle this problem, explicit incompressible SPH (EISPH) that solves the Poisson equation approximately has been proposed and tested in various applications (*Hosseini et al.*, 2007; *Rafiee and Thiagarajan*, 2009; *Nomeritae et al.*, 2016; *Bui and Nguyen*, 2017; *Nomeritae et al.*, 2018).

SPH has been used to simulate multi-fluid flows owing to its advantages in tracking free surfaces and multi-interfaces (*Shao*, 2012). SPH has also been employed to model fluid flow in porous media (*Shao*, 2010; *Akbari and Namin*, 2013). Progresses in employing

SPH in porous media have led to a corrected SPH algorithm, focusing on the behaviour of the flow moving between different media (*Akbari*, 2014). However, this algorithm needs strong validation against experimental observations. Despite the increasing interest in SPH for modelling multi-fluid flows and fluid flow in porous media, the simultaneous modelling of a multi-fluid flow that occurs over or within a porous medium has not been comprehensively studied. Developing a method to simulate multi-fluid flows in media with different porosities is important to study natural and man-made events, such as seawater intrusion in groundwater (*Zhao et al.*, 2013) and oil recovery through water flooding in petroleum reservoirs (*Coutinho et al.*, 2008).

Although large computational time is one of the drawbacks of SPH, the rapid progress in computation technology, such as the development of Graphics Processing Units (GPUs), has made it possible to use SPH in the larger scale problems (*Violeau and Rogers*, 2016). Therefore, it is worthwhile developing an SPH multi-fluid solver and applying it to environmental and engineering problems such as salt and fresh water dynamics in coastal zones, and seawater upconing in freshwater aquifers (*Werner et al.*, 2009; *Stoeckl and Houben*, 2012; *Stoeckl et al.*, 2016).

The overarching aim of the present study is to bring together SPH schemes for multi-fluid flow and flow in porous media to generate a model capable of simulating multi-fluid flow in porous media at scales significantly larger than pore scale. Furthermore, this study aims to apply the SPH model to applications such as freshwater and salt water dynamics in aquifers and salt water upconing below pumping wells.

This thesis comprises six chapters. A detailed literature review of the progress in the modelling of flow in porous media and multi-fluid flow as well as research gaps and aims are presented in Chapter 2. Chapter 3 includes the overview of the numerical schemes applied in this study. In Chapter 4, the applicability of the numerical schemes in modelling flow in porous media is investigated. Chapter 5 includes a published paper that links modelling approaches of flow in porous media and multi-fluid flow to generate a model capable of simulating multi-fluid flow in porous media. Chapter 6 includes a submitted paper that presents the simulations of two engineering application (freshwater lens formation in an island and upconing of salt water in a freshwater aquifer). Chapter 7 summarises the key findings, highlights the limitations of this study and proposes opportunities for future studies.

CHAPTER 2

Literature review, research gaps and aims

Numerous experimental and analytical studies have been conducted to study multi-fluid flow in porous media. Because computational modeling is focus of the thesis, this chapter focuses on the studies that have employed numerical techniques to model these flows. Readers are referred to *Werner et al.* (2013) and *Werner et al.* (2017) for comprehensive review of experimental and analytical studies. Significant effort has been dedicated to the modeling of gravity currents with multi-fluid flows in porous media; however, less work has been devoted to multi-fluid flows over and within porous media. Thus, to understand the theoretical background and modeling approaches of such flows, this review focuses on studies of fluid flow across media with different porosities and multi-fluid flow. Mathematical modeling to develop governing equations and numerical modeling techniques applied to both types of flows are described. Subsequently the research gaps and the aims of the thesis are presented.

2.1 Fluid flow over and within porous media

Fluid flow in the environment often occurs over porous media and interact with the flow within the porous media. For example, in engineering applications, water flows in streams that is affected by the porous bed, and groundwater in coastal aquifers that is influenced by interaction with seawater. To study the physics of these applications, one of the main approaches is numerical modeling. To facilitate modeling these flows many studies have developed governing equations and numerical techniques to discretize the equations. One

of the main challenges with modeling these flows is handling the boundary conditions at the interface between a porous medium and outside the porous medium to match the velocity and stress (*Beavers and Joseph*, 1967).

2.1.1 Governing equations

One of the first studies focused on fluid flow through porous media was published by Darcy, and is applied to numerous practical applications. He investigated the flow of water through a layer of sand and concluded that for creeping flows, the average flow rate passing through the layer is proportional to the pressure gradient across the layer and the constant of proportionality representing the hydraulic conductivity of the layer (*Bear*, 2013). Although Darcy's law has been found effective in many practical applications, it has been found necessary to extend it for more complex circumstances, especially for the case when flow might happen across the boundary of a porous medium and outside the porous medium (i.e., a free flow domain) (*Acton et al.*, 2001). This task has led to a wide range of modeling approaches for predicting fluid behaviour over and within porous media, that can be categorised into two approaches, i.e. two-domain and single-domain.

2.1.1.1 Two-domain approach

In the two-domain approach, a separate set of equations is defined in each domain with coupling term at the interface. One of the early investigations associated with this approach was the study of *Beavers and Joseph* (1967). They used the Poiseuille flow equation and Darcy's Law to formulate the solution method. Fig. 2.1 shows the assumed velocity profiles over and within the porous medium. The Poiseuille law assumes a smooth laminar flow and it is governed by pressure gradient and viscous force. To couple the Poiseuille and Darcy laws, *Beavers and Joseph* (1967) proposed a semi-empirical condition at the interface between the porous and free flow domains. The Poiseuille equation reads

$$\mu \frac{\partial^2 u}{\partial y^2} = \frac{\partial p}{\partial x}, \tag{2.1}$$

with the boundary conditions

$$u = 0 \qquad \text{at} \qquad y = h,$$

$$\frac{\partial u}{\partial y} = \frac{\alpha}{\sqrt{\kappa}}(u_i - U) \qquad \text{at} \qquad y = 0.$$

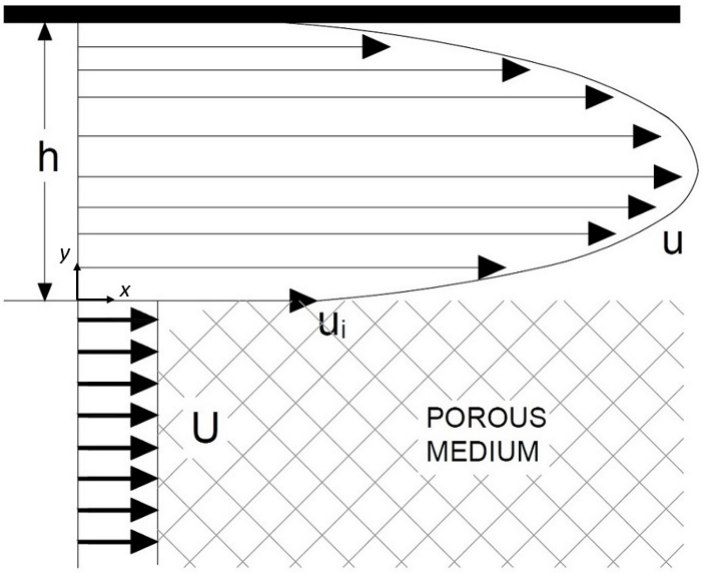

Figure 2.1: Velocity profile above and within the porous medium assumed by *Beavers and Joseph* (1967).

Here u is velocity, p is pressure, μ is the dynamic viscosity of the fluid, κ is the permeability of the porous medium, α is an empirical dimensionless quantity experimentally obtained, u_i is the slip velocity at the interface between the free flow domain and the porous medium, and U is the Darcy velocity, i.e. the volume flow rate per unit area. The Darcy equation for a flow through a homogeneous, isotropic permeable bed is written (*Bear*, 2013)

$$U = -\frac{\kappa}{\mu}\frac{\partial p}{\partial x}. \tag{2.2}$$

The solution of Eq. (2.1) leads to a velocity profile in the free flow domain as

$$u = -\frac{\kappa}{2\mu}\left(\frac{\sigma^2 + 2\alpha\sigma}{1+\alpha\sigma}\right)\frac{\partial p}{\partial x}\left(1 + \frac{\alpha}{\sqrt{\kappa}}y\right) + \frac{1}{2\mu}\left(y^2 + 2\alpha y\sqrt{\kappa}\right)\frac{\partial p}{\partial x}, \tag{2.3}$$

where $\sigma = h/\sqrt{\kappa}$. Eq. (2.3) correlated well with the experimental data (*Beavers and Joseph*, 1967). Several studies attempted to determine the empirical parameter α which has been proven to be dependent on the geometry of the interface rather than the fluid's parameters (*Goyeau et al.*, 2003; *Richardson*, 1971).

Neale and Nader (1974) questioned the physical validity of the approach employed by *Beavers and Joseph* (1967) because the actual velocity profile within the porous medium

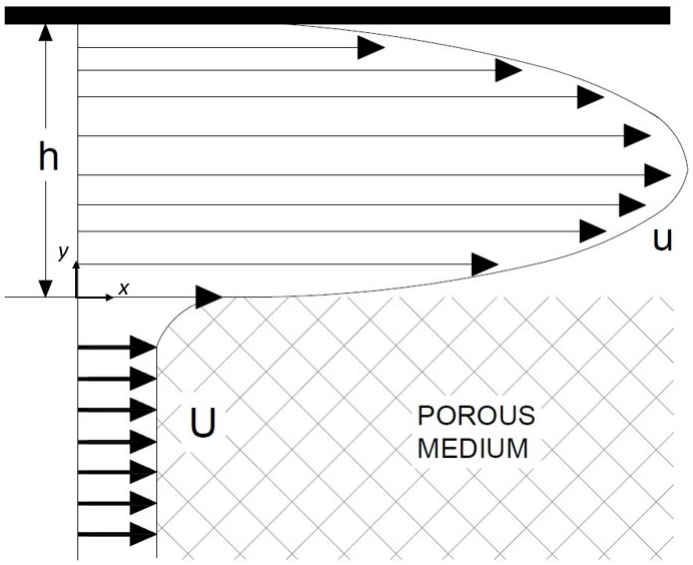

Figure 2.2: Actual velocity profile for a coupled parallel flows in a channel and a porous medium (*Neale and Nader*, 1974).

contains a boundary layer region and the discontinuity of the velocity across the interface between the free flow domain and the porous medium is not physically realistic (see Fig. 2.2). *Neale and Nader* (1974) proposed the Brinkman's extension of Darcy's Law to be applied as the shear term in Eq. (2.2); Brinkman's extension is better suited for the boundary layer at the interface and reads

$$0 = -\nabla p + \mu_{eff}\nabla^2 u - \mu\kappa^{-1}u, \tag{2.4}$$

where u hereafter denotes the local averaged velocity, ρ is density of fluid, μ_{eff} is effective dynamic viscosity which is dependent on porosity and the fluid's dynamic viscosity. The second term on the right hand side of the Eq. (2.4) represents the Brinkman's extension, and its shear nature improves the Beaver and Joseph's approach by providing a boundary layer region at the interface. The boundary layer thickness is of order $\sqrt{\kappa}$. Although the boundary layer at the interface within the porous medium is usually insignificant, it can considerably affect flow in the free flow domain, above the porous medium (*Neale and Nader*, 1974). The shear term outside the boundary layer region is insignificant, and Darcy's original law is applicable (*Neale and Nader*, 1974).

To capture macroscopic, rather than microscopic, behaviour of a flow above and within a porous medium, some studies focused on volume averaging of the momentum

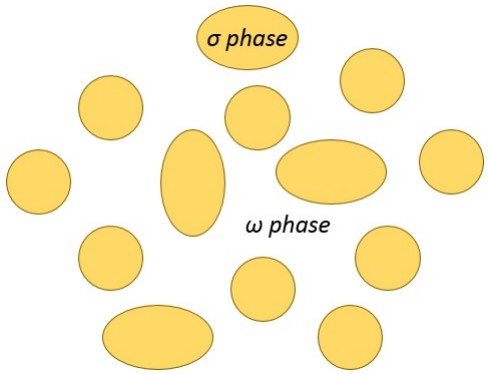

Figure 2.3: Averaging volume of a system consisted of solid and fluid phases (*Whitaker*, 1986).

equation. *Whitaker* (1986) developed a volume averaged momentum equation for a flow within a homogeneous porous medium using the Brinkman's extension. *Whitaker* (1986) considered two types of averaging methods. In the first, averaging is carried out over the whole averaging volume, consisting of fluid and solid materials (Fig. 2.3), and is called phase or superficial averaging, while in the second, the averaging is carried out only over fluid phase, ω-phase (Fig. 2.3), and is called intrinsic averaging. These two averaged values are related by the porosity according to

$$\langle \psi \rangle = \epsilon \langle \psi \rangle^{\omega}, \tag{2.5}$$

where ϵ is porosity, and $\langle \psi \rangle$ and $\langle \psi \rangle^{\omega}$ represent superficial and intrinsic value of a function, respectively.

A volume-averaged momentum equation within a porous medium was developed by adding the Forchheimer correction to Brinkman's extension, which accounts for the drag force associated with inertial effects (*Whitaker*, 1996) as

$$0 = -\nabla \langle p_{\omega} \rangle^{\omega} + \rho_{\omega} g + \mu_{\omega} \nabla^2 \langle v_{\omega} \rangle^{\omega} - \frac{\mu_{\omega}}{K} \langle v \rangle - \frac{\mu_{\omega}}{K} F \langle v_{\omega} \rangle, \tag{2.6}$$

where g is the acceleration due to gravity, $\langle v_{\omega} \rangle$ is the superficial averaged or Darcy seepage velocity, $\langle v_{\omega} \rangle^{\omega}$ is intrinsic averaged velocity, $\langle p_{\omega} \rangle^{\omega}$ is the intrinsic averaged pressure and K and F are permeability and Forchheimer tensors, respectively. Intrinsic averaged pressure was used in Eq. (2.6) as it is the pressure that can be measured by a probe in

an experimental apparatus (*Scarselli*, 2013). The volume averaged equations derived by Whitaker were applicable to a flow that occurs in a porous medium.

Brinkman's extension to Darcy's law proposed by *Neale and Nader* (1974) has been the most employed equation to describe flow in porous media. However, it has also been a topic of extensive controversy, especially in its description of the interface. To model a porous medium and a free flow domain interface there needs to be four matching conditions (*Nield*, 1991), because the Navier-Stokes and Brinkman equations both have second order derivatives. These four conditions are continuity of normal and tangential velocity and stress. Although the velocity components are continuous functions at the interface, the tangential viscous stress has a discontinuity at the solid sections of the interface. The tangential shear stress is zero over the solid section, while it is non zero in the clear fluid. *Nield* (1991) also mentioned that the situation of viscous normal stress is somewhat similar to that of the tangential stress.

In two-domain approaches, a jump condition in stress is often employed along with the governing equations to handle the discontinuity of stress at the interface (*Ochoa-Tapia and Whitaker*, 1995). The jump condition often includes a parameter that must be obtained experimentally. Furthermore, solving two sets of equations for two different regions requires a boundary condition at the interface between the regions (*Valdés-Parada et al.*, 2013). In addition, determination of the thickness of the transition layer, also requires experimental measurements (*Goharzadeh et al.*, 2006). Due to these challenges, the single-domain approach is considered in some studies.

2.1.1.2 Single-domain approach

In the single-domain approach the free flow domain and the flow in the porous medium are considered to be driven by the same equations with different parameters dependent on the medium (*Tao et al.*, 2013). The transition from the free flow to the porous medium is treated through variation of properties in the equations, such as permeability and porosity (*Goyeau et al.*, 2003). Therefore, there is no need to explicitly formulate boundary conditions at the interface. The momentum equation for flow in a domain consisting of free flow and a porous medium is given as (*Goyeau et al.*, 2003)

$$\epsilon^{-1}\frac{\partial(\rho u)}{\partial t} + \epsilon^{-2}\nabla\cdot(\rho u u) = -\nabla p + \mu\nabla^2 u + \rho g - \mu\kappa^{-1}u. \tag{2.7}$$

According to Eq. (2.7), in the space associated with a free flow domain the porosity is 1 and permeability is infinite, so that the drag term becomes zero and Eq. (2.7) becomes the Navier-Stokes equations (*Goyeau et al.*, 2003).

In the single-domain approach, the change in properties (i.e., porosity and permeability) in an interface between a porous medium and a free flow domain is defined in different ways such as sharp or gradual change. The variation of flow in the interface does not have a general solution and is still an open research area. Experiments are usually required to investigate the geometry of the interface, to formulate variation of porosity and permeability (*Duman and Shavit*, 2010).

Due to its simplicity, this approach, has been widely employed in engineering applications, such as heat or solute and mass transfer, and erosion (*Gobin et al.*, 2005; *Valdés-Parada et al.*, 2007; *Panah and Blanchette*, 2018).

The single-domain approach also has been the platform in studies associated with particle methods such as SPH, due to their Lagrangian nature. As the particles tend to travel throughout a domain, it is intuitive to assign parameters to a particle, in accordance with the domain in which it resides, and solve a unified governing equation.

Pahar and Dhar (2016b) derived the Lagrangian form of the momentum equation for flow across different media as

$$\frac{Du}{Dt} = -\frac{\epsilon}{\rho}\nabla p + \nu\nabla^2 u + \epsilon\vec{g} - \frac{\epsilon\mu}{\rho\kappa}u - \frac{\epsilon c_F}{\kappa^{1/2}}|u|u, \tag{2.8}$$

where the last term on the right hand side is the Forchheimer quadratic drag term that accounts for an inertial drag when the pore scale Reynolds number is higher than unity (*Joseph et al.*, 1982; *Nield*, 2000); c_F is the dimensionless Forchheimer coefficient that is obtained experimentally (*Pahar and Dhar*, 2016a).

2.1.2 Numerical simulations

2.1.2.1 Grid based methods

Grid based, Eulerian methods, have been extensively used to simulate fluid flow in porous media. These methods are the basis of many powerful tools. Grid based methods suffer from drawbacks such as the need to update grid continuously to cover the area when the fluid flows; additionally tracking free surfaces and interfaces is computationally expensive (*Liu and Liu*, 2003). A method such as volume of fluid (VOF) is usually used to track free surfaces (*Del Jesus et al.*, 2012; *Hu et al.*, 2012; *Raeini et al.*, 2012). A problem with VOF is the production of artificial numerical diffusion and free surface smearing. Therefore, a reconstruction method is often used to reconstruct the free surface throughout a simulation (*Park et al.*, 2005).

Del Jesus et al. (2012) and *Hu et al.* (2012) studied the interaction of a dynamic wave with porous media. They studied fluid motion across heterogeneous media with variable porosity and used VOF to track the free surfaces, where variation density was detected to track the position of the interface (*del Jesus*, 2011). In addition an interface reconstruction technique (*Kothe et al.*, 1999) was used to reconstruct the interface.

2.1.2.2 SPH simulations

With progress in particle methods such as SPH and their advantages in handling interfaces, they have attracted an increasing interest in modeling flow in porous media. The Lagrangian nature of the method facilitates modeling free surface flows without the extra procedure of tracking and moving the interface.

Due to the potential advantages of projection-based particle methods, such as incompressible-SPH (ISPH), with higher accuracy in calculating pressure values and conservation of volume, most SPH studies dedicated to flow in porous media have used the projection-based methods.

In SPH, solid particles, fixed at their location or moving, are often employed to represent porous media. The drag force due to the presence of the porous material is accounted for by interaction of solid and fluid particles (*Bui et al.*, 2007; *Jiang et al.*, 2007; *Grabe and Stefanova*, 2014). For moving solid particles, an extra set of equations are used (*Bui et al.*, 2007; *Bui and Nguyen*, 2017). Using two sets of particles (i.e., solid and fluid) requires extra computational cost, as different sets of equations must be solved and extra interactions are required between particles. The use of solid particles is required when the medium can move, as in problems related to erosion, and landslides.

When the medium is fixed, to avoid the extra time imposed by the presence of the solid particles, a drag force can be explicitly imposed on the particles that enter the porous medium. This approach has been used in SPH for applications such as wave interaction with porous media (*Shao*, 2010), and is often employed in other modelling methods (*Goyeau et al.*, 2003).

Recently, a new SPH approach has been developed (*Akbari and Namin*, 2013; *Pahar and Dhar*, 2016a) to simulate free surface flow moving across media with different porosities. In this method, the density or volume of a particle is adjusted according to the porosity of media and SPH approximations are modified accordingly. In this method, the equations are solved mostly with incompressible-SPH (ISPH) schemes (*Aly and Asai*, 2015; *Pahar and Dhar*, 2016a), requiring large computational time due to the implicit solution of the pressure Poisson equation (PPE). For weakly-compressible

(WCSPH) schemes, limited studies have been conducted to validate the equivalent approach (*Ren et al.*, 2016). This approach has been employed in different applications, such as wave interaction with porous structures (*Akbari and Namin*, 2013), fluid flow through porous dams (*Aly and Asai*, 2015; *Pahar and Dhar*, 2016a) and lock-exchange flow through a porous medium (*Pahar and Dhar*, 2017). In this method, smoothing length is recommended to be adjusted for particles moving across different media (*Pahar and Dhar*, 2017). To conserve momentum, smoothing lengths of a pair of interacting particles need to be averaged (*Rafiee et al.*, 2007).

Peng et al. (2017) used WCSPH with mixture theory to simulate fluid flow in porous media. They used solid particles to carry porosity of the media. In a similar approach, *Khayyer et al.* (2018) implemented an enhanced ISPH projection method capable of simulating fluid flow across media with different porosities. The method calculates volume fraction of fluid and porous material consistently, using two-phase mixture theory, to reproduce fluid flow interactions with spatially varying porous media. The effect of porous media is incorporated through a resistance force. The method is capable of satisfying pressure and velocity continuity as well as volume conservation at interface between fluid and porous media without any interface boundary condition.

2.2 Multi-fluid flow

Multi-fluid flow refers to any flow consisting of more than one fluid. Multi-fluid flow frequently occurs in nature and plays a crucial role in a variety of engineering fields and industrial processes, such as air entrainment at the ocean surface, cavitation, rising of a air bubble in a viscous liquid, and gravity current of two or more fluids intruding into each other under gravity (*Huppert*, 2006; *Rotunno et al.*, 2011; *Zainali et al.*, 2013). Due to this importance, there is a necessity to model and predict the detailed behaviour of these flows. They have been studied experimentally, through laboratory models, theoretically, through mathematical modeling, and computationally (*Brennen and Brennen*, 2005). Experimental methods are not applicable for most practical scales, and reliable mathematical and computational techniques are required for extrapolation of laboratory scales to the prototype scale. Alongside several experimental and theoretical studies dedicated to multi-phase flows (*Britter and Linden*, 1980), numerical studies, which mostly solve the Navier-Stokes equations, have provided an efficient way to study multi-fluid flows.

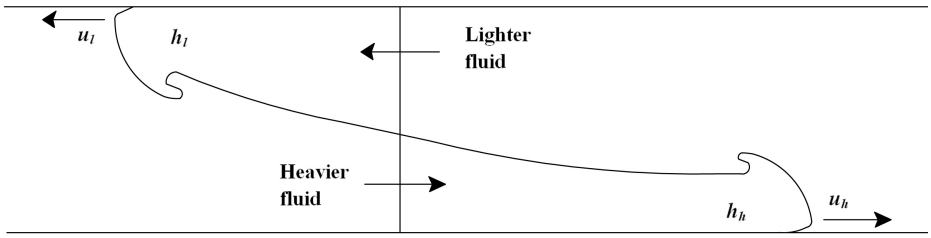

Figure 2.4: Schematic view of a lock-exchange flow (*Rotunno et al.*, 2011).

2.2.1 Governing equations

The lock-exchange gravity current is a common example of multi-fluid flows that has attracted a wide research interest, since it can be encountered in several engineering applications. Herein, the governing equations employed to study these flows are explained, because gravity currents are used in this study to validate the multi-fluid model. Gravity currents result from two fluids with different densities, due to difference in salinity or temperature. In this current, a denser fluid usually flows under a lighter fluid and pushes the lighter fluid up. This phenomenon occurs frequently in the environment (e.g. turbidity currents occurring under a sea, avalanches, lava flows, dam break, and salt wedge propagation) (*Adduce et al.*, 2011).

A schematic diagram of a lock-exchange gravity current is shown in Fig. 2.4. Based on the ratio of density of lighter, ρ_l, to heavier fluid, ρ_h, the lock-exchange gravity currents are classified as Boussinesq ($\rho_l/\rho_h \approx 1$) and non-Boussinesq ($\rho_l/\rho_h < 1$). For Boussinesq flow, both heavy and light gravity currents propagate at nearly the same velocity and depth. For non-Boussinesq flow, the heavy current propagates faster than the light current, and the depth of the heavy current reduces to fulfil the conservation of volume.

A frequently used set of equations for studying lock-exchange problems, using the description of the long wave of expansion, is solving the two-layer shallow-water equations (*Rottman and Simpson*, 1983; *Lowe et al.*, 2005; *Ungarish*, 2007). The shallow-water equations arranged for a right moving heavier fluid's, with velocity u_h, and depth h_h (Fig. 2.4), are

$$\frac{\partial h_h}{\partial t} + h_h \frac{\partial u_h}{\partial x} + u_h \frac{\partial h_h}{\partial x} = 0, \tag{2.9}$$

$$\frac{\partial u_h}{\partial t} + a \frac{\partial u_h}{\partial x} + b \frac{\partial h_h}{\partial x} = 0, \tag{2.10}$$

with

$$a = \frac{u_h(h_l - \gamma h_h) + 2\gamma u_l h_h}{(\gamma h_h + h_l)}, \tag{2.11}$$

$$b = \frac{-\gamma(u_h - u_l)^2 + (1-\gamma)g h_l}{(\gamma h_h + h_l)}, \tag{2.12}$$

where γ is the density ratio of lighter to heavier fluid, ρ_l/ρ_h, and u_l and h_l are the left moving lighter fluid's velocity and depth, respectively (*Lowe et al.*, 2005). Although shallow-water equations are often simple to implement, they neglect or simply represent stress, friction and diffusivity terms. Moreover, they do not account for the vertical component of velocity, which makes them not suitable for inclined surfaces or flows with non-horizontal direction (*Rotunno et al.*, 2011). Furthermore, these equations do not account for a possible diffusion between miscible fluids.

A more robust approach is solving the Navier-Stokes equations for a multi-fluid system. The Navier-Stokes equations consists of continuity, momentum and diffusion equations as (*Birman et al.*, 2005; *Birman and Meiburg*, 2006)

$$\frac{D\rho}{Dt} = -\rho \nabla \cdot \vec{u}, \tag{2.13}$$

$$\rho \frac{D\vec{u}}{Dt} = -\nabla p + \mu \nabla^2 \cdot \vec{u} + \rho \vec{g}, \tag{2.14}$$

$$\frac{D\rho}{Dt} = D_m \nabla^2 \cdot \rho, \tag{2.15}$$

where D/Dt denotes the total time derivative of a quantity, $\vec{u}$ is fluid velocity vector, and D_m denotes molecular diffusivity. Eq. (2.15) accounts for the density change due to a possible change in concentration of a scalar.

Eq. (2.13) shows the compressible form of the continuity equation. In the case of an incompressible flow the continuity equation is written as (*Birman et al.*, 2005; *Birman and Meiburg*, 2006)

$$\nabla \cdot \vec{u} = 0. \tag{2.16}$$

2.2.2 Numerical simulation of multi-fluid flow

2.2.2.1 Grid based methods

Eulerian methods have been applied intensively in simulating multi-fluid flows. *Birman et al.* (2005) used the Navier-Stokes equations along with the diffusion equation for solving non-Boussinesq lock-exchange flows. They used a finite-difference approach to discretize the governing equations for each fluid. The numerical results showed good agreement with the experiments of *Lowe et al.* (2005). In another approach, the Navier-Stokes equation have been used for a mixture of two incompressible fluids with different properties describing the lock-exchange system (*Étienne et al.*, 2005). *Étienne et al.* (2005) used a Direct Numerical Simulation approach for simulating exchange flows of large density ratios. They discretized the problem domain using a finite-element method and applied a dynamic mesh adaptation technique for refining the mesh at every time step in areas of high density gradients. Finite-volume methods also along with VOF interface tracking techniques have been employed to study gravity currents (*Bonometti and Balachandar*, 2008). Grid-based methods are also the foundation of commercial codes that solve multi-fluid flows across different media, and solute transfer. The most commonly used codes are SUTRA (*Voss et al.*, 2008) and SEAWAT (*Langevin et al.*, 2008), which solve the equations using finite-elements and finite differences, respectively. The packages have been specifically developed to solve applications of multi-fluid flow in porous media such as seawater intrusion in fresh groundwater. However, they also are applied to heat transport (*Werner et al.*, 2013).

The investigation of the literature shows that using grid-based techniques usually requires the detection of the interface, between the fluids throughout a simulation, where the Volume of Fluid technique is often employed (*Serchi et al.*, 2012). Furthermore, dynamic mesh adaptation, with mesh refinement at the interface, is often required (*Étienne et al.*, 2005; *Meiburg et al.*, 2015). Due to these complications particles methods, such as SPH, has been considered as an alternative to solve these problems, as its Lagrangian nature makes it advantageous for automatically simulating the interfaces.

2.2.2.2 SPH simulations

As the earliest attempt to apply SPH to multi-fluid flows, *Monaghan et al.* (1999) employed a WCSPH method to simulate gravity currents descending a ramp. Their numerical approach predicted the denser fluid's velocity with acceptable accuracy. *Shao* (2012) proposed a two-step, prediction and correction, ISPH method to model multi-fluid

systems of incompressible fluids. He proposed two different approaches (i.e., coupled and decoupled ISPH algorithms) to solve multi-fluid problems. In the coupled method, different fluids were not distinguished and the standard ISPH technique was applied across the interface, while in the decoupled method, each phase was treated separately first and then the pressure and shear stress continuity was satisfied across the interface. The results appeared to show that the decoupled technique led to comparatively better results. ISPH along with pressure-decoupling technique has also been used to simulate Boussinesq lock-exchange flows in a confined domain (*Firoozabadi et al.*, 2013); however, the pressure decoupling appears to be problematic in free-surface flows (*Leroy et al.*, 2015).

Pahar and Dhar (2016c) used an ISPH scheme to simulate a lock-exchange flow of salt water intruding into fresh water, by solving the Navier-Stokes equations along with the diffusion equation (Eqs. 2.13 - 2.15). They adjusted the coefficient of molecular diffusivity to account for the diffusivity arising from turbulence.

2.3 Research gaps

The review of the literature shows that SPH has been recently applied to fluid flow in porous media as well as simulating multi-fluid flows due to its advantages in tracking interfaces and time development of the interfaces between fluids. However, there are limited studies and a lack of strong validation against experimental or field observations. Therefore, this application still requires further study.

For fluid flow in porous media, the studies mostly use incompressible schemes. Although incompressible schemes reproduce smoother pressure fields compared to weakly compressible schemes, they require a larger computational time. An explicit incompressible SPH scheme, explicitly solving the PPE, can be considered to reduce the computational cost. Alternatively, weakly compressible schemes with corrective terms to improve the pressure reproduction can be considered. Therefore, there is a need to compare the advantages and disadvantages of different SPH schemes in modeling fluid flow in porous media.

Furthermore, simultaneous SPH simulation of multi-fluid flow across media with different porosities is something that has not been widely conducted using SPH. Modeling these flows is important because a number of important multi-fluid flows in engineering applications occur in porous media such as interaction of seawater and fresh groundwater aquifers and seawater upconing below extraction wells.

2.4 Aims

The overarching aim of the present study is to bring together SPH schemes for multi-fluid flow and flow in porous media to generate a model capable of simulating multi-fluid flow in porous media with applications such as seawater intrusion in fresh groundwater and seawater upconing below groundwater pumping wells; The specific objectives are:

1. To identify an appropriate SPH scheme to model fluid flow in porous media.

   Most previous studies have focused on SPH modeling of fluid flow in porous media using ISPH schemes. The application of WCSPH schemes has rarely been investigated. The main difference between ISPH and WCSPH schemes are in the way pressure is calculated. ISPH calculates the pressure using a pressure Poisson equation, while WCSPH schemes solve the pressure using an equation of state. WCSPH often approximates the viscous force with an artificial viscosity term, while ISPH employs a real viscosity approximation. A comparison of applications of different SPH schemes in modeling fluid flow in porous media is required to investigate possible advantages and disadvantages of these schemes.

2. To develop the modeling approach of multi-fluid flow over and within a porous medium.

   Although SPH has been used to model multi-fluid flows and fluid flow in porous media, there are limited studies using this method. Strong validation against experimental studies are required to validate and improve the modeling approach. Furthermore, simultaneous SPH modeling of a multi-fluid flow that occurs over or within a porous medium has not been widely studied.

3. To investigate the flexibility of the SPH model in engineering applications.

   Generation of a method to simulate multi-fluid flows in porous media is important to study natural problems, such as seawater intrusion in groundwater or seawater upconing below groundwater wells due to pumping. Although there are several grid based models developed to study these problems, the advantages of SPH in simulating these flows and rapid progress in computational technologies encourage to investigate the flexibility of SPH to model these flows. In addition, modeling the seawater upconing requires an SPH algorithm to simulate point mass sinks, which

has not been done in literature. This study also aims to develop the algorithm to lay the foundation for future applicability of the SPH in these applications.

CHAPTER 3

An overview of Smoothed Particle Hydrodynamics

Smoothed Particle Hydrodynamics (SPH) is a Lagrangian method, that uses moving nodes or particles instead of grids for the discretization of a domain. SPH was first developed for astrophysical studies (*Gingold and Monaghan*, 1977; *Lucy*, 1977), and rapidly applied to a variety of engineering applications such as fluid dynamics.

This chapter presents a general overview of the method, and SPH schemes applied in this study.

3.1 Governing equations

The governing equations for a flow of two or more incompressible fluids in saturated porous media with mass sinks and solute transport are (*Pahar and Dhar*, 2016b,a,c; *Bear and Bachmat*, 2012)

$$\nabla \cdot \vec{u} = -\Gamma, \tag{3.1}$$

$$\frac{D\vec{u}}{Dt} = -\frac{\epsilon}{\rho}\nabla p + \frac{\mu}{\rho}\nabla^2\vec{u} + \epsilon\vec{g} + \vec{R}, \tag{3.2}$$

$$\frac{DC}{Dt} = \nabla \cdot (\mathcal{D}_d \nabla C), \tag{3.3}$$

where Eqs. (3.1), (3.2) and (3.3) define mass, momentum and species conservation, respectively, $\vec{u}$ is the Darcian velocity equal to $\epsilon\vec{u}_f$, $\vec{u}_f$ being the fluid intrinsic velocity and ϵ porosity, Γ is a flux per unit of volume due to point sinks, ρ is the fluid density, p is pressure, μ is the dynamic viscosity, $\vec{g}$ is the gravitational acceleration, $\vec{R}$ is the porous media drag force, $\mathcal{D}_d$ is the effective dispersion tensor, and C is concentration of a solute such as salt.

When a fluid passes through a porous medium, the solid matrix of the medium generates a resistance to the fluid motion. This drag force consists of a linear (Darcy) and a quadratic (Forchheimer) term as (*Nield*, 2000)

$$\vec{R} = -\frac{\epsilon\mu}{\rho\kappa}\vec{u} - \frac{\epsilon c_F}{\kappa^{1/2}}|\vec{u}|\vec{u}, \tag{3.4}$$

where κ is the permeability of the media through which the flow occurs, and c_F is the dimensionless Forchheimer coefficient. The Darcy term is dominant in flows with a pore scale Reynolds number lower than unity (*Nield*, 2000). For larger Reynolds numbers, the quadratic term dominates due to inertial effects (*Joseph et al.*, 1982). In the absence of a porous medium $\epsilon = 1$ and $\kappa \to \infty$, such that both terms on the right hand side of Eq. (3.4) are zero.

For compressible fluids, the continuity equation with no sink point is written as (*Bear and Bachmat*, 2012)

$$\frac{D(\epsilon\rho)}{Dt} = -\epsilon\rho\nabla\cdot\vec{u}_f; \tag{3.5}$$

because the simulations of the sink point (see Chapter 5) were conducted using an incompressible scheme, the compressible continuity equation is presented without the sink term.

3.2 SPH formulations

In SPH, a fluid is represented by an ensemble of particles. Each particle carries the fluid properties such as mass, density, velocity, position, viscosity, porosity and pressure. The fluid particles move in accordance with the governing equations. Fluid variables such as velocity, position and pressure, associated with a particle are approximated through

interpolation over its neighbouring particles that fall within a defined domain, called the support domain.

To formulate a function in SPH, two steps are taken: integral representation and particle approximation (*Liu and Liu*, 2003). The integral representation implies that a function can be represented in form of an integral as

$$f(\vec{x}) = \int_{\Omega} f(\vec{x}')\delta(\vec{x} - \vec{x}')d\vec{x}', \tag{3.6}$$

where Ω is the volume of the integration containing $\vec{x}$, $\delta(\vec{x} - \vec{x}')$ is the Dirac function given by

$$\delta(\vec{x} - \vec{x}') = \begin{cases} \infty & \vec{x} = \vec{x}' \\ 0 & \vec{x} \neq \vec{x}' \end{cases}, \tag{3.7}$$

and satisfies the condition given by

$$\int_{-\infty}^{+\infty} \delta(\vec{x})d\vec{x} = 1. \tag{3.8}$$

Using the Dirac function, Eq. (3.6) describes an exact integral representation of an arbitrary function. The Dirac function can be replaced by a smoothing function to create an approximating function that attempts to capture important patterns of the arbitrary function. The integral representation is thus rewritten as

$$< f(\vec{x}) >= \int_{\Omega} f(\vec{x}')W(\vec{x} - \vec{x}', h)d\vec{x}', \tag{3.9}$$

where W is the smoothing or kernel function, and h is smoothing length that controls the influence area of the kernel function (*Liu and Liu*, 2003). Eq. (3.9) is called the kernel approximation in SPH literature and the angle brackets <> are used to represent the kernel approximation.

The particle approximation of a function is achieved by replacing the infinitesimal volume $d\vec{x}'$ in Eq. (3.9) with the finite volume of particles as (*Monaghan*, 1992)

$$< f(\vec{x}_i) >= \sum_{j=1}^{N} \frac{m_j}{\rho_j} f(\vec{x}_j)W(|\vec{x}_i - \vec{x}_j|, h), \tag{3.10}$$

where i and j denote particle labels, m_j and ρ_j represent mass and density of particle j, and m_j/ρ_j is the volume of particle j.

The SPH approximation of the gradient of an arbitrary function can then be approximated as the derivative of Eq. (3.10) (*Monaghan*, 1992)

$$< \nabla f(\vec{x_i}) >= \sum_{j=1}^{N} \frac{m_j}{\rho_j} f(\vec{x_j}) \nabla_i W_{ij}, \tag{3.11}$$

where $W_{ij} = W(|\vec{x}_i - \vec{x}_j|, h)$, $\nabla_i W_{ij} = \frac{\vec{x}_{ij}}{|\vec{x}_{ij}|} \frac{\partial W_{ij}}{\partial |\vec{x}_{ij}|}$, with $|\vec{x}_{ij}| = |\vec{x}_i - \vec{x}_j|$ the distance between particle i and j.

3.2.1 Spatial volume

The volume of particles in SPH is commonly calculated as m/ρ; however, special care needs to be paid to define volume when a particle moves across media with different porosities.

A porosity value is assigned to each particle in this study, that is defined to be a function of position ($\vec{x}$). Thus the value of porosity assigned to a particle is only dependent on the particles' position. When particle j is in a free flow domain ($\epsilon = 1$), the volume of the fluid that the particle carries, V_p (Fig. 3.1a), is $V_{pj} = m_j/\rho_j$. When the particle enters a porous medium, the same mass of fluid occupies a larger volume, V_j (Fig. 3.1b), referred to as spatial volume here, that accounts for both fluid and solid volumes, so that $m_j = \rho_j V_j \epsilon_j$, with $V_{pj} = \epsilon_j V_j$ (Fig. 3.1c). In this study, the mass associated with each particle is kept constant, except for mass change due to diffusion (Eq. 3.3) and mass reduction due to a point sink; therefore, the spatial volume (i.e., the space) associated with each particle is (*Pahar and Dhar*, 2016a)

$$V_j = \frac{m_j}{\epsilon_j \rho_j}. \tag{3.12}$$

The spatial volume associated with each particle depends on the porosity of the medium. Therefore, the spatial volume of a particle inside a porous medium will be larger than that of particle within a fluid domain, with the same mass.

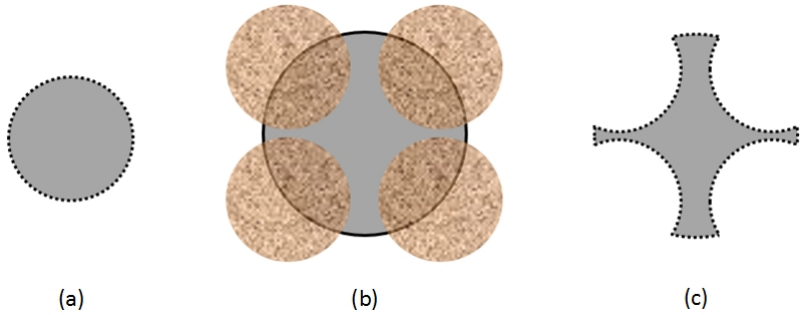

Figure 3.1: Spatial volume of a particle within a (a) free flow domain ($\epsilon = 1$) and (b) a porous medium, (c) volume of fluid within a particle (*Pahar and Dhar*, 2016a).

3.2.2 Kernel function

The smoothing or kernel function in Eq. (3.9) is an even function and is normalized over its influence area. The kernel function must satisfy several conditions.

The kernel summation over its influence domain, Ω, should be equal to unity, i.e.

$$\int_{\Omega} W(\vec{x} - \vec{x}', h) d\vec{x}' = 1. \tag{3.13}$$

The kernel $W(\vec{x} - \vec{x}', h)$ should approach the Dirac-δ function as the smoothing length approaches zero:

$$\lim_{h \to 0} W(\vec{x} - \vec{x}', h) = \delta(\vec{x} - \vec{x}'), \tag{3.14}$$

and has a support domain given by

$$W(\vec{x} - \vec{x}', h) = 0 \quad \text{when} \quad |\vec{x} - \vec{x}'| > \lambda h, \tag{3.15}$$

where λh is the radius of the support domain or influence area of the kernel function (Fig. 3.2), with λ a constant that depends on the nature of the kernel function.

There are several kernel functions introduced in literature. Two kernel functions, i.e. cubic, 3^{rd} order, and spline, 5^{th} order, were tested in this study. The cubic spline kernel function (Fig. 3.3a) used here reads (*Monaghan and Lattanzio*, 1985; *Liu and Liu*, 2003)

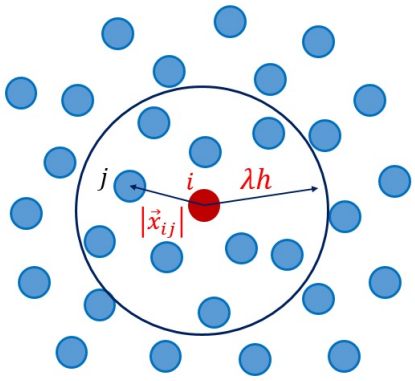

Figure 3.2: Support domain of the kernel function, with radius λh, for particle i.

$$W(q,h) = \alpha_d \times \begin{cases} \frac{2}{3} - q^2 + \frac{1}{2}q^3 & 0 \leq q < 1 \\ \frac{1}{6}(2-q)^3 & 1 \leq q < 2 \\ 0 & q \geq 2, \end{cases} \tag{3.16}$$

where α_d is a normalisation constant equal to $1/h$, $15/(7\pi h^2)$, or $3/(2\pi h^3)$ in one-, two- and three-dimensional domains, respectively, and $q = |\vec{x}_i - \vec{x}_j|/h = |\vec{x}_{ij}|/h$.

The quintic spline kernel function (Fig. (3.3b)) used here reads (*Morris*, 1996; *Liu and Liu*, 2003)

$$W(q,h) = \alpha_d \times \begin{cases} (3-q)^5 - 6(2-q)^5 + 15(1-q)^5 & 0 \leq q < 1 \\ (3-q)^5 - 6(2-q)^5 & 1 \leq q < 2 \\ (3-q)^5 & 2 \leq q < 3 \\ 0 & q > 3, \end{cases} \tag{3.17}$$

with α_d equal to $1/(120h)$, $7/(478\pi h^2)$, and $3/(359\pi h^3)$ in one-, two- and three-dimensional domains, respectively.

The selection of a kernel function and smoothing length in media with different porosities is important. As described in section. 3.2.1, the spatial volume that SPH particles occupy within a porous medium represents both fluid and solid phases volume; therefore, a fluid particle with a given mass within a porous medium has a larger spatial volume than a particle in a free flow domain with same mass. Having a larger spatial volume causes the particles to move apart from each other, leading to a loss of resolution inside the porous medium. Therefore, the number of particles inside the support domain

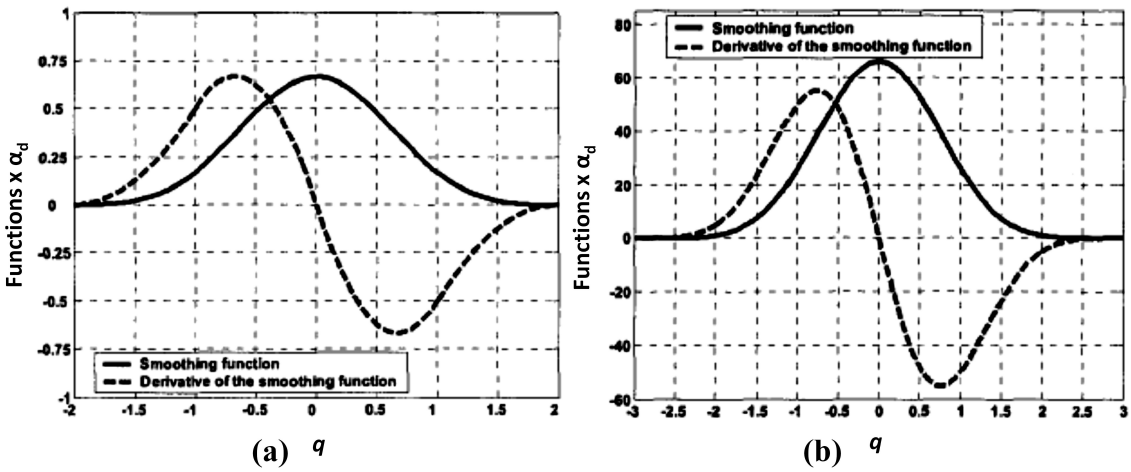

Figure 3.3: The (a) cubic and (b) quintic, kernel functions and their derivatives used in this study (*Liu and Liu*, 2003).

of the kernel function might not be sufficient to accurately approximate the variable and its derivatives. To tackle this problem, a kernel function with a larger support domain, such as the quintic function, can be used. In case of using a kernel function with a smaller support domain such as the cubic spline, the smoothing length needs to be adjusted (*Pahar and Dhar*, 2016a). To adjust the smoothing length, its length should be inversely proportional to square root of porosity, so that in a medium with lower porosity the smoothing length is larger. Using a variable smoothing length formally adds extra terms involving the derivative of smoothing length in the momentum equation (*Price and Monaghan*, 2004); however, these terms are neglected in this study. Because the same value of smoothing length should be used for a pair of interacting particles to conserve momentum, the smoothing length for interacting particles i and j is calculated as $h_{ij} = (h_i + h_j)/2$ (*Rafiee et al.*, 2007).

3.3 SPH approximations

The governing equations are discretized into a set of ordinary differential equations by the particle approximations of a function (Eq. 3.10) and derivative of a function (Eq. 3.11). To generate the particle approximations of the functions and derivatives in porous media, the spatial volume concept is used, so that the spatial volume (Eq. 3.12) is replaced by the conventional volume of particles (m/ρ) in the approximations provided in literature.

3.3.1 Continuity equation for an incompressible fluid

There are several ways in the literature to approximate the divergence of velocity in the continuity equation (*Liu and Liu*, 2003). However, one of the most common approximations is applied here and Eq. (3.1) is written in discrete form as (*Pahar and Dhar*, 2016a)

$$(\nabla \cdot \vec{u})_i = \sum_{j=1}^{N} \frac{m_j}{\epsilon_j \rho_j} (\vec{u}_j - \vec{u}_i) \cdot \nabla_i W_{ij} = -\Gamma_i. \tag{3.18}$$

where Γ_i is the contribution of the sink points around the particle i on the divergence of velocity (section 3.8).

3.3.2 Continuity equation for a compressible fluid

The compressible continuity equation (Eq. 3.5) is approximated as

$$\frac{D\rho_i}{Dt} = \sum_{j=1}^{N} \frac{m_j}{\epsilon_j} (\vec{u}_i - \vec{u}_j) \cdot \nabla_i W_{ij}. \tag{3.19}$$

The compressible SPH scheme used in this study, δ-SPH, benefits from a diffusive term added to the approximation of the continuity equation (Eq. 3.19) to reduce the common density and pressure fluctuations in weakly-compressible SPH schemes as (*Marrone et al.*, 2011)

$$\frac{D\rho_i}{Dt} = \sum_{j=1}^{N} \frac{m_j}{\epsilon_j} (\vec{u}_i - \vec{u}_j) \cdot \nabla_i W_{ij} + \delta h c_0 \sum_{j=1}^{N} \frac{m_j}{\epsilon_j \rho_j} \vec{\psi}_{ij} \cdot \nabla_i W_{ij}, \tag{3.20}$$

with

$$\vec{\psi}_{ij} = 2(\rho_j - \rho_i) \frac{\vec{x}_{ji}}{|\vec{x}_{ij}|^2} - \left[\langle \nabla \rho \rangle_i^L + \langle \nabla \rho \rangle_j^L \right], \tag{3.21}$$

$$\langle \nabla \rho \rangle_a^L = \sum_b \frac{m_b}{\epsilon_b \rho_b} (\rho_b - \rho_a) L_a \nabla_a W_b, \tag{3.22}$$

$$L_a = \left[\sum_b \frac{m_b}{\epsilon_b \rho_b} (\vec{x}_b - \vec{x}_a) \otimes \nabla_a W_b \right]^{-1}, \tag{3.23}$$

where δ is set to 0.1 (*Marrone et al.*, 2011)

3.3.3 Momentum equation

The momentum equation consists of the pressure gradient, the viscous force, acceleration due to gravity and the drag force. The gravity and drag terms are calculated directly without any approximation.

3.3.3.1 Pressure gradient

The pressure gradient term in Eq. (3.2) is approximated in two common ways, in this thesis, as

$$\left(\frac{\epsilon}{\rho}\nabla p\right)_i = \epsilon_i \sum_{j=1}^{N} \frac{m_j}{\epsilon_j}\left(\frac{p_i}{\rho_i^2} + \frac{p_j}{\rho_j^2}\right)\nabla_i W_{ij}, \tag{3.24}$$

and

$$\left(\frac{\epsilon}{\rho}\nabla p\right)_i = \epsilon_i \sum_{j=1}^{N} \frac{m_j}{\epsilon_j}\left(\frac{p_i + p_j}{\rho_i \rho_j}\right)\nabla_i W_{ij}. \tag{3.25}$$

More sophisticated pressure gradient terms can be found in *Khayyer et al.* (2017a).

3.3.3.2 Viscous term

The viscous term in Eq. (3.2) is often used in incompressible SPH schemes and is approximated as (*Shao and Lo*, 2003)

$$\left(\frac{\mu}{\rho}\nabla^2\vec{u}\right)_i = \sum_{j=1}^{N} \frac{4m_j(\mu_i + \mu_j)\vec{u}_{ij}\cdot\vec{x}_{ij}}{\epsilon_j(\rho_i + \rho_j)^2\left(|\vec{x}_{ij}|^2 + \eta^2\right)}\nabla_i W_{ij}, \tag{3.26}$$

where η is a small parameter included to ensure that the denominator remains non-zero ($\eta = 0.001h_{ij}$, with $h_{ij} = (h_i + h_j)/2$), and $\vec{u}_{ij}^n = \vec{u}_i - \vec{u}_j$.

In compressible SPH schemes, often an artificial viscosity term is used and is equivalent to the viscous term in the momentum equation and stabilizes the numerical scheme. The artificial viscosity in the compressible scheme employed in this study, δ-SPH, is approximated as (*Molteni and Colagrossi*, 2009; *Marrone et al.*, 2011)

$$\left(\frac{\mu}{\rho}\nabla^2\vec{u}\right)_i \equiv \alpha h c_0 \frac{\rho_0}{\rho_i}\sum_{j=1}^{N}\frac{m_j}{\epsilon_j\rho_j}\pi_{ij}\nabla_i W_{ij}, \tag{3.27}$$

with

$$\pi_{ij} = \frac{(\vec{u}_j - \vec{u}_i) \cdot \vec{x}_{ji}}{|\vec{x}_{ij}|^2}, \tag{3.28}$$

where α is set to 0.02, ρ_o is the density at the free surface of flow, c_0 is the speed of sound and must be at least 10 times the maximum velocity of the flow. The speed of sound was assumed to be $20\sqrt{gH}$ here, with H being the maximum depth of the flow (*Molteni and Colagrossi*, 2009).

3.3.4 Diffusion equation

The diffusion of scalar in this study is handled in two different ways. In the first, the effective dispersion tensor ($\mathcal{D}_d$) only assumed to account for diffusivity; dispersivity is neglected, so that $\mathcal{D}_d$ becomes a constant, while in the second, it is considered as a size 2 matrix to account for dispersivity effects. We will refer to the methods as Diffusion and Dispersion-Diffusion.

3.3.4.1 Diffusion

Eq. (3.3) is solved assuming $\mathcal{D}_d$ as a scalar coefficient. We refer to the coefficient as the effective coefficient of diffusivity ($\mathcal{D}_e$). The SPH approximation of the equation reads (*Ghasemi et al.*, 2013; *Zhu and Fox*, 2001)

$$(\nabla \cdot (\mathcal{D}_e \nabla C))_i = \sum_{j=1} \frac{m_j}{\epsilon_j \rho_j} \frac{(\mathcal{D}_{ei} + \mathcal{D}_{ej}) \vec{x}_{ij} \cdot \nabla_i W_{ij}}{|\vec{x}_{ij}|^2 + \eta^2} (C_i - C_j), \tag{3.29}$$

where the effective coefficient of diffusivity, $\mathcal{D}_e$, is determined using an empirical equation based on the flow regime and the porosity of the medium. The empirical equation assumes the porous medium is saturated (*Simunek and Suarez*, 1993; *Pahar and Dhar*, 2016c), and is given by

$$\mathcal{D}_{ei} = (D_{mi} + D_{ti})(\epsilon_i)^{4/3}, \tag{3.30}$$

where D_m and D_t are coefficients of molecular and turbulent eddy diffusivity, respectively. D_t is only added for flows with Reynolds numbers higher than 1000 (*Simpson*, 1997).

3.3.4.2 Dispersion-Diffusion

In this approach the effects of dispersivity is also accounted for, so that the $\mathcal{D}_d$ tensor is determined using the effective coefficient of diffusivity, dispersivity, and particle velocities as (*Salamon et al.*, 2006)

$$\mathcal{D}_{di} = \mathcal{D}_{ei} I + d_{ti}|\vec{u}_i| I + (d_{li} - d_{ti}) \frac{\vec{u}_i \otimes \vec{u}_i^T}{|\vec{u}_i|}, \tag{3.31}$$

where d_l and d_t are longitudinal and transverse dispersivity, I is identity matrix of size 2 (for 2D flow), and $\mathcal{D}_e$ is the effective coefficient of diffusivity. $\mathcal{D}_d$ in Eq. (3.31) is an anisotropic and heterogeneous dispersion matrix. Eq. (3.31) is approximated using an anisotropic SPH approximation (*Tran-Duc et al.*, 2016). To simplify the approximation procedure, $\mathcal{D}_d$ will be assumed to be a diagonal matrix. This assumption is reasonable when bulk flow is vertical or horizontal, such that the second term on the right hand side of Eq. (3.31) can be assumed to be diagonal. The variation of concentration is then approximated as (*Tran-Duc et al.*, 2016)

$$\left(\nabla \cdot (\mathcal{D}_d \nabla C)\right)_i = 2 \sum_{j=1}^{N} \frac{m_j}{\epsilon_j \rho_j} \left(\frac{e_{ij,1}^2}{\bar{D}_{dij,11}} + \frac{e_{ij,2}^2}{\bar{D}_{dij,22}} \right)^{-1} \frac{\vec{x}_{ij} \cdot \nabla_i W_{ij}}{|\vec{x}_{ij}|^2 + \eta^2} (C_i - C_j), \tag{3.32}$$

where $e_{ij} = \vec{x}_{ij}/|\vec{x}_{ij}|$ is the unit vector from i to j, and $\bar{\mathcal{D}}_{dij}$ is average of the effective diffusivity tensors of particles i and j. The numbers in subscript of e_{ij} and $\bar{\mathcal{D}}_{dij}$ reference a particular element in the vector and the matrix, respectively.

3.4 Boundaries

3.4.1 Solid boundaries

A single layer of virtual particles is used to identify solid boundaries (*Monaghan*, 1994). The virtual particles interact only with fluid particles and exert a repulsive force via a Leonard-Jones potential given by (*Monaghan*, 1994)

$$F(\vec{x})_{ij} = \begin{cases} L \left[\left(\frac{r_0}{|\vec{x}_{ij}|} \right)^{p_1} - \left(\frac{r_0}{|\vec{x}_{ij}|} \right)^{p_2} \right] \frac{1}{|\vec{x}_{ij}|} & \frac{r_0}{|\vec{x}_{ij}|} \geq 1, \\ 0 & \frac{r_0}{|\vec{x}_{ij}|} < 1. \end{cases} \tag{3.33}$$

Here p_1 and p_2 are constants equal to 4 and 2 respectively, L is the square of the largest

velocity of flow, and r_0 is a cut off distance assumed to be 0.8 times the initial distance between virtual particles. Repulsive forces are applied perpendicularly to the boundaries, and along 45° at corners. The distance between the virtual particles is set to half the initial spacing of the fluid particles to ensure impermeable boundaries are maintained (Fig. 3.4).

3.4.2 Free and no slip boundary conditions

Ghost particles are used to impose boundary conditions. For a fluid particle within a distance of λh from the solid boundaries, where λ is determined in accordance with the kernel, a ghost particle is produced symmetrically on the other side of the boundaries (*Liu and Liu*, 2003) (Fig. 3.4a). Ghost particles are assigned the same density, concentration, mass, pressure, porosity, dynamic viscosity, coefficients of molecular and turbulent eddy diffusivity, and smoothing length as the corresponding fluid particles. To impose free-slip boundary conditions, the component of velocity parallel to the boundary is unchanged, while for no-slip it is reversed. The normal component of the velocity is reversed for both free-slip and no-slip conditions (*Marrone et al.*, 2011) (Fig. 3.4b).

Modified no-slip boundary condition

A mixed free-slip and no-slip boundary conditions, which are recommended for higher Reynolds numbers, can also be implemented. The no-slip boundary condition is used in calculating the viscous term in the momentum equation while the free-slip boundary condition is used in calculating the pressure Poisson equation, the pressure gradient and change in concentration (*Marrone et al.*, 2013; *Grenier et al.*, 2013). The mixed boundary condition is called modified no-slip boundary condition here.

3.4.3 Free surface

A free surface pressure condition is assigned after calculating particle pressure. Free surfaces are identified using particle densities. The particle densities are approximated using a density summation (*Liu and Liu*, 2003) as

$$\rho_i^{\epsilon} = \sum_{j=1}^{N} \frac{m_j}{\epsilon_j} W_{ij}. \tag{3.34}$$

As the free surface particles reside within a non-complete support domain, their particle density is significantly less than the fluid's initial density. When the density of a

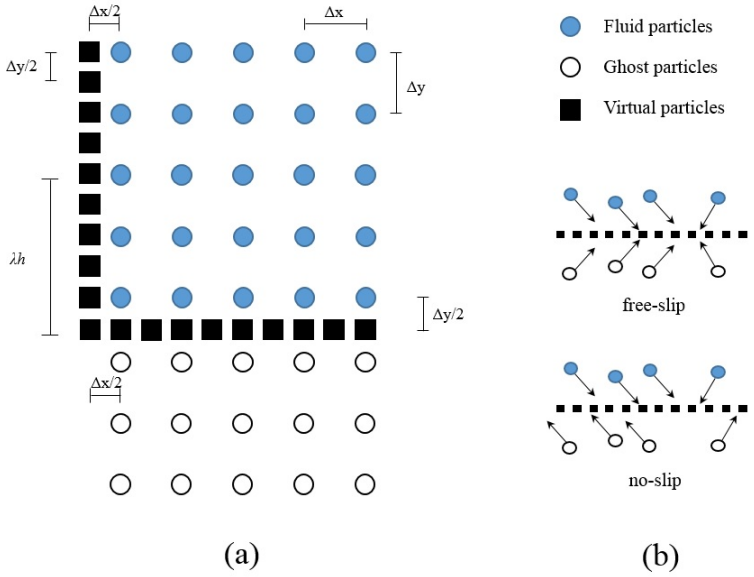

Figure 3.4: Schematic representation of (a) virtual, fluid and ghost particles (Ghost particles are only shown for the fluid particles adjacent to the lower horizontal solid boundary), and (b) application of free-slip and no-slip boundary conditions.

particle drops below 99% of its initial density, it is considered as a free-surface particle and zero pressure is assigned to that particle (*Shao and Lo*, 2003). Eq. (3.34) is only used to detect free surfaces (i.e., it is not used to update the density of particles).

3.4.4 Interface conditions

When particles move between media with different porosities, the porosity values are assigned depending on the particles' position. However, the geometrical transition at an interface between media is not usually sharp, and a sharp transition may not properly represent the physics of the problem (*Duman and Shavit*, 2010). Furthermore, based on investigations, in this thesis, this sharp change in porosity may lead to numerical instabilities in some cases. In this study, in some cases (Chapter. 4), a gradual linear change of porosity is applied at the interface between media with different porosities to check its advantages and disadvantages. As shown in Fig. 3.5, the porosity linearly changes in a transition layer between a fluid flow domain, $\epsilon = 1$, and a porous medium, $\epsilon = \epsilon_m$. The thickness of the transition layer is assumed to be equal to the diameter of the support domain of the kernel function, $\delta_\epsilon = 2\lambda h$. A sharp interface can also be simulated with no transition layer.

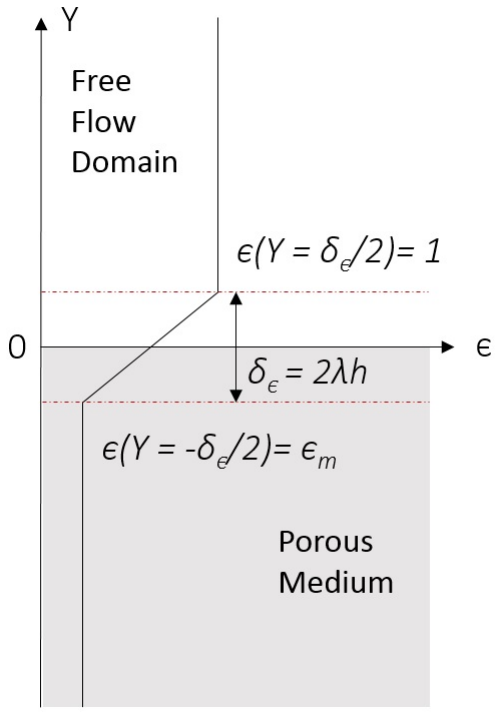

Figure 3.5: Definition of the transition layer between a free flow and a porous medium with porosity ϵ_m. The depth of the transition layer, δ_ϵ, equals the diameter of the support domain of the kernel function, $2\lambda h$.

3.4.5 Inflow boundaries

Inflow boundary condition is used to simulate a fluid recharge into porous media. Inflow particles are used to simulate the inflow of fluid into the domain (*Nomeritae et al.*, 2018). The thickness of the zone occupied by inflow particles is set to be larger than the radius of the support domain of the kernel function. Inflow particles within the inflow zone are moved with a constant velocity determined by the inflow rate. Once an inflow particle moves outside the inflow zone (Fig. 3.6), it is turned into a fluid particle and moves according to the governing equations. The inflow particles' velocity and pressure are used in approximating the hydrodynamics of the fluid particles in a domain but not vice versa (*Federico et al.*, 2012).

3.5 Particle search

To approximate variables of particle i, a search algorithm is used to detect particles around it that fall within a distance equal to support domain of the kernel function.

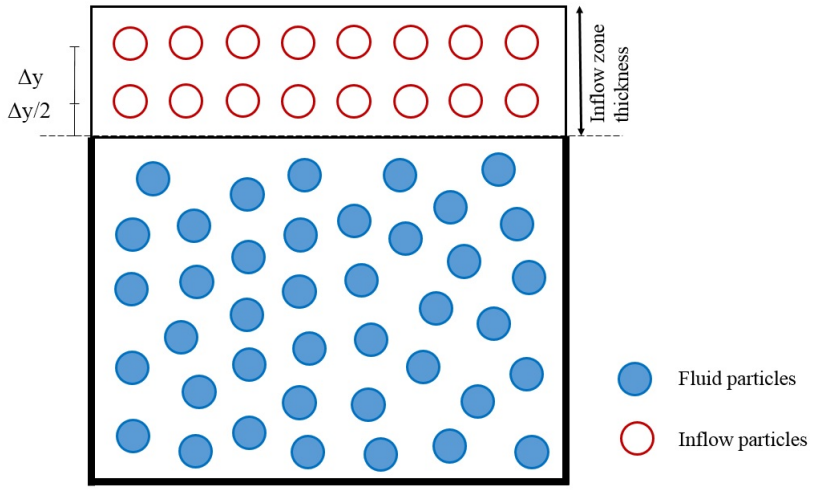

Figure 3.6: Schematic view of an inflow boundary condition.

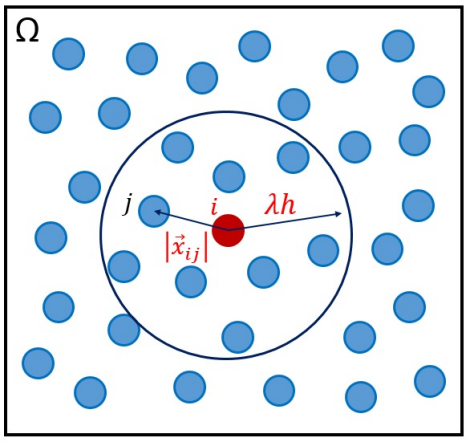

Figure 3.7: A schematic view of the all-pair search algorithm to find the nearest neighbouring particles to approximate the variables in particle i (Section 3.5.1).

3.5.1 All pair search

Particles surrounding the particle i that fall within a distance equal to the support domain of the kernel function are detected at each time step. The distance between all particles within the domain Ω (Fig. 3.7) and the particle i needs to be checked to determine whether they are within the support domain of particle i (*Liu and Liu*, 2003). Although this algorithm is straightforward, it requires high computational time and it is only applicable to small scale problems.

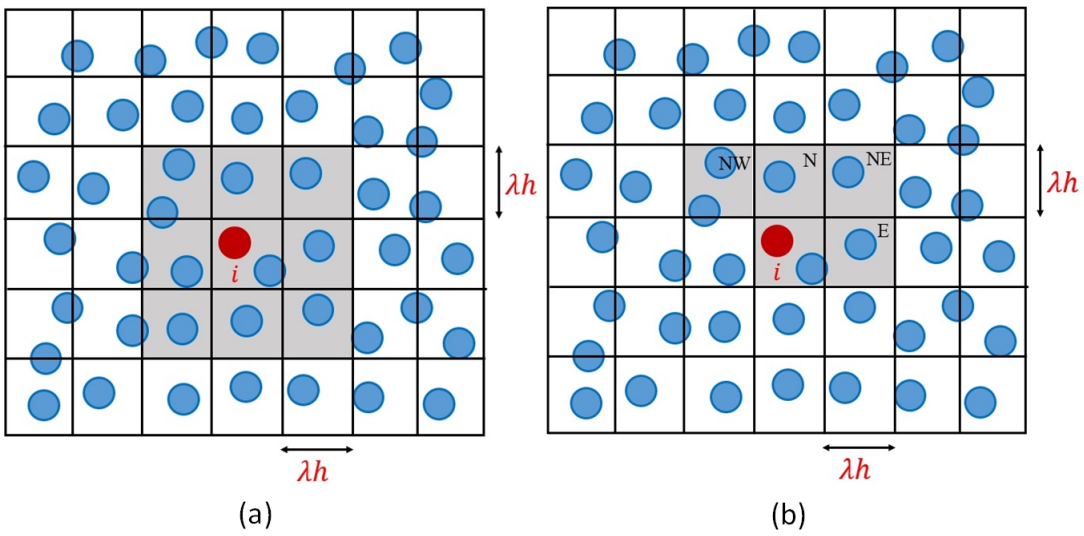

Figure 3.8: (a) Link list and (b) the improved linked list algorithm to find the nearest neighbouring particles (Section 3.5.2).

3.5.2 Linked list algorithm

In this algorithm, a background mesh is created by dividing a domain into a set of square cells, with sizes equal to the radius of the support domain of the kernel function. For a particle i only particles that are located within the same cell as i and the surrounding cells can contribute to the summations (Fig. 3.8a). Therefore, the computational time is significantly reduced compared to the all pair search. The linked list algorithm is further improved by only searching across a few cells (i.e., north west, north, north east, east, and the same cell that particle i resides) (Fig. 3.8b), as the rest of the cells surrounding the centred cell are considered through sweeping. In this study the linked list approaches are used.

3.6 Numerical schemes

In this study, Explicit incompressible-SPH (EISPH) (*Nomeritae et al.*, 2016) and δ-SPH (*Marrone et al.*, 2011) were used to compare their advantages and disadvantages for fluid flow in porous media. The scheme that was selected between these was further developed, by incorporating Eq. (3.3), to solve multi-fluid flow in porous media.

3.6.1 EISPH

3.6.1.1 Euler integration algorithm

The governing equations are solved with an EISPH scheme, which employs two steps, prediction and pressure correction (*Cummins and Rudman*, 1999), with an approximate solution of the Poisson equation. The time integration algorithm is first order in time for velocity and second order in time for particle position. Although the algorithm is not totally first order, it is referred as an Euler algorithm in this study.

In the prediction step, the viscous, gravity and the drag forces contribute to the velocity and position of particles as

$$\vec{u}_i^* = \vec{u}_i^n + \left(\frac{\mu}{\rho}\nabla^2\vec{u}\right)_i^n \Delta t + \epsilon_i^n \left(\vec{g} - \frac{\mu}{\rho\kappa}\vec{u}\right)_i^n \Delta t, \tag{3.35}$$

where $\vec{u}^*$ is intermediate velocity, $\vec{u}^n$ is particle velocity at time $n\Delta t$, with Δt constant throughout the simulations.

The viscous term is approximated using Eq. (3.26) as

$$\left(\frac{\mu}{\rho}\nabla^2\vec{u}\right)_i^n = \sum_{j=1}^{N} \frac{4m_j^n(\mu_i+\mu_j)\vec{u}_{ij}^n \cdot \vec{x}_{ij}^n}{\epsilon_j^n(\rho_i^n+\rho_j^n)^2\left(|\vec{x}_{ij}^n|^2+\eta^2\right)} \nabla_i {W_{ij}}^n, \tag{3.36}$$

The gravitational and drag terms are calculated directly, with the drag term calculated only for particles inside a porous medium.

The intermediate particle positions ($\vec{x}^*$) are calculated using the intermediate intrinsic velocity of the particles as

$$\vec{x}_i^* = \vec{x}_i^n + \frac{\vec{u}_i^*}{\epsilon^n}\Delta t, \tag{3.37}$$

where $\vec{x}^n$ is particle position at time $n\Delta t$. Afterwards, the intermediate porosity of particles, ϵ^*, are assigned using the intermediate position of particles.

In the second step, the particle velocities are calculated at the new time step as

$$\vec{u}_i^{n+1} = \vec{u}_i^* - \frac{\epsilon_i^*}{\rho_i^n}\nabla p_i^{n+1}\Delta t, \tag{3.38}$$

where p^{n+1} is particle pressure at time $(n+1)\Delta t$. Eqs. (3.38) and (3.1) are combined to form the pressure Poisson equation as

$$\nabla \cdot \left(\frac{\epsilon^*}{\rho^n} \nabla p^{n+1} \right)_i = \left(\frac{\nabla \cdot \vec{u}^* + \Gamma}{\Delta t} \right)_i , \tag{3.39}$$

where Γ is the contribution of the sink points around particle i (see Section 3.8).

The divergence of the intermediate velocity is approximated as in Eq. (3.18) as

$$\left(\nabla \cdot \vec{u}^* \right)_i = \sum_{j=1}^{N} \frac{m_j^n}{\epsilon_j^* \rho_j^n} (\vec{u}_j^* - \vec{u}_i^*) \cdot \nabla_i W_{ij}^*. \tag{3.40}$$

The Laplacian operator in Eq. (3.39) is expressed using an approximation of the second derivative (*Monaghan*, 2005) and reads

$$\nabla \cdot \left(\frac{\epsilon^*}{\rho^n} \nabla p^{n+1} \right)_i = \sum_{j=1}^{N} \frac{m_j^n}{\epsilon_j^* \rho_i^n \rho_j^n} \frac{\left(\epsilon_i^* + \epsilon_j^* \right) \vec{x}_{ij}^* \cdot \nabla_i W_{ij}^*}{|\vec{x}_{ij}^*|^2 + \eta^2} \left(p_i^{n+1} - p_j^{n+1} \right), \tag{3.41}$$

so that the PPE becomes

$$\sum_{j=1}^{N} \frac{m_j^n}{\epsilon_j^* \rho_i^n \rho_j^n} \frac{\left(\epsilon_i^* + \epsilon_j^* \right) \vec{x}_{ij}^* \cdot \nabla_i W_{ij}^*}{|\vec{x}_{ij}^*|^2 + \eta^2} \left(p_i^{n+1} - p_j^{n+1} \right) = \left(\frac{\nabla \cdot \vec{u}^* + \Gamma}{\Delta t} \right)_i . \tag{3.42}$$

Eq. (3.42) is written for particle i as

$$p_i^{n+1} = \frac{B_i + \sum_{j=1}^{N} A_{ij} p_j^{n+1}}{\sum_{j=1}^{N} A_{ij}}, \tag{3.43}$$

with

$$A_{ij} = \frac{m_j^n}{\epsilon_j^* \rho_i^n \rho_j^n} \frac{\left(\epsilon_i^* + \epsilon_j^* \right) \vec{x}_{ij}^* \cdot \nabla_i W_{ij}^*}{|\vec{x}_{ij}^*|^2 + \eta^2}, \tag{3.44}$$

and

$$B_i = \left(\frac{\nabla \cdot \vec{u}^* + \Gamma}{\Delta t} \right)_i . \tag{3.45}$$

Eq. (3.43) should be solved using a linear solver; however, this is explicitly solved with an approximation that has been proven to lead to satisfactory results in variety of applications (*Nomeritae et al.*, 2016; *Bui and Nguyen*, 2017; *Nomeritae et al.*, 2018). The

value of p_j^{n+1} on the right hand side of Eq. (3.43) is assumed to be equal to p_j^n; and the time step value is set to a sufficiently small value. The pressure of each particle is thus approximated explicitly as

$$p_i^{n+1} = \frac{B_i + \sum_{j=1}^{N} A_{ij} p_j^n}{\sum_{j=1}^{N} A_{ij}}. \tag{3.46}$$

The initial pressure value of the free surface particles are set to zero. Therefore, the pressure of free surface particles from the previous time step is always equal to zero. After the calculation of pressure using Eq. (3.46), the pressure of particles of the free surface is imposed to be zero, if Eq. (3.46) assigns non-zero values to them.

The calculated pressure values are used to calculate the pressure gradient using Eq. (3.24) as

$$\left(\frac{\epsilon^*}{\rho^n}\nabla p^{n+1}\right)_i = \epsilon_i^* \sum_{j=1}^{N} \frac{m_j^n}{\epsilon_j^*}\left(\frac{p_i^{n+1}}{\rho_i^{n2}} + \frac{p_j^{n+1}}{\rho_j^{n2}}\right)\nabla_i W_{ij}^*. \tag{3.47}$$

Afterwards the velocity field at the new time step is calculated using Eq. (3.38). The new position is calculated as

$$\vec{x}_i^{n+1} = \vec{x}_i^n + \frac{\left(\frac{\vec{u}_i^n}{\epsilon_i^n}\right) + \left(\frac{\vec{u}_i^{n+1}}{\epsilon_i^*}\right)}{2}\Delta t, \tag{3.48}$$

and new particle porosity, ϵ^{n+1}, associated with the new position is assigned.

In problems associated with multi-fluid flows, the new concentration of each particle is calculated in this stage using Eq. (3.3) as (*Pahar and Dhar*, 2016c)

$$C_i^{n+1} = C_i^n + \left(\nabla \cdot \left(\mathcal{D}_d^{n+1}\nabla C\right)\right)_i \Delta t, \tag{3.49}$$

where the second term in the right hand side of Eq. (3.49) is approximated depending on the nature of the problem (i.e. whether diffusivity or dispersivity govern the physics of the problem), using one of the approaches in section 3.3.4.

Subsequently, density and the mass of each particle are updated as (*Pahar and Dhar*, 2016c)

$$\rho_i^{n+1} = C_i^{n+1}(\rho_s - \rho_f) + 0.5(\rho_s + \rho_f), \tag{3.50}$$

$$m_i^{n+1} = \rho_i^{n+1} V_{pi}^{n+1}, \tag{3.51}$$

where V_p is volume of fluid a particle carries and is equal to $V_p = m_j/\rho_j$.

The time step value, Δt, is defined to satisfy the Courant stability and viscous diffusion conditions as

$$\Delta t \leq min(\Delta t_{CFL}, \Delta t_{visc}), \tag{3.52}$$

with

$$\Delta t_{CFL} \leq 0.25 \frac{h}{u_{max}}, \tag{3.53}$$

and

$$\Delta t_{visc} \leq 0.125 \frac{h^2}{\nu}, \tag{3.54}$$

where u_{max} is the predicted maximum velocity in the computations and ν is the kinematic viscosity (*Morris et al.*, 1997).

3.6.1.2 Heun integration algorithm

In the Heun integration algorithm, velocity and position of the particles are solved in two stages at each time step. In the first stage, an approximate value of velocity, $\tilde{\vec{u}}_i^{n+1}$, and position, $\tilde{\vec{x}}_i^{n+1}$ at the new time step are predicted using the first order Euler method as

$$\tilde{\vec{u}}_i^{n+1} = \vec{u}_i^n + \left(\frac{D\vec{u}}{Dt}\right)^n_{i[x^n, \epsilon^n, u^n, p^n, \rho^n]} \Delta t, \tag{3.55}$$

$$\tilde{\vec{x}}_i^{n+1} = \vec{x}_i^n + \left(\frac{\vec{u}_i^n}{\epsilon_i^n}\right) \Delta t \;\Rightarrow \tilde{\epsilon}_i^{n+1} = f\left(\tilde{\vec{x}}_i^{n+1}\right). \tag{3.56}$$

The variables inside the bracket in Eq. (3.55) are used in the corresponding stage. In the second stage, the values of the variables are updated as

$$\vec{u}_i^{n+1} = \vec{u}_i^n + \frac{\left(\frac{d\vec{u}}{dt}\right)^n_{i[x^n, \epsilon^n, u^n, p^n, \rho^n]} + \left(\frac{d\tilde{\vec{u}}}{dt}\right)^{n+1}_{i[\tilde{x}^{n+1}, \tilde{\epsilon}^{n+1}, \tilde{u}^{n+1}, p^{n+1}, \rho^n]}}{2} \Delta t, \tag{3.57}$$

$$\vec{x}_i^{n+1} = \vec{x}_i^n + \frac{\left(\frac{\vec{u}_i^n}{\epsilon_i^n}\right) + \left(\frac{\tilde{\vec{u}}_i^{n+1}}{\tilde{\epsilon}_i^{n+1}}\right)}{2} \Rightarrow \epsilon_i^{n+1} = f\left(\vec{x}_i^{n+1}\right), \tag{3.58}$$

and finally the concentration and density of the particles are updated as

$$C_i^{n+1} = C_i^n + \left(\nabla \cdot \left(\mathcal{D}_d^{n+1} \nabla C\right)\right)_{i[x^{n+1}, \epsilon^{n+1}, C^n]} \Delta t, \tag{3.59}$$

$$\rho_i^{n+1} = C_i^{n+1}(\rho_d - \rho_l) + 0.5(\rho_d + \rho_l) \;\Rightarrow m_i^{n+1} = \rho_i^{n+1} V_{pi}. \tag{3.60}$$

The approximate prediction-correction method (See 3.6.1.1) is used to calculate du/dt and impose incompressibility at each stage.

Because the momentum and pressure steps must be calculated twice; therefore, the Heun algorithm is approximately twice as expensive as the Euler.

3.6.2 δ-SPH

δ-SPH is an improved form of WC-SPH proposed by *Molteni and Colagrossi* (2009). The method was further improved by *Antuono et al.* (2010) and *Marrone et al.* (2011). In this method the pressure is explicitly calculated using the equation of state (*Marrone et al.*, 2011)

$$p = c_o^2(\rho - \rho_0), \tag{3.61}$$

where c_0 is the speed of sound and here is set to $20\sqrt{gH}$ (*Molteni and Colagrossi*, 2009).

In this scheme, an artificial viscosity is used instead of the viscous term in Eq. (3.2), and a diffusive term is added to the continuity equation (Eq. (3.19)) to reduce density and pressure fluctuations as in *Marrone et al.* (2011). The governing equations are written as

$$\frac{D\rho_i}{Dt} = \sum_{j=1}^{N} \frac{m_j}{\epsilon_j}(\vec{u}_i - \vec{u}_j) \cdot \nabla_i W_{ij} + \delta h c_0 \sum_{j=1}^{N} \frac{m_j}{\epsilon_j \rho_j} \vec{\psi}_{ij} \cdot \nabla_i W_{ij}, \tag{3.62}$$

$$\frac{D\vec{u}_i}{Dt} = -\epsilon_i \sum_{j=1}^{N} \frac{m_j}{\epsilon_j} \left(\frac{p_i + p_j}{\rho_i \rho_j}\right) \nabla_i W_{ij} + \epsilon_i \vec{g} + \alpha h c_0 \frac{\rho_0}{\rho_i} \sum_{j=1}^{N} \frac{m_j}{\epsilon_j \rho_j} \pi_{ij} \nabla_i W_{ij} + \vec{R}_i, \tag{3.63}$$

The Leapfrog time integration scheme was applied to solve the δ-SPH equations as in *Bui et al.* (2008)

$$\rho_i^{n+1/2} = \rho_i^{n-1/2} + \left(\frac{D\rho}{Dt}\right)_i^n \Delta t, \tag{3.64}$$

$$\vec{u}_i^{n+1/2} = \vec{u}_i^{n-1/2} + \left(\frac{D\vec{u}}{Dt}\right)_i^n \Delta t, \tag{3.65}$$

$$\vec{x}_i^{n+1} = \vec{x}_i^n + \frac{\vec{u}_i^{n+1/2}}{\epsilon_i^n}\Delta t. \tag{3.66}$$

Shephard filtering is applied at each time step to renormalise the density field using (*Dalrymple and Rogers*, 2006),

$$\rho_i^n = \frac{\sum_{j=1}^N \frac{m_j^n}{\epsilon_j^n \rho_j^n}\rho_j^n W_{ij}^n}{\sum_{j=1}^N \frac{m_j^n}{\epsilon_j^n \rho_j^n} W_{ij}^n}, \tag{3.67}$$

which reduces density oscillations especially at free surfaces.

The time step value, Δt, is defined to satisfy the Courant stability conditions via (*Barcarolo*, 2013; *Nomeritae et al.*, 2016)

$$\Delta t_{CFL} \leq 0.75\frac{h}{c_0}. \tag{3.68}$$

3.7 A comparison between EISPH and δ-SPH

This section addresses the first objective, which is to identify an appropriate SPH scheme to use in simulating fluid flow over and within porous media. The schemes are applied to a case study of a fluid percolating into a porous medium.

The EISPH has been used to simulate a variety of engineering applications due to its lower computational cost compared to ISPH (*Hosseini et al.*, 2007; *Nomeritae et al.*, 2016, 2018). Although the method uses approximation in solving PPE, studies have shown the ability of the scheme to provide smooth and acceptable pressures and velocity fields (*Nomeritae et al.*, 2016, 2018). Because, δ-SPH has been proven to reproduce smoother and more accurate pressures, compared to conventional weakly compressible schemes, in a range of engineering applications (*Molteni and Colagrossi*, 2009; *Marrone et al.*, 2011; *Nomeritae et al.*, 2016), it has been selected as the WCSPH scheme in this study.

3.7.1 Vertical percolation into a porous medium

An experimental measurement of percolation of glycerine in a porous medium made of glass beads, reported in *Acton et al.* (2001), is simulated here using the EISPH and δ-SPH schemes. The experiment was conducted in a Perspex tube of internal diameter 0.034

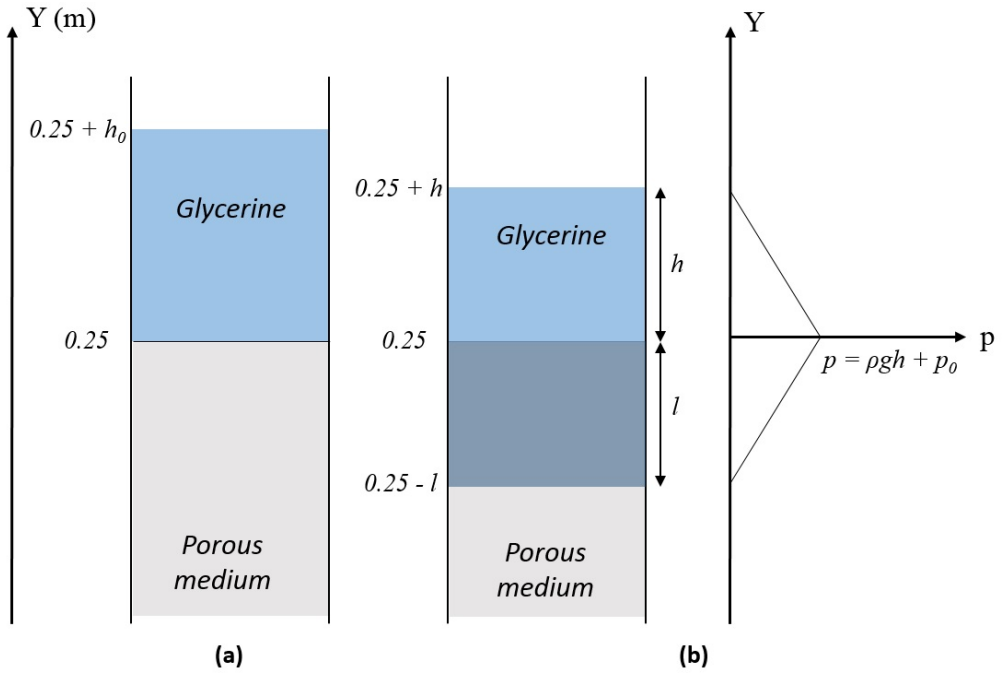

Figure 3.9: (a) Schematic view of the experimental tank. (b) The extension of the fluid from the free flow domain to the porous medium and the theoretical pressure distribution (Section 3.7.1)

m. The tube was filled to a depth of 0.25 m with spherical glass beads with a nominal diameter of $D = 0.002$ m (Fig. 3.7.1a). The porosity of the medium was measured as $\epsilon = 0.37 \pm 0.02$, and the permeability was found to be $\kappa = (3.13 \pm 0.2) \times 10^{-9}\,\mathrm{m}^2$. A volume of glycerine ($6.78 \times 10^{-5}\,\mathrm{m}^3$) was poured onto the top of the medium as rapidly as possible. The depth of the poured glycerine, above top of the bed, was measured to be initially as $h_0 = 0.075$ m. The kinematic viscosity was given as $9.06 \times 10^{-4}\,\mathrm{m^2 s^{-1}}$.

In the simulations, the density of the fluid was assumed to be $\rho = 1260\,\mathrm{kg\,m^{-3}}$ (*Association et al.*, 1963). The initial spacing between fluid particles ($\Delta x = \Delta y$) was set to 0.001 m, with total number of fluid particles equal to 2550. The smoothing length, h, was $1.2\Delta x$, and the time step was 5×10^{-6} s. No-slip boundary conditions were imposed at the wall boundaries. The pore scale Reynolds number, $Re = uD/\nu$, was calculated as $Re = 3 \times 10^{-4}$. Since the pore scale Reynolds number was much lower than unity, the quadratic term of the drag force in Eq. (3.4) was neglected. The porosity was set to $\epsilon = 0.37$ and the linear gradual change from 1 to 0.37 (section 3.4.4) was imposed at the transition layer, with a depth of $\delta_\epsilon = 0.0072\,m$. Not using this transition layer caused numerical instability, likely due to the sudden change in porosity. The permeability value was set to $\kappa = 3.13 \times 10^{-9}\,\mathrm{m}^2$ as given in the experiment.

In EISPH, the viscous term was calculated as in Eq. (3.26), and the dynamic viscosity was calculated to be $\mu = 1.14\,\mathrm{Pa}\cdot\mathrm{s}$. In δ-SPH, the viscosity was calculated using the artificial viscosity as in Eq. (3.27), with α equal to 0.02 and c_0 equal to 20. The quintic kernel function (see section 3.2.2) was used in both schemes.

The fluid was released over the porous medium at $t = 0\,\mathrm{s}$ and it started to percolate into the porous medium. The residual fluid level above the porous medium throughout the simulation is given by h and the percolated depth of the fluid within the porous medium is given by l (Fig. 3.7.1b). Due to the very small velocity of the fluid, the pressure distribution can be assumed to be hydrostatic (Fig. 3.7.1b). Its value above the porous medium is (*Acton et al.*, 2001)

$$p(Y,t) = p_0 + \rho g(h + 0.25 - Y), \tag{3.69}$$

and inside the porous medium is

$$p(Y,t) = p_0 + \rho g h(1 + (0.25 - Y)/l), \tag{3.70}$$

with p_0 assumed to be zero.

Fig. 3.10 shows the simulated pressure values for both schemes. The change in the porosity of the media (from $\epsilon = 1$ to $\epsilon = 0.37$) is evident from the particles moving apart at the surface of the porous medium ($Y = 0.25$ m), and this appears to be correctly handled. Fig. 3.11 shows pressure values at two elevations, ± 0.02 m from the interface. These values were calculated as the average of the pressure values of the particles within a distance equal to a smoothing length above and below the measurement level. The theoretical pressure values were determined using Eqs. (3.69) and (3.70), and measured fluid depths given in (*Acton et al.*, 2001). As shown in Fig. 3.11, the both schemes reproduced smooth pressure pattern, with EISPH reproducing pressure values comparatively closer to the theoretical values.

Fig. 3.12a shows the drainage of the fluid through the porous medium, $(h_0 - h)$, and Fig. 3.12b shows porosity multiplied by the percolated depth of the fluid within the porous medium, ϵl, as a function of time. Both schemes were able to reproduce the observed data in *Acton et al.* (2001). As shown in Fig. 3.12, the change of volume of glycerine in the free flow domain is nearly equal to the change of volume occupied by glycerine in the porous medium (i.e., $h_0 - h \approx \epsilon l$). The error in volume conservation (the

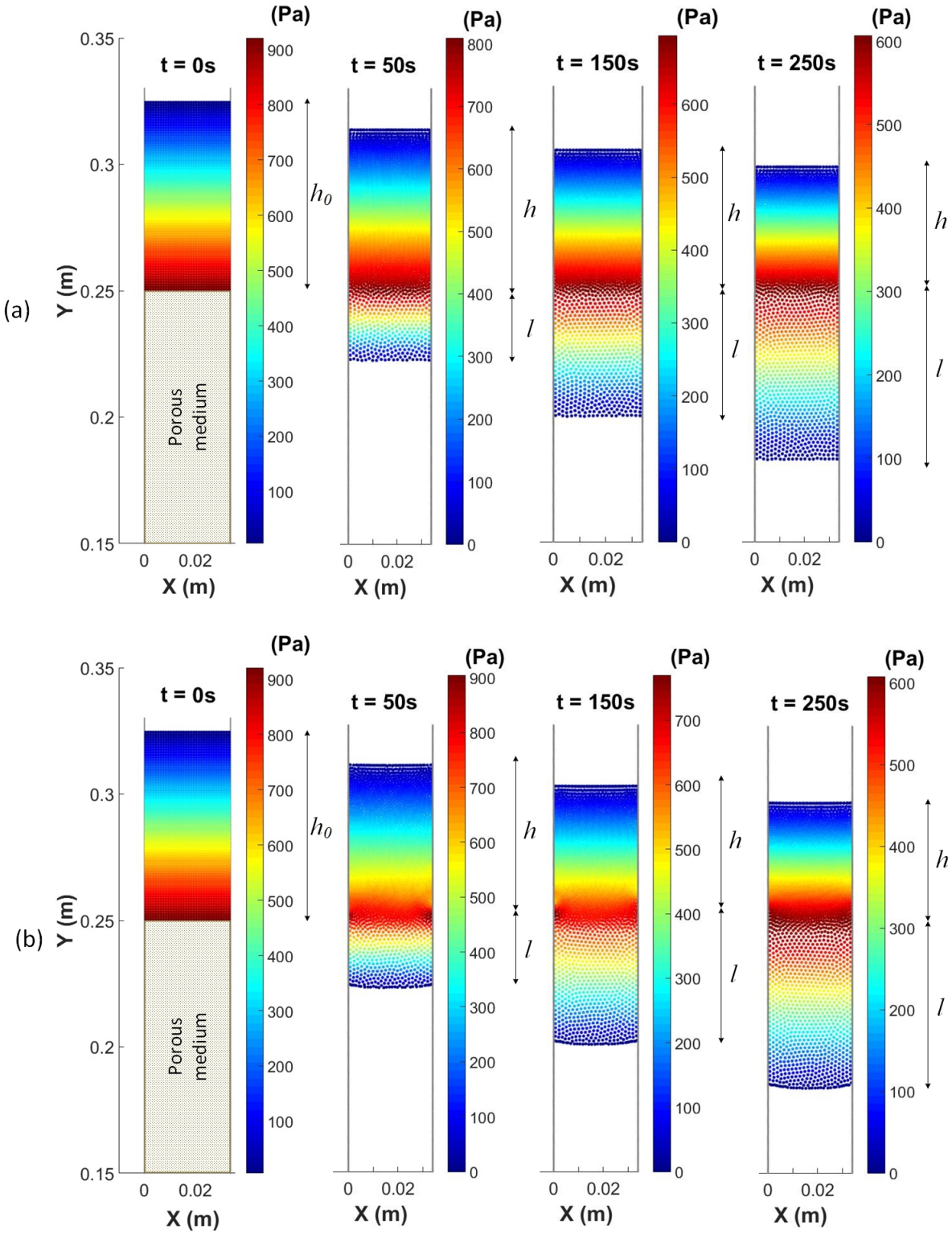

Figure 3.10: Simulated pressure distribution in the column of glycerine percolating through a porous medium 0.25 m deep with a) EISPH and b) δ-SPH.

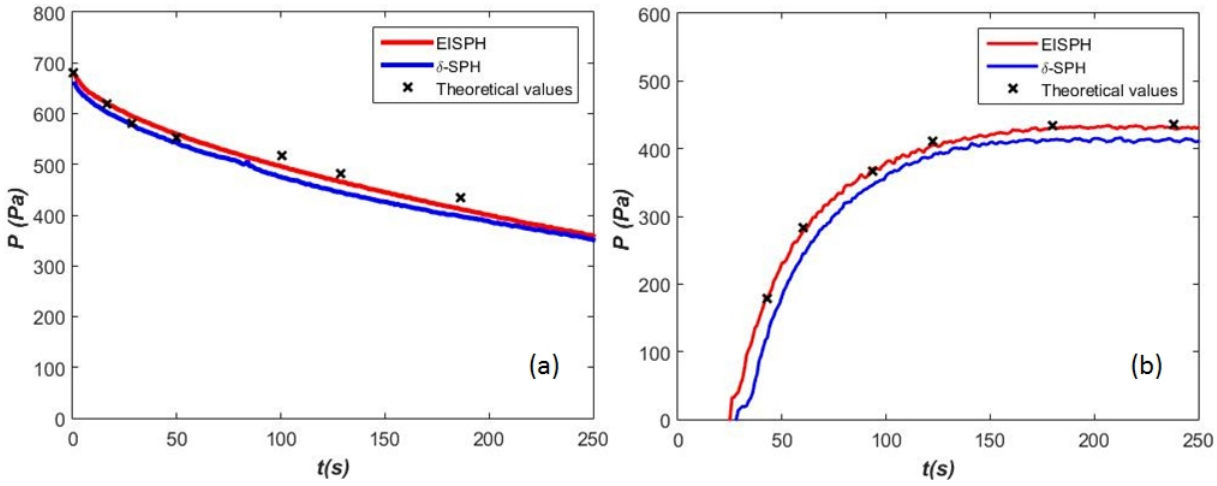

Figure 3.11: Comparison of the time evolution of pressure between EISPH and δ-SPH at (a) 0.02 m above and (b) 0.02 m below the porous medium.

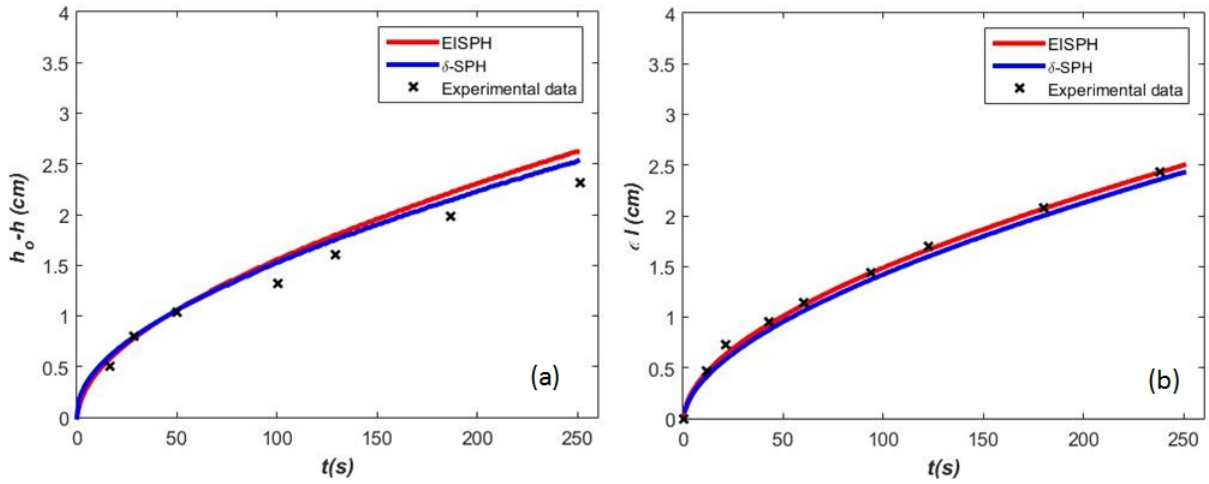

Figure 3.12: (a) Time evolution of drainage of glycerine over the porous medium and (b) porosity times percolated depth of glycerine within the porous medium in the test case in Fig. 3.10

slight deviation between $h_0 - h$ and ϵl) might be due to the approach used to model the interface between domains with different porosities; this requires further study.

In conclusion, both schemes reproduced satisfactorily results for fluid flow across media with different porosities. However, the EISPH scheme led to pressure values comparatively closer to the theoretical data. Additionally, the EISPH uses real viscosity term, in contrast to the artificial viscosity in δ-SPH, which better takes into account the physical properties of fluids. Furthermore, the δ-SPH scheme uses numerical parameters such as speed of

sound, the parameters in approximating the viscous term of the momentum equation and the parameter in the continuity equation. These parameters are often recommended by numerical experiments and varies depending on the application (*Molteni and Colagrossi*, 2009; *Marrone et al.*, 2011). Due to these reasons, EISPH was selected to develop a model of multi-fluid flow in porous media.

3.8 Sink approximations

To carry out SPH simulations of problems such as seawater upconing below extraction wells, a method to describe a sink for the extraction of water mass must be developed.

In a point sink, such as suction or pumping acting at a point, the fluid surrounding the sink point moves toward the sink point. In SPH, this means that fluid particles should move toward the sink point and a portion of the fluid's mass should be removed at a rate equal to the sink rate. The extraction of the mass from a point is included in the continuity equation (Eq. 3.1) (*Bear and Bachmat*, 2012) in the form of fluid flux per unit of volume, Γ, and is approximated as

$$\Gamma = \sum_{k=1}^{s} Q_k \delta(\vec{x} - \vec{x}_k), \tag{3.71}$$

where k is the k^{th} sink point, s denotes the number of sink points, Q is the sink rate and δ is the Dirac function. Eq. (3.71) describes fluid flux per unit volume due to sinks. The contributions of sinks for particle i is approximated as

$$\Gamma_i = \sum_{k=1}^{s} Q_k \delta(\vec{x}_i - \vec{x}_k) \approx \sum_{k=1}^{s} Q_k \zeta_k W_{ik}, \tag{3.72}$$

where ζ is a normalization factor equivalent to an approximation of constant 1 and defined as (*Monaghan et al.*, 2005; *Monaghan*, 2005)

$$\frac{1}{\zeta_k} = \sum_{j=1}^{N} \frac{m_j}{\epsilon_j \rho_j} W_{jk}. \tag{3.73}$$

In Eq. (3.72), sink points within a distance equal to the radius of the support of the kernel function from particle i are detected to calculate Γ; therefore, a sink point directly affects the particles (sink particles hereafter) inside the support domain at the sink point.

The particles outside the direct influence of the sink point are indirectly affected through their interaction with the sink particles.

The term Γ contributes to the pressure Poisson equation (Eq. 3.39), causing the pressure of the particles surrounding the sink point to change in a way that they move towards the sink point.

Each particle in SPH carries a certain amount of fluid mass and in order to account for the mass extraction due to the sink, particles mass must be reduced and particles deleted where and when necessary. Three different methods for deleting particles are proposed to investigate their advantages and disadvantages.

3.8.1 Solely Particle Removal (SPR)

In this method, the mass reduction due to the sink is handled by just deleting particles. One particle is deleted after a certain number of time steps. The duration, t_p, required to delete one particle is determined using the volume of fluid in a particle and the sink rate, such that

$$t_p = \frac{\epsilon V}{Q} \tag{3.74}$$

where V is a spatial volume associated with a particle, and ϵV is the volume of fluid that each particle carries. Mass is reduced (i.e., one particle is removed) at every time step that is a multiple of t_p (i.e., at times $t = \alpha t_p$, α being an integer). Every time $t = \alpha t_p$, the particle closest to the sink point is removed (Fig. 3.13a).

Because the sink particles move toward the sink point due to the inclusion of Γ in the pressure Poisson equation (Eq. 3.39), the particle deletion does not lead to a void in the vicinity of the sink point.

3.8.2 Mass Reduction and Particle Removal (MRPR)

Similar to *SPR*, one particle is removed every certain number of time steps. However, differently from *SPR*, the mass of sink particles is gradually reduced every time step before one particle is deleted. The amount of mass required to be removed in one time step is divided among the sink particles and reduced from the mass of the particles. The division of the mass, required to be removed, among the sink particles is handled in two ways to investigate their advantages and disadvantages; (1) in accordance to the kernel value ($MRPR_K$), so that the particle closer to a sink point loses more mass than the

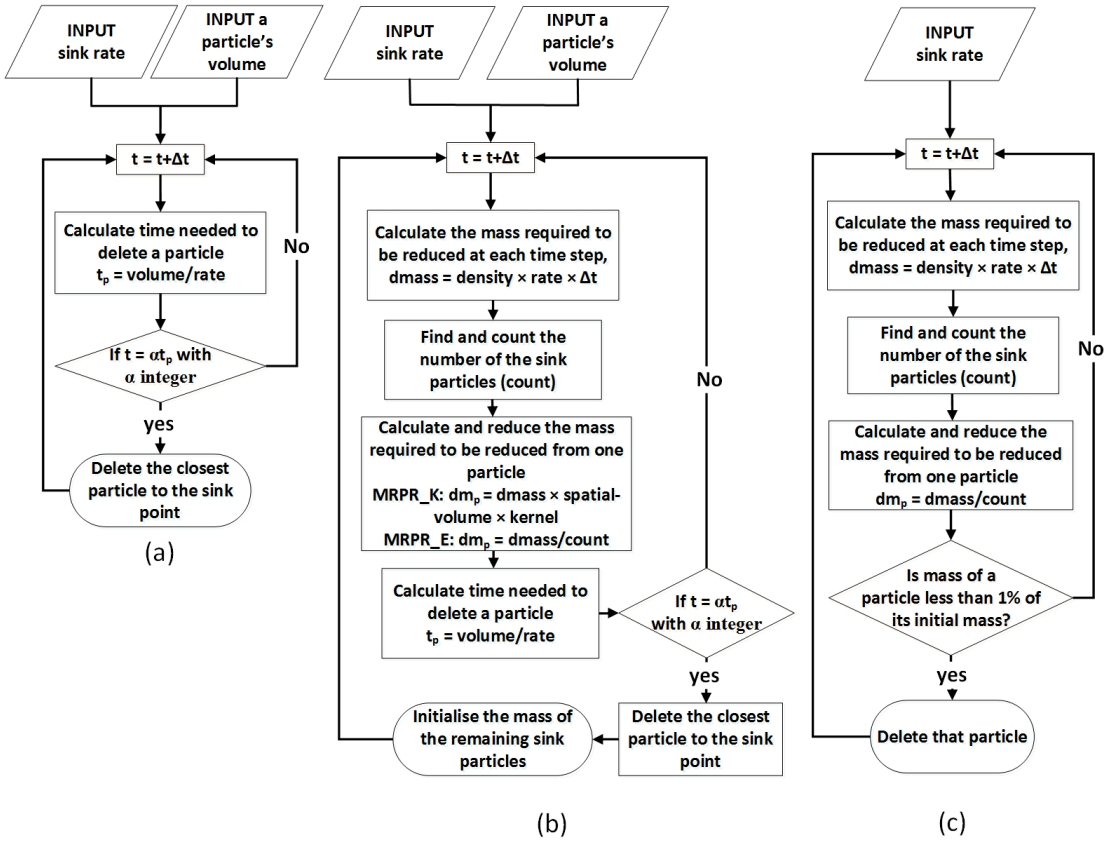

Figure 3.13: The procedure for the reduction of mass due to a sink point using (a) Solely Particle Removal (SPR), (b) Mass Reduction and Particle Removal (MRPR) and (c) Constant Mass Reduction (CMR).

more distant ones (2) evenly ($MRPR_E$). Therefore, the amount of the mass reduced from each particle is determined using the sink rate, time step value, kernel value (used in $MRPR_K$), and number of sink particles (used in $MRPR_E$). When the time required to delete one particle, αt_p, is reached, the closest particle to the sink point is removed and the mass of the remaining sink particles is set back to their initial mass value (Fig. 3.13b).

3.8.3 Constant Mass Reduction (CMR)

In this method, the mass of the sink particles is gradually reduced every time step, as in *MRPR*. The reduction of the mass of the sink particles continues until the mass of a sink particle drops below a cut-off value, which here is set to 1% of particles initial mass value, below which the particle is removed (Fig. 3.13c).

CHAPTER 4

SPH modelling of multi-fluid lock-exchange over and within porous media

This chapter comprises the published paper:
Basser, H., Rudman, M., & Daly, E. (2017). SPH modelling of multi-fluid lock-exchange over and within porous media. Advances in Water Resources, 108, 15-28.
The paper won the 2017 best departmental research paper award.

4.1 Introduction

Multi-fluid flow over and within porous media is ubiquitous in nature and engineering applications. The SPH modeling of these flows and validation against observations have not been largely conducted in literature. The explicit numerical scheme for incompressible fluid using Smoothed Particle Hydrodynamics (EISPH) (section 3.6.1) was employed due to its advantages compared to the δ-SPH scheme. Two integration algorithms, e.g. Euler and Heun (see section 3.6.1), were employed to integrate the SPH schemes and investigate a possible effect of the integration methods on the results.

To validate the model and explore its advantages and disadvantages, case studies including percolation of a single fluid in a porous medium, gravity current of a single fluid over a porous medium, multi-fluid flow over an impermeable bed, and a porous medium were simulated and compared with experimental data.

The section associated with the methods in the paper is also included in chapter 3 of this thesis. Furthermore, some parts of one of the case studies in the paper (section 3.1 in the paper) was also presented in section 3.7 of this thesis.

4.2 Published paper

See the published paper starting from the following page.

Advances in Water Resources 108 (2017) 15–28

Contents lists available at ScienceDirect

Advances in Water Resources

journal homepage: www.elsevier.com/locate/advwatres

SPH modelling of multi-fluid lock-exchange over and within porous media

Hossein Basser[a,*], Murray Rudman[b], Edoardo Daly[a]

[a] Department of Civil Engineering, Monash University, VIC 3800, Australia
[b] Department of Mechanical and Aerospace Engineering, Monash University, VIC 3800, Australia

ARTICLE INFO

Article history:
Received 21 April 2017
Revised 20 July 2017
Accepted 20 July 2017
Available online 21 July 2017

Keywords:
Smoothed particle hydrodynamics
Explicit incompressible SPH
Multi-fluid flow
Porous media

ABSTRACT

Multi-fluid flow over and within porous media occurs frequently in nature and plays an important role in engineering applications. The modeling of these flows and validation against experimental or field observations have not been largely conducted in literature. An explicit numerical scheme for incompressible fluid using Smoothed Particle Hydrodynamics (EISPH) was employed and solved using two integration algorithms. To explore the capabilities and limitations of the model, case studies including percolation of a single fluid in a porous medium, gravity current of a single fluid over a porous medium, multi-fluid flow over an impermeable bed, and a porous medium were simulated and compared with experimental data. The EISPH method led to results overall similar to the observed experimental data. The model was able to reproduce the behaviour of the flow within media with different porosities. In addition, the model reproduced behaviour of multi-fluid flow at the interface between different fluids, such as reproducing Kelvin–Helmholtz vortices and diffusion of salt.

1. Introduction

A gravity current is a multi-fluid flow that occurs due to a density difference between fluids (Huppert, 2006; Simpson, 1982). Gravity currents often occur in the presence of porous media, and play a crucial role in a variety of natural and industrial processes, such as sea water intrusion into groundwater, carbon dioxide migration in groundwater (Zhao et al., 2013) and oil recovery through water flooding in petroleum reservoirs (Coutinho et al., 2008).

Gravity currents have been often studied using lock-exchange laboratory experiments, where a dense fluid is released into an ambient fluid via removal of a lock. These experiments mostly focused on the front velocity and often referred to flow over an impermeable bed (Adduce et al., 2011; Lowe et al., 2005; Rottman and Simpson, 1983), although some experiments have been conducted in porous media (Acton et al., 2001; Huppert and Woods, 1995; Thomas et al., 2004). Although experimental studies have helped to explore the behaviour of gravity currents, they suffer from disadvantages such as the difficulty in up-scaling to dimensions suitable for practical applications, and in porous media the opaqueness of the media makes it difficult to observe the dynamics of the flow (Thomas et al., 2004). Therefore, analytical models and computational techniques have been developed.

Shallow water equations are the base of most analytical solutions proposed for lock-exchange flows (Rotunno et al., 2011; Ungarish and Huppert, 2002). These equations can reproduce the key features of the flow, such as front position and speed; however, the interaction of the flow with boundaries and diffusion between fluids are not well captured (Rotunno et al., 2011). Alternatively, the Navier–Stokes equations, including a diffusion equation for the density variations, have been employed to study these flows in further detail (Birman et al., 2005; Cantero et al., 2007). From a numerical point of view, the main modelling challenges in these complex flows are handling the discontinuity in flow behaviour at the interface between the fluids and porous media, the abrupt discontinuity in fluid properties such as density for immiscible fluids, and the potentially complex geometry of the interface. To tackle these problems, it is necessary to track and recognise the interfaces; this, however, can be computationally expensive in grid based numerical methods. Therefore, there has been a rising interest in using meshless methods, such as Smoothed Particle Hydrodynamics (SPH)(Liu and Liu, 2003).

SPH is a fully Lagrangian meshless method that has shown good accuracy for many computational fluid dynamics applications (Liu and Liu, 2003). Due to its Lagrangian nature, it has been recently applied to multi-fluid flows with interfaces (Monaghan and Rafiee, 2013; Shao, 2013); however, it still requires extensive vali-

* Corresponding author.
E-mail address: hossein.basser@monash.edu (H. Basser).

http://dx.doi.org/10.1016/j.advwatres.2017.07.011
0309-1708/

dation against experimental data or high quality benchmark tests (Violeau and Rogers, 2016). SPH algorithms have been tested successfully for multi-fluid flows with high density ratios (Lind et al., 2015; Mokos et al., 2015; Monaghan and Rafiee, 2013), but their application to multi-fluid flows with small density ratios has not been widely studied (Pahar and Dhar, 2016a). The ability of SPH to simulate multi-fluid flow with density ratio close to one has been tested with some modifications to the Navier–Stokes equations, using a pressure decoupling formula and Boussinesq approximation, in confined flows; however, its application in free surface flows requires further improvement (Ghasemi et al., 2013; Leroy et al., 2015).

SPH has also been employed to model fluid flow in porous media. Some studies focused on pore-scale flow (Kunz et al., 2016; Tartakovsky et al., 2016), soil and water interaction (Fourtakas and Rogers, 2016), and, more in engineering applications, flow in fully saturated media has been considered (Bui et al., 2007; Shao, 2010), with encouragement for further validation. The behaviour of the flow at the interface between porous media with different porosities has not been well investigated. Recently, a corrected SPH algorithm has been proposed to solve the fluid flow in porous media, focusing on the behaviour of the flow moving between different media (Akbari, 2014). This algorithm needs a strong validation against experimental observations.

Despite the increasing interest in SPH for modelling multi-fluid flows and fluid flow in porous media, the simultaneous modelling of a multi-fluid flow that occurs over or within a porous medium has not been largely studied. Developing a method to simulate multi-fluid flows in media with different porosities is important to study natural and man-made events, such as seawater intrusion in groundwater (Zhao et al., 2013) and release of sewage liquids nearby coasts (Thomas et al., 2004), that often occur in media with heterogeneous porosity.

The contribution of this study is to bring together SPH schemes for multi-fluid flow and flow in porous media to generate a model capable of simulating multi-fluid flow in porous media at scales significantly larger than pore scale. Most studies employ weakly compressible SPH (WCSPH) or incompressible SPH (ISPH) schemes. The ISPH method is preferred owing to its more accurate pressure prediction (Violeau and Rogers, 2016). However, ISPH is computationally expensive as the Poisson equation to calculate pressure must be solved implicitly (Nomeritae et al., 2016). To overcome this high computational cost, explicit incompressible SPH (EISPH) has been proposed and has shown the capability in reproducing experimental data for various applications (Hosseini et al., 2007a; Nomeritae et al., 2016; Rafiee and Thiagarajan, 2009). The EISPH method is used in this study for its computational efficiency. The credibility of the model is tested against data from experiments available in the literature.

2. Methods

This section describes the Navier–Stokes equations for multi-fluid flows in porous media with a spatially varying porosity, $\epsilon(\vec{x})$. In this study, $\epsilon(\vec{x})$ is fixed in time; however, this condition can be relaxed without much additional complexity.

2.1. Governing equations

The governing equations for a flow of two or more incompressible fluids with different densities in a medium with porosity changing in space are Akbari (2014), Pahar and Dhar (2016a), Pahar and Dhar (2016c)

$$\nabla \cdot \vec{u} = 0, \tag{1}$$

$$\frac{D\vec{u}}{Dt} = -\frac{\epsilon}{\rho}\nabla p + \frac{\mu}{\rho}\nabla^2\vec{u} + \epsilon\vec{g} + \vec{R}, \tag{2}$$

$$\frac{DC}{Dt} = \mathcal{D}_e\nabla^2 C, \tag{3}$$

where $\vec{u}$ is the Darcian velocity equal to $\epsilon\vec{u}_f$, $\vec{u}_f$ being the fluid intrinsic velocity, ρ is the fluid density, p is pressure, μ is the dynamic viscosity, $\vec{g}$ is the gravitational acceleration, $\mathcal{D}_e$ is the effective coefficient of diffusivity, which depends on the flow regime, fluid and scalar properties and characteristics of the porous media, and C is concentration of a solute such as salt. Variations of fluid density were assumed to be a direct function of C as $\rho = f(C)$, where the form of the function f is defined according to the physics of the scenario being modelled. C is assumed to be an indicator function here, with $-0.5 \le C \le 0.5$ where $C = -0.5$ and $C = 0.5$ correspond to the minimum and maximum density, respectively. C relates to density as

$$\rho = C(\rho_d - \rho_l) + 0.5(\rho_d + \rho_l), \tag{4}$$

where ρ_d and ρ_l are the maximum and minimum densities, respectively. This function is more beneficial from a numerical point of view (Ghasemi et al., 2013). C will be referred to as concentration hereafter.

When a fluid passes through a porous medium, the solid matrix of the medium generates a resistance to the fluid motion. This drag force consists of a linear (Darcy) and a quadratic (Forchheimer) term as Nield (2000)

$$\vec{R} = -\frac{\epsilon\mu}{\rho\kappa}\vec{u} - \frac{\epsilon c_F}{\kappa^{1/2}}|\vec{u}|\vec{u}, \tag{5}$$

where κ is the permeability of the media through which the flow occurs, and c_F is the dimensionless Forchheimer coefficient. The Darcy term is dominant in flows with a pore scale Reynolds number lower than unity (Nield, 2000). For larger Reynolds numbers, the quadratic term dominates due to inertial effects (Joseph et al., 1982). In the absence of a porous medium, $\epsilon = 1$ and $\kappa \to \infty$, such that both terms on the right hand side of Eq. (5) are zero. A detailed derivation of the continuity and momentum equations are reported in the appendix of Pahar and Dhar (2016c).

2.2. SPH approximation

A brief overview of SPH is provided here, but more detailed expositions can be found in Monaghan (1992); 1994); 2005). In SPH, fluids are discretised as ensembles of Lagrangian particles that interact with each other. The values of variables associated with each particle are approximated using the values of the same variables of surrounding particles. The contribution of each particle to the approximation of the variable is determined by interpolation using a weighting function (Liu and Liu, 2003). A generic function $f(\vec{x})$ is approximated as Monaghan (1992)

$$f(\vec{x}_i) = \sum_{j=1}^{N} V_j f(\vec{x}_j) W(|\vec{x}_i - \vec{x}_j|, h), \tag{6}$$

where j (1,... , N) denotes particle labels, V_j represents the spatial volume of particle j, W is the kernel weighting function, the value of which depends on the distance between particles, $|\vec{x}_i - \vec{x}_j|$, h is a smoothing length that controls the support domain of the kernel function, with a radius equal to λh, λ being a coefficient that depends on the order of the kernel, and N is the number of particles within the support domain.

A quintic spline weighting function (Liu and Liu, 2003; Morris, 1996) was used here because, for the cases analysed, it led to more

stable pressure values than a cubic B-spline (Monaghan and Lattanzio, 1985). The quintic function is

$$W(q,h)=\alpha_d\times\begin{cases}(3-q)^5-6(2-q)^5+15(1-q)^5 & 0\le q<1\\ (3-q)^5-6(2-q)^5 & 1\le q<2\\ (3-q)^5 & 2\le q<3\\ 0 & q>3,\end{cases} \tag{7}$$

where α_d is a normalisation constant equal to $1/(120h)$, $7/(478\pi h^2)$, and $3/(359\pi h^3)$ in one-, two- and three-dimensional domains, respectively, and $q=|\vec{x}_i-\vec{x}_j|/h=|\vec{x}_{ij}|/h$.

The gradient of a function $f(\vec{x})$ can be approximated as Monaghan (1992)

$$\nabla f(\vec{x}_i)=\sum_{j=1}^{N}V_j f(\vec{x}_j)\nabla_i W_{ij}=\sum_{j=1}^{N}V_j f(\vec{x}_j)\frac{\vec{x}_{ij}}{|\vec{x}_{ij}|}\frac{\partial W_{ij}}{\partial|\vec{x}_{ij}|}, \tag{8}$$

where $W_{ij}=W(|\vec{x}_i-\vec{x}_j|,h)$.

2.2.1. Spatial volume

Since the flow can occur in media with different porosities, particular care needs to be paid to the definition of spatial volume. Porosity is defined to be a function of position ($\vec{x}$) and thus the value of porosity assigned to a particle is only dependent on the particles' position. When particle j is not in a porous medium ($\epsilon=1$), the volume of the particle, V_p, is $V_{pj}=m_j/\rho_j$. When the particle enters a porous medium, the same mass of fluid occupies a larger volume, V_j, referred to as spatial volume here, that accounts for both fluid and solid volumes, so that $m_j=\rho_j V_j\epsilon_j$, with $V_{pj}=\epsilon_j V_j$. In this study, the mass associated with each particle is kept constant, except for mass change due to diffusion (Eq. 3); therefore, the spatial volume (i.e., the space) associated with each particle is Pahar and Dhar (2016b)

$$V_j=\frac{m_j}{\epsilon_j\rho_j}. \tag{9}$$

If the density changes due to variations in scalar concentration, the mass of fluid associated with particle j should be changed as $m_j=\rho_j\epsilon_j V_j=\rho_j V_{pj}$.

The spatial volume associated with each particle depends on the porosity of the medium. Therefore, the spatial volume of particles inside a porous medium is expected to be larger than that of particles within a fluid domain; this leads to a coarser resolution inside the porous medium (Pahar and Dhar, 2016b). In order to keep the number of particles inside the support domain in a certain range, the smoothing length should be adjusted according to the value of porosity. However, having a variable smoothing length adds extra terms involving the derivative of smoothing length in the momentum equation (Price and Monaghan, 2004). Another approach is using a larger support domain to occupy a sufficient number of particles. The quintic kernel (Eq. 7) has a larger support domain compared to more commonly used kernels, such as cubic spline, and is used here to avoid this problem.

2.2.2. Numerical scheme

EISPH was adopted to solve the governing equations (Nomeritae et al., 2016). A two step, prediction-correction projection method (Cummins and Rudman, 1999), with an approximate solution of the Poisson equation, was employed to calculate velocity and particle position of each particle at each time step. A time integration algorithm that is first order in time for velocity and second order in time for particle position was used. Although the algorithm is not totally first order, it will be referred as an Euler algorithm hereinafter.

In the prediction step, an intermediate velocity ($\vec{u}^*$) is calculated as

$$\vec{u}_i^*=\vec{u}_i^n+\left(\frac{\mu}{\rho}\nabla^2\vec{u}\right)_i^n\Delta t+\epsilon_i^n\left(\vec{g}-\frac{\mu}{\rho\kappa}\vec{u}-\frac{c_F}{\kappa^{1/2}}|\vec{u}|\vec{u}\right)_i^n\Delta t, \tag{10}$$

where $\vec{u}^n$ is particle velocity at time $n\Delta t$, with Δt constant throughout the simulations.

The viscous term is approximated as Shao and Lo (2003)

$$\left(\frac{\mu}{\rho}\nabla^2\vec{u}\right)_i^n=\sum_{j=1}^{N}\frac{4m_j^n(\mu_i+\mu_j)\vec{u}_{ij}^n\cdot\vec{x}_{ij}^n}{\epsilon_j^n(\rho_i^n+\rho_j^n)^2\left(|\vec{x}_{ij}^n|^2+\eta^2\right)}\nabla_i W_{ij}{}^n, \tag{11}$$

where η is a small parameter included to ensure that the denominator remains non-zero ($\eta=0.001h_{ij}$, with $h_{ij}=(h_i+h_j)/2$), and $\vec{u}_{ij}^n=\vec{u}_i^n-\vec{u}_j^n$. The gravitational and drag terms are calculated directly, with the drag term calculated only for particles inside a porous medium.

The intermediate positions ($\vec{x}^*$) are calculated using the intermediate intrinsic velocity of the particles as

$$\vec{x}_i^*=\vec{x}_i^n+\frac{\vec{u}_i^*}{\epsilon^n}\Delta t, \tag{12}$$

where $\vec{x}^n$ is particle position at time $n\Delta t$. Afterwards, the intermediate porosity of particles, ϵ^*, associated with the intermediate position is assigned.

In the correction step, the pressure of the particles is calculated in a way to approximately satisfy incompressibility. The velocity of a particle at time $(n+1)\Delta t$ is

$$\vec{u}_i^{n+1}=\vec{u}_i^*-\frac{\epsilon_i^*}{\rho_i^n}\nabla p_i^{n+1}\Delta t, \tag{13}$$

where p^{n+1} is particle pressure at time $(n+1)\Delta t$. Combining Eqs. (1) and (13) yields the pressure Poisson equation

$$\nabla\cdot\left(\frac{\epsilon^*}{\rho^n}\nabla p^{n+1}\right)_i=\left(\frac{\nabla\cdot\vec{u}^*}{\Delta t}\right)_i. \tag{14}$$

The divergence of the intermediate velocity is the source term for the pressure Poisson equation, and is approximated using Eq. (8) as Pahar and Dhar (2016b)

$$(\nabla\cdot\vec{u}^*)_i=\sum_{j=1}^{N}\frac{m_j^n}{\epsilon_j^*\rho_j^n}(\vec{u}_j^*-\vec{u}_i^*)\cdot\nabla_i W_{ij}^*. \tag{15}$$

The Laplacian operator in Eq. (14) is expressed using an approximation of the second derivative (Monaghan, 2005) and reads

$$\nabla\cdot\left(\frac{\epsilon^*}{\rho^n}\nabla p^{n+1}\right)_i=\sum_{j=1}^{N}\frac{m_j^n}{\epsilon_j^*\rho_i^n\rho_j^n}\frac{\left(\epsilon_i^*+\epsilon_j^*\right)\vec{x}_{ij}^*\cdot\nabla_i W_{ij}^*}{|\vec{x}_{ij}^*|^2+\eta^2}\left(p_i^{n+1}-p_j^{n+1}\right), \tag{16}$$

so that

$$\sum_{j=1}^{N}\frac{m_j^n}{\epsilon_j^*\rho_i^n\rho_j^n}\frac{\left(\epsilon_i^*+\epsilon_j^*\right)\vec{x}_{ij}^*\cdot\nabla_i W_{ij}^*}{|\vec{x}_{ij}^*|^2+\eta^2}\left(p_i^{n+1}-p_j^{n+1}\right)=\left(\frac{\nabla\cdot\vec{u}_*}{\Delta t}\right)_i. \tag{17}$$

Eq. (17) can be written for particle i as

$$p_i^{n+1}=\frac{B_i+\sum_{j=1}^{N}A_{ij}p_j^{n+1}}{\sum_{j=1}^{N}A_{ij}}, \tag{18}$$

with

$$A_{ij}=\frac{m_j^n}{\epsilon_j^*\rho_i^n\rho_j^n}\frac{\left(\epsilon_i^*+\epsilon_j^*\right)\vec{x}_{ij}^*\cdot\nabla_i W_{ij}^*}{|\vec{x}_{ij}^*|^2+\eta^2}, \tag{19}$$

and

$$B_i=\left(\frac{\nabla\cdot\vec{u}^*}{\Delta t}\right)_i. \tag{20}$$

Considering a small time step, the value of p_j^{n+1} on the right hand side of Eq. (18) in EISPH is assumed to be equal to p_j^n, so that the pressure of each particle can be approximated explicitly as Nomeritae et al. (2016), Hosseini et al. (2007)

$$p_i^{n+1} = \frac{B_i + \sum_{j=1}^{N} A_{ij} p_j^n}{\sum_{j=1}^{N} A_{ij}}. \tag{21}$$

This is an approximation that is equivalent to diagonalising the Poisson problem matrix and was shown to work for various applications (Nomeritae et al., 2016). Since in the cases analysed here no negative pressure was expected physically, possible negative pressures arising from small numerical errors are set to zero.

The initial pressure value of the free surface particles are set to zero. Therefore, the pressure of free surface particles from the previous time step is always equal to zero. However, when pressure at the new time step is calculated, its value for the free surface particles might be non-zero and needs to be re-set to the free surface boundary condition. Therefore, after the calculation of pressure using Eq. (21), the pressure of particles of the free surface is imposed to be equal to zero. The determination of the free surface particles is explained in Section 2.2.4. The pressure calculated from Eq. (21) is used in Eq. (13) to calculate $\vec{u}_i^{n+1}$. The pressure gradient is calculated as

$$\left(\frac{\epsilon^*}{\rho^n}\nabla p^{n+1}\right)_i = \epsilon_i^* \sum_{j=1}^{N} \frac{m_j^n}{\epsilon_j^*}\left(\frac{p_i^{n+1}}{\rho_i^{n2}} + \frac{p_j^{n+1}}{\rho_j^{n2}}\right)\nabla_i W_{ij}^*. \tag{22}$$

Once $\vec{u}_i^{n+1}$ is determined, the new position is then calculated as

$$\vec{x}_i^{n+1} = \vec{x}_i^n + \frac{\left(\frac{\vec{u}_i^n}{\epsilon_i^n}\right) + \left(\frac{\vec{u}_i^{n+1}}{\epsilon_i^*}\right)}{2}, \tag{23}$$

and new particle porosity, ϵ^{n+1}, associated with the new position is assigned. Afterwards, the new concentration of each particle is calculated using Eq. (3) as Pahar and Dhar (2016a)

$$C_i^{n+1} = C_i^n + \left(\mathcal{D}_e \nabla^2 C\right)_i \Delta t, \tag{24}$$

with Ghasemi et al. (2013), Zhu and Fox (2001)

$$\left(\mathcal{D}_e \nabla^2 C\right)_i = \sum_{j=1}^{N} \frac{m_j^n}{\epsilon_j^{n+1}\rho_j^n} \frac{(\mathcal{D}_{ei}^{n+1} + \mathcal{D}_{ej}^{n+1})\vec{x}_{ij}^{n+1} \cdot \nabla_i W_{ij}^*}{|\vec{x}_{ij}^{n+1}|^2 + \eta^2}\left(C_i^n - C_j^n\right). \tag{25}$$

The effective diffusivity coefficient, $\mathcal{D}_e$, is determined in accordance with flow regime and the porosity of a medium using an empirical equation, assuming the porous medium is saturated (Simunek and Suarez, 1993), as

$$\mathcal{D}_{ei}^{n+1} = (D_{mi} + D_{ti})(\epsilon_i^{n+1})^{4/3}, \tag{26}$$

where D_m and D_t are coefficients of molecular and turbulent eddy diffusivity, respectively. D_t is only added for flows with Reynolds numbers higher than 1000 (Simpson, 1997). Subsequently, density and the mass of each particle are updated as Pahar and Dhar (2016a)

$$\rho_i^{n+1} = C_i^{n+1}(\rho_d - \rho_l) + 0.5(\rho_d + \rho_l), \tag{27}$$

$$m_i^{n+1} = \rho_i^{n+1} V_{pi}. \tag{28}$$

The time step value, Δt, is defined to satisfy the Courant stability and viscous diffusion conditions as

$$\Delta t \leq min(\Delta t_{CFL}, \Delta t_{visc}), \tag{29}$$

with

$$\Delta t_{CFL} \leq 0.25\frac{h}{u_{max}}, \tag{30}$$

and

$$\Delta t_{visc} \leq 0.125\frac{h^2}{\nu}, \tag{31}$$

where $u_{\max}$ is the predicted maximum velocity in the computation and $\nu = \mu/\rho$ is the kinematic viscosity (Morris et al., 1997). The time step used in the simulations was chosen to satisfy these conditions throughout the simulations, and its value was kept constant.

A prediction-correction method (known as Heun's method) was also applied in order to assess the accuracy of the Euler method. The method is second order in time, for both velocity and position, and is described in Appendix A.

2.2.3. Initial conditions

Initial values of velocity, density, mass, concentration, dynamic viscosity, smoothing length, and pressure were assigned to the fluid particles. Initial velocity components were set to zero, and density, mass, and concentration of each particle were assigned according to the fluids' initial properties. Hydrostatic pressure profiles were assumed at the start of each simulation.

2.2.4. Boundary conditions

Different types of particles are used to handle flow, solid boundaries, and boundary conditions. Three types of particles are used: fluid, virtual, and ghost particles. Fluid particles are associated with moving fluids. A single layer of virtual particles is used to identify solid boundaries (Monaghan, 1994). The virtual particles interact only with fluid particles and exert a repulsive force on them as Monaghan (1994)

$$F(\vec{x})_{ij} = \begin{cases} L\left[\left(\frac{r_0}{|\vec{x}_{ij}|}\right)^{p_1} - \left(\frac{r_0}{|\vec{x}_{ij}|}\right)^{p_2}\right]\frac{1}{|\vec{x}_{ij}|} & \frac{r_0}{|\vec{x}_{ij}|} \geq 1, \\ 0 & \frac{r_0}{|\vec{x}_{ij}|} < 1, \end{cases} \tag{32}$$

where p_1 and p_2 are constants equal to 4 and 2 respectively, L is the square of the largest velocity, and r_0 is a cut off distance assumed to be 0.8 times the initial distance between virtual particles. Repulsive forces are applied perpendicularly to the boundaries, and along 45° at corners. The distance between the virtual particles is set to half the initial spacing of the fluid particles to be certain to maintain impermeable boundaries.

Ghost particles are used to impose boundary conditions. For a fluid particle within a distance of 3 h from the solid boundaries, a ghost particle is produced symmetrically on the other side of the boundaries (Liu and Liu, 2003) (Fig. 1(a)). Ghost particles are assigned the same density, concentration, mass, pressure, porosity, dynamic viscosity, effective diffusivity coefficient, and smoothing length as the corresponding fluid particles. To impose free-slip boundary conditions, the component of velocity parallel to the boundary is unchanged, while for no-slip it is reversed. The normal component of the velocity is reversed for both free-slip and no-slip conditions (Marrone et al., 2011) (Fig. 1(b)).

Free-slip or no-slip boundary conditions are used in calculating viscous force (Eq. 11), pressure Poisson equation (Eq. 15 and Eq. 16), pressure gradient (22), and change in the concentration (Eq. 25). Mixed free-slip and no-slip boundary conditions, which are recommended for higher Reynolds numbers, can also be implemented, as the no-slip boundary condition is used in calculating the viscous term in the momentum equation while the free-slip boundary condition is used in calculating the pressure Poisson equation, the pressure gradient and change in concentration (Grenier et al., 2013; Marrone et al., 2013). The mixed boundary condition is called modified no-slip boundary condition here.

A free surface pressure condition is assigned after calculating particle pressure using Eq. (21). Free surfaces are identified using

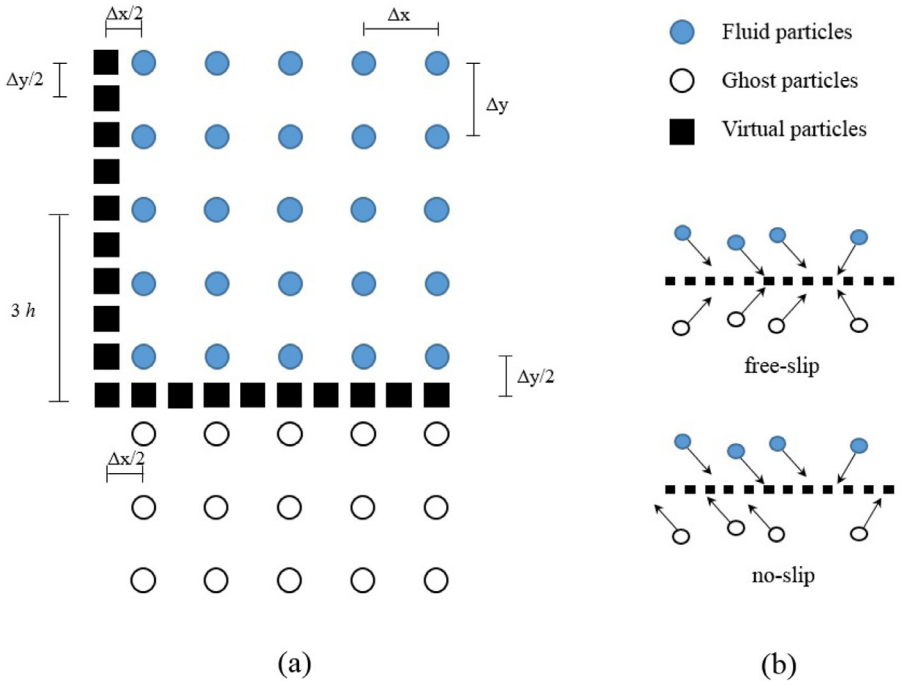

Fig. 1. Schematic representation of (a) virtual particles and initial distribution of fluid particles, and (b) application of free-slip and no-slip boundary conditions.

particle densities. The particle densities are approximated using a density summation (Liu and Liu, 2003) as

$$\rho_i^{\epsilon} = \sum_{j=1}^{N} \frac{m_j}{\epsilon_j} W_{ij}. \tag{33}$$

As the free surface particles reside within a non-complete support domain, their particle density is less than the fluid's initial density. When the density of a particle drops below 99% of its initial density, it is considered as a free-surface particle and zero pressure is assigned to that particle (Shao and Lo, 2003). Eq. (33) is only used to detect free surfaces, as the density of particles during integration are updated only by Eq. (27).

2.3. Interface conditions

When particles move between media with different porosities, the porosity values are assigned depending on the particles' position. However, the geometrical transition at an interface between media is not usually sharp, and a sharp transition may not properly represent the physics of the problem (Duman and Shavit, 2010). Furthermore, based on our investigations this sharp change in porosity may lead to numerical instabilities. Therefore, a gradual change in porosity is usually applied at the interface (Akbari, 2014). In this study, a gradual linear change of porosity is applied at the interface between media with different porosities. As shown in Fig. 2, the porosity linearly changes in a transition layer between a fluid flow domain, $\epsilon = 1$, and a porous medium, $\epsilon = \epsilon_m$. The thickness of the transition layer is assumed to be equal to the diameter of the support domain of the kernel function, $\delta_\epsilon = 2\lambda h$. A sharp interface can also be simulated with no transition layer.

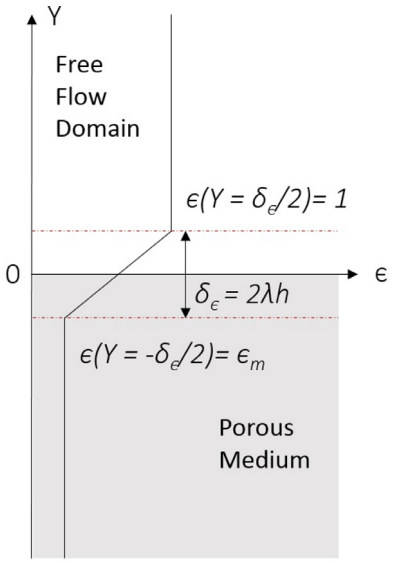

Fig. 2. Definition of the transition layer between a free flow and a porous medium with porosity ϵ_m. The depth of the transition layer, δ_ϵ, equals the diameter of the kernel function, $2\lambda h$.

3. Case studies

In this section the method is applied to four different cases to test different aspects of the method and validate it where possible. The cases are: (a) vertical percolation of a single fluid in a porous medium (Acton et al., 2001) in order to check the accuracy and limitations of the method in modelling a flow moving in media with different porosities, (b) gravity current of a single fluid over a porous medium in order to investigate the credibility of the model to simulate currents propagating over a porous medium (Acton et al., 2001), (c) Boussinesq lock-exchange over an impermeable bed (Adduce et al., 2011) to validate the model for simulating multi-fluid flows focusing on the evolution of the current front and diffusion at the fluids' interface, and (d) Boussinesq lock-exchange over a porous medium (Thomas et al., 2004) to bring together the models of the single fluid flows in porous media and multi-fluid flows over the impermeable bed to simulate a multi-fluid flow in a porous medium.

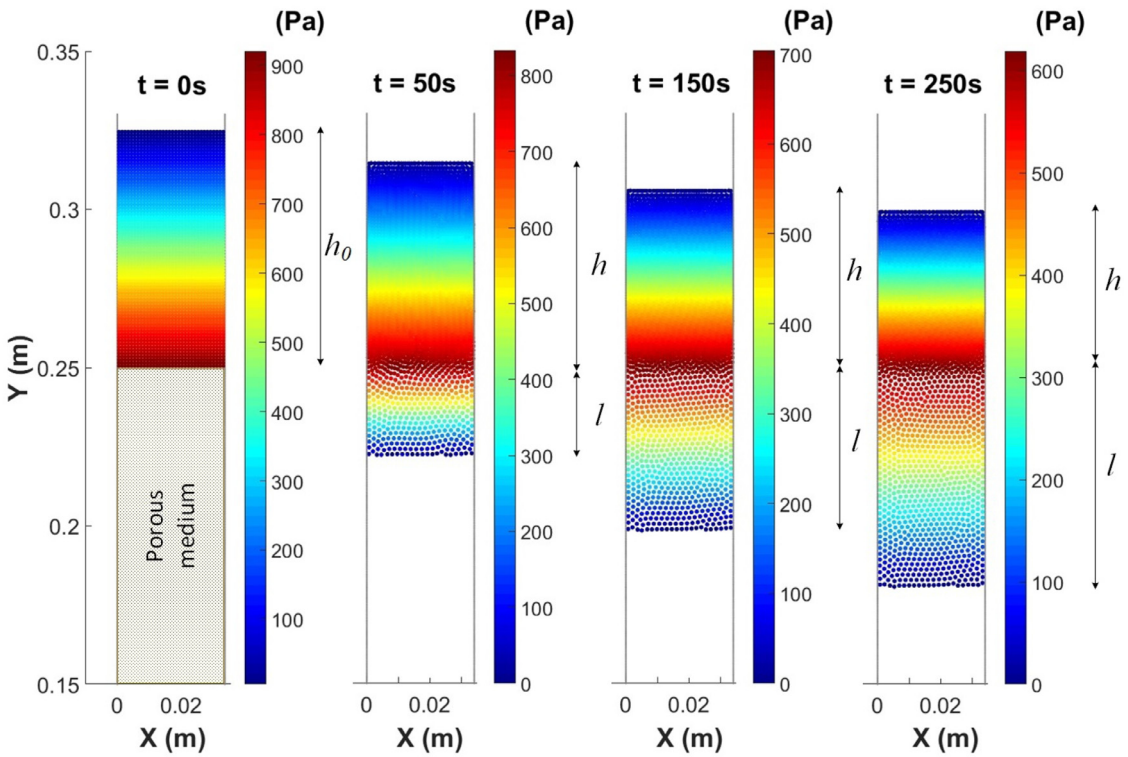

Fig. 3. Simulated pressure distribution in a case with a column of glycerine percolating through a porous medium 0.25 m deep. The Heun algorithm was used in the simulation.

3.1. Percolation of a fluid in a porous medium

The experiment of fluid percolation in a porous medium described in Acton et al. (2001) was simulated using both time integration algorithms. The experiment was conducted in a Perspex tube of internal diameter 0.034 m. The tube was filled to a depth of 0.25 m with spherical glass beads with a nominal diameter of $D = 0.002$ m. The porosity of the medium was measured as $\epsilon = 0.37 \pm 0.02$, and the permeability was found to be $\kappa = (3.13 \pm 0.2) \times 10^{-9}$ m^2. A volume of glycerine, $V = 6.78 \times 10^{-5}$ m^3, was poured onto the top of the medium as rapidly as possible. The depth of the poured glycerine was measured as $h_0 = 0.075$ m. The kinematic viscosity was measured to be 9.06×10^{-4} m^{2}s^{-1}.

In the simulations, the density of the fluid was assumed to be $\rho = 1260$ kg m^{-3}, such that the dynamic viscosity was set to $\mu = 1.14$ Pa · s. The initial spacing between fluid particles ($\Delta x = \Delta y$) was set to 0.001 m, with total number of fluid particles equal to 2550. The smoothing length, h, was $1.2\Delta x$, and the time step was 5×10^{-6} s. No-slip boundary conditions were imposed at the wall boundaries. The pore scale Reynolds number, $Re = uD/\nu$, was calculated as $Re = 3 \times 10^{-4}$. Since the pore scale Reynolds number was much lower than unity, the quadratic term of the drag force in Eq. (5) was neglected. The porosity was set to $\epsilon = 0.37$ and a linear gradual change was imposed at the transition layer, with a depth of $\delta_\epsilon = 0.0072$ m, as explained in Section 2.3. Not using this transition layer caused numerical instability that might be due to the sudden change in porosity. The permeability value was set to $\kappa = 3.13 \times 10^{-9}$ m^2.

Fig. 3 shows the simulated pressure values. The change in the porosity of the media (from $\epsilon = 1$ to $\epsilon = 0.37$) is evident from the particles moving apart at the surface of the porous medium ($Y = 0.25$ m), and this appears to be correctly handled. Fig. 4 shows pressure values at two elevations, ±0.02 m from the interface. These values were calculated as the average of the pressure values of the particles within a distance equal to a smoothing length above and below the measurement level. The theoretical pressure values were determined using the analytical equations, derived assuming a hydrostatic pressure, and measured fluid depths (Acton et al., 2001). As shown in Fig. 4, the model was able to reproduce these results using both time integration schemes; the comparable results of the two models might be due to the small time step.

Fig. 5a shows the drainage of the fluid through the porous medium, $(h_0 - h)$ where h is the residual fluid level above the porous medium, and Fig. 5b shows porosity times the percolated depth of the fluid within the porous medium, ϵl, as a function of time. Again both numerical algorithms were able to reproduce the observed data (Acton et al., 2001), with the Heun integration scheme leading to results slightly closer to the experiment. As shown in Fig. 5, the change of volume of glycerine in the free flow domain is equal to the change of volume occupied by glycerine in the porous medium (i.e., $h_0 - h = \epsilon l$). This appeared to be an issue in other studies that modelled a similar flow with SPH (Akbari, 2014; Aly and Asai, 2015). The error in volume conservation might be due to the approach used to model the interface between domains with different porosities; this requires further study. Furthermore, the SPH schemes in other studies are different. For example, Akbari (2014) changed the density of particles instead of their volumes when moving between media with different porosities. This might be problematic as density also appears in the pressure gradient term in addition to the particles volumes.

The CPU time for the Heun integration method was approximately twice that of the Euler integration method.

3.2. Gravity current over a porous medium

The experiment of Acton et al. (2001), who examined flow of a viscous gravity current over a dry porous medium, was simulated. In the experiment, a tank was used as sketched in Fig. 6. The porous medium was composed of dried spherical glass beads with

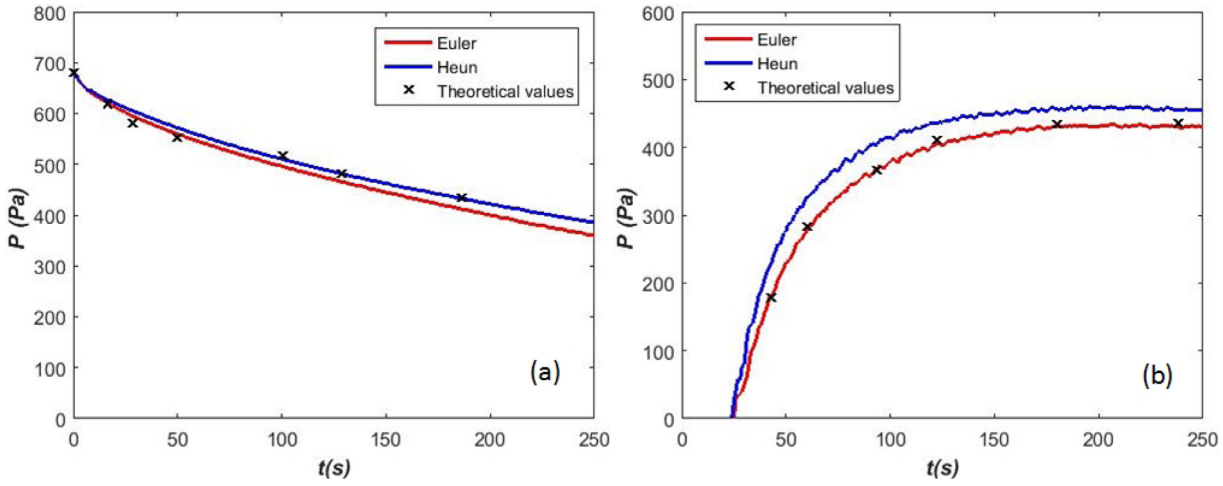

Fig. 4. Time evolution of pressure (a) 0.02 m above and (b) 0.02 m below the porous medium in the case of glycerine percolating into a porous medium.

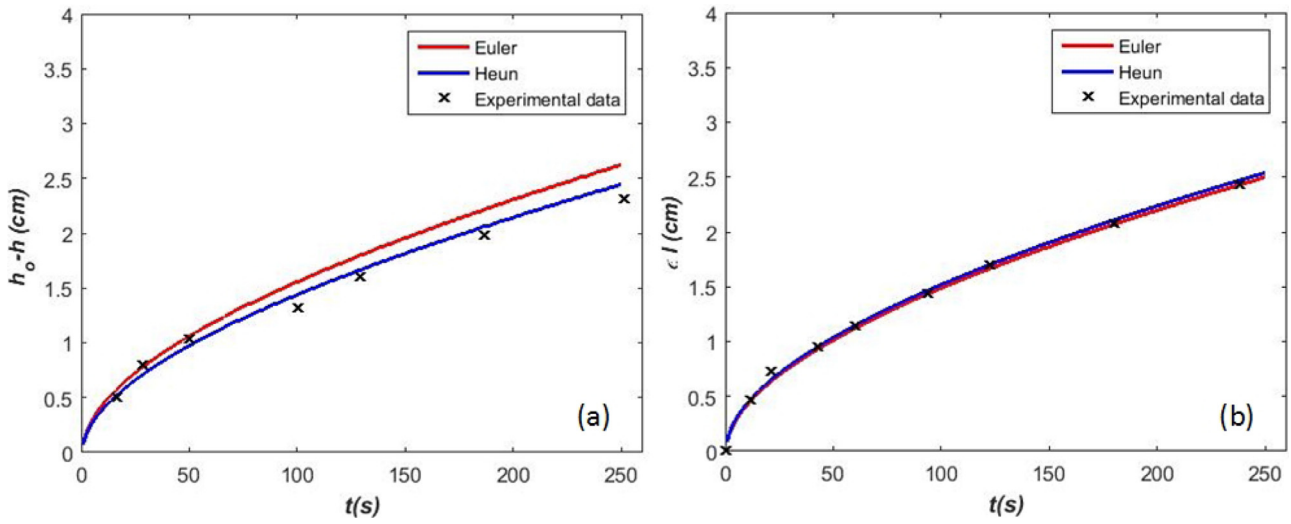

Fig. 5. (a) Time evolution of drainage of glycerine over the porous medium and (b) porosity times percolated depth of glycerine within the porous medium in the test case in Fig. 3.

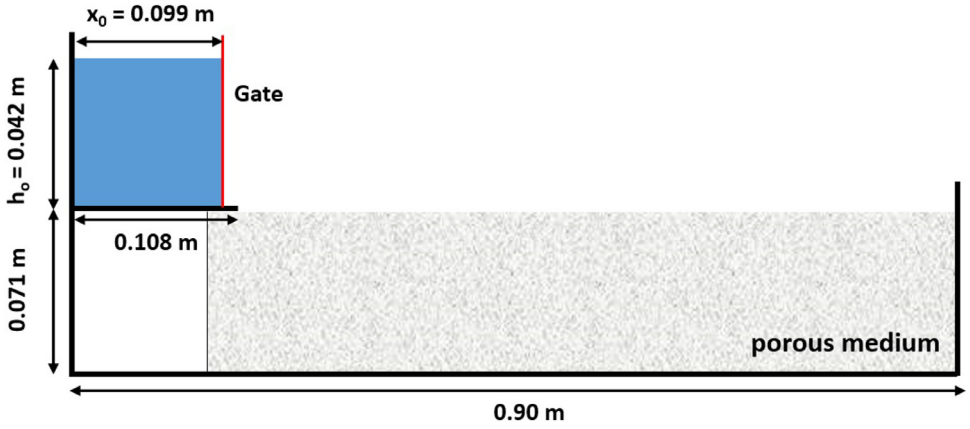

Fig. 6. Schematic view of the flume used in the experiment by Acton et al. (2001) (Section 3.2).

a nominal diameter of $D = 0.002$ m. The fluid behind the gate was glycerine with kinematic viscosity of $\nu = 7.2 \times 10^{-4}$ m^2 s^{-1}. The gate was raised at $t = 0$ s to allow a volume of glycerine to flow over the porous medium. After one second the gate was rapidly closed. The porosity and averaged permeability were found to be $\epsilon = 0.37 \pm 0.02$, and $\kappa = 3.1 \times 10^{-9}$ m^2, respectively. The volume per unit width of glycerine released after the closure of the gate was measured to be $q_{er} = 3.1 \times 10^{-3}$ m^2. The initial volume per unit width, depth, and length of the fluid behind the gate were not specified in Acton et al. (2001); therefore, they were assumed using a trial and error approach to obtain a released volume close to that in the experiment.

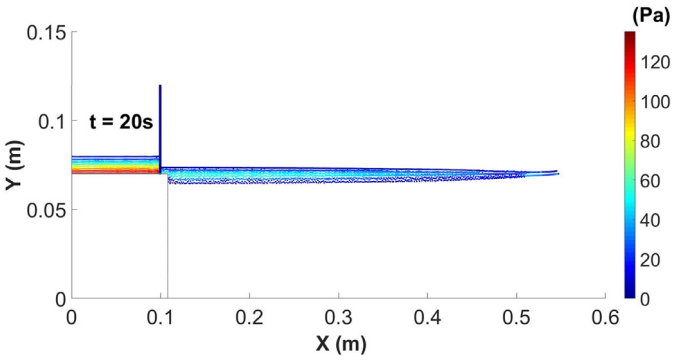

Fig. 7. Simulated pressure distribution for the propagation of a gravity wave over and within a porous medium (Section 3.2). The figure's scale is 2:1 for better visualisation of the vertical scale.

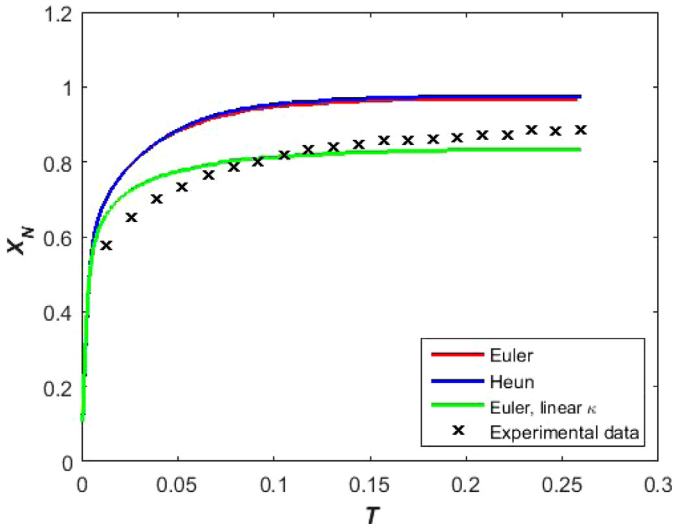

Fig. 8. Non-dimensional length of the current, X_N, as a function of non-dimensional time, T. The variables are $X_N = L/(q^4/3\kappa)^{1/6}$ and $T = t/(3\nu^6 q^2/g^6\kappa^5)^{1/6}$.

In the simulation, the initial volume per unit width, the initial depth and length of the fluid behind the gate were set to $q_0 = 4.16 \times 10^{-3}$ m^2, $h_0 = 0.042$ m, and $x_0 = 0.099$ m respectively. The initial spacing between fluid particles ($\Delta x = \Delta y$) was set to 0.001 m, with total number of fluid particles equal to 4561. The smoothing length, h, was 1.2 Δx, and the time step was 5×10^{-6} s. No-slip boundary conditions were imposed at solid boundaries. The dynamic viscosity was set to $\mu = 0.91$ Pa · s, assuming $\rho = 1260$ kg m^{-3}. The gate was simulated using virtual particles (Crespo et al., 2008) that exerted a repulsive force on the fluid particles (Eq. 32). The gate was initially open and it was closed a second after the release of the fluid. The closing speed of the gate was set to 0.5 m s^{-1}. The modelled volume of glycerine released was calculated as $q = 3.17 \times 10^{-3}$ m^2 by comparing the depth of the fluid behind the gate before and after gate closure. The quadratic drag in Eq. (5) was neglected due to the slow flow within the porous medium. The porosity was set to $\epsilon = 0.37$. It was observed that imposing a linear change of porosity at the transition layer caused unrealistic behaviour of the current near the porous medium. This seems to be a problem when the dominant direction of a flow is in a direction perpendicular to the direction porosity gradient. The current front tended to jump over half of the transition layer above the interface (i.e., $\delta_\epsilon/2$ in Fig. 2). To avoid this problem, the transition layer was modified such that the porosity changed linearly starting from the surface of the porous medium, for a depth of $\delta_\epsilon/2$. It should be added that using no transition layer at all caused numerical instability.

Fig. 7 shows the pressure distribution and qualitative form of the gravity current after twenty seconds. The change in the porosity of the media is again evident from the particles moving apart in the porous medium. Pressure distribution data are not available from the experiments. Qualitatively the model appears to give reasonable pressure distributions with maximum pressure at the interface decreasing to zero at the two fluid surfaces above and within the porous medium.

The length of the gravity current from the gate, L, is non-dimensionalised as $X_N = L/(q^4/3\kappa)^{1/6}$, and the time, t, is non-dimensionalised as $T = t/(3\nu^6 q^2/g^6\kappa^5)^{1/6}$ (Acton et al., 2001). Fig. 8 shows the non-dimensional data for the propagation of the gravity current length, X_N, as a function of non-dimensional time, T. As shown in Fig. 8, the two integration methods led to comparatively similar results. This might be due to the small time step. Both schemes generated a wave initially faster than the observed one. Differences between the model and experiments might be due to the lack of information about the initial conditions of the experiments. Additionally, the width of the experimental flume (0.15 m) might have slowed the wave, especially considering the large viscosity of glycerine, which might be better studied using a three dimensional model.

Another source of the error might be the uncertainty in the value of the permeability at the interface. The effect of change of permeability in the transition layer was tested using the Carman–Kozeny equation (Phillips, 1991), which relates permeability to porosity. Accordingly, the permeability in the transition layer was calculated using a linearly decreasing porosity. The position of the transition layer ($\delta_\epsilon/2$) was kept completely within the porous medium. As shown in Fig. 8 (the curve represented as Euler, linear κ), the results are sensitive to the permeability pattern in the transition layer; therefore, care is required in handling the distribution of the permeability in this zone.

Table 1
Characteristic of the experiments of Adduce et al. (2011) and values of the parameters (Section 3.3).

Run	x_0 (m)	ρ_d (kg m^{-3})	μ_d (Pa · s)	D_t (m^2 s^{-1})	Re_m
1	0.30	1090	1.27×10^{-3}	10^{-5}	38,724
2	0.30	1064	1.14×10^{-3}	10^{-5}	30,432
3	0.30	1037	1.07×10^{-3}	10^{-6}	24,137

3.3. Boussinesq lock-exchange over an impermeable bed

Three different Boussinesq lock-exchange gravity currents of two fluids over an impermeable bed, presented in Adduce et al. (2011), were simulated. In the experiments, a 3 m long tank, 0.30 m deep, and 0.2 m wide was used. The tank was divided in two parts using a gate, located a distance x_0 from the left wall of the tank. The right and left parts of the gate were filled with fresh water, $\rho_l = 1000$ kg m^{-3}, and salt water, ρ_d, respectively, to a depth of $h_0 = 0.30$ m. The density and initial length of the locks are shown in Table 1.

In the simulation, the EISPH scheme was solved with the Euler algorithm due to its comparable results with the Heun algorithm in the first two case studies. Two different initial spacing between fluid particles ($\Delta x = \Delta y$), 0.005 and 0.0025 with total number of fluid particles equal to 36,000 and 144,000, respectively, were used to check the sensitivity to the spatial resolution. The smoothing length, h, was $1.2\Delta x$, and the time step was 5×10^{-5} s. It was observed that the no-slip boundary conditions led to loss of accuracy in the velocity of the currents; this is in agreement with Marrone et al. (2013), Grenier et al. (2013) that question the accuracy of the

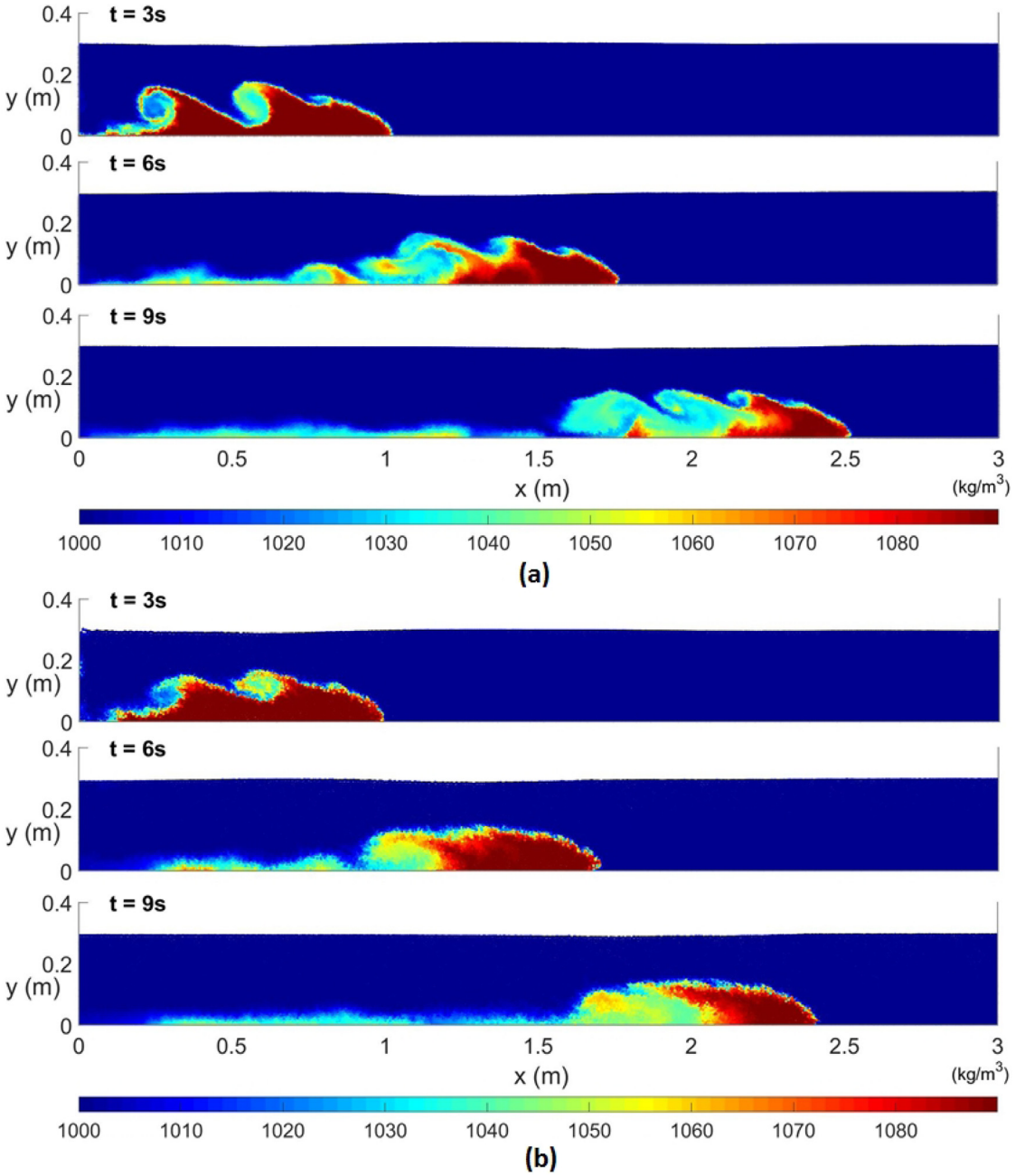

Fig. 9. Density evolution of the lock-exchange gravity current over an impermeable bed at different times for Run 1 (Table 1), with (a) $\Delta x = \Delta y = 0.0025$ m and (b) $\Delta x = \Delta y = 0.005$ m.

conventional implementation of the no-slip boundary conditions for flows with Reynolds numbers higher than 2400. Therefore, the modified no-slip boundary condition was used. The dynamic viscosity of fresh water was set to $\mu_l = 10^{-3}$ Pa · s, and the dynamic viscosity of the salt water, μ_d, were assumed as in Table 1 (Isdale et al., 1972). The coefficient of molecular diffusivity was assumed to be $D_m = 2 \times 10^{-9}$ m^2 s^{-1} (Lide, 2004). The turbulent eddy diffusivity was also accounted for, due to the high mean Reynolds number values for the experiments, and values within an approximated range provided in Jackson and Rehmann (2003) were used as shown in Table 1.

When the gate was removed, the salt water propagated over the tank's bed displacing the fresh water. Fig. 9 shows the density evolution of the current for Run 1, with $\Delta x = \Delta y = 0.0025$ m. As the heavy current propagates, mixing occurs at the interface between the two fluids. The qualitative form of the current is in agreement with the observations of Adduce et al. (2011), Rottman and Simpson (1983), as the fresh water current displaced the heavy current and it reached the left wall (Rottman and Simpson, 1983). In addition, Kelvin–Helmholtz vortices were reproduced at the interface between two fluids at the initial stage of the simulation (Pahar and Dhar, 2016a). The Kelvin–Helmholtz vortices were better captured using the finer resolution (Fig. 9).

Fig. 10(a) shows the position of the gravity current front from the left wall as a function of time for Run 1, with $\Delta x = \Delta y = 0.0025$ m. As shown in Fig. 10(a), the results reasonably agree with the ISPH model developed by Pahar and Dhar (2016a). It is also observed that the velocity of the simulated current (slope of the graph) is in agreement with that of the experimental current. The slight non-linearity in the initial trend of the observed data might

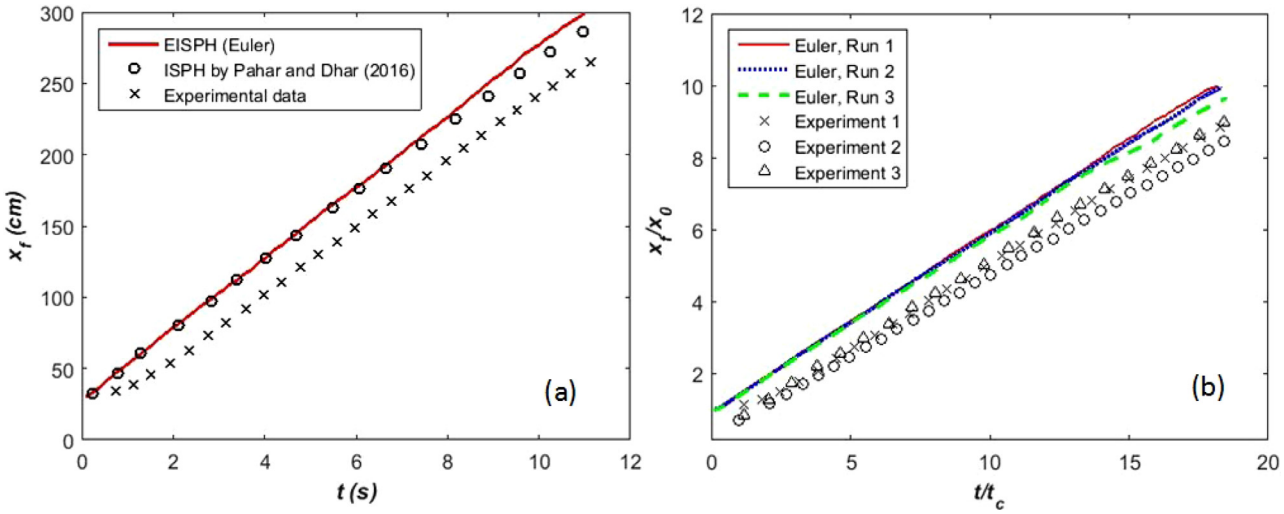

Fig. 10. (a) Comparison of the front positions, x_f, as functions of time, t, for Run 1 (Table 1), and (b) Non-dimensional front position as function of non-dimensional time for different experimental runs (Table 1); x_0 is the initial length of the heavy current and $t_c = x_0/\sqrt{g_0' h_0}$ with $g_0' = g(\rho_d - \rho_l)/\rho_d$.

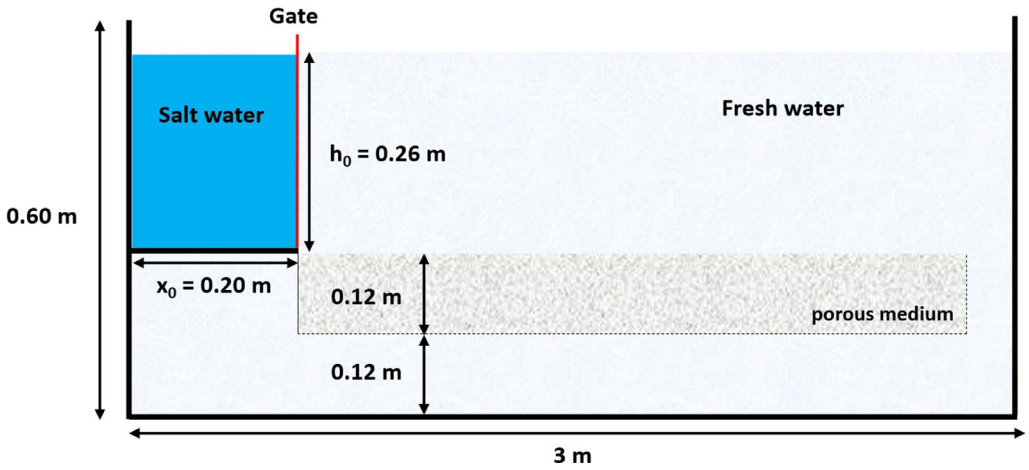

Fig. 11. Schematic view of the tank used in the experiment by Thomas et al. (2004) (Section 3.4).

be due to the effect of the gate removal. In addition, the differences between the simulated results and observed data might be also due to the gate effect. The difference between the leading position in the EISPH model and the ISPH model (Pahar and Dhar, 2016a) might be due to the calculation of turbulent stresses in Pahar and Dhar (2016a), which caused extra resistance against the current propagation. The position of the gravity current as a function of time for this simulation was observed to be dependent on the chosen spatial resolutions, showing around 4% difference between the simulations with $\Delta x = \Delta y = 0.005$ m and $\Delta x = \Delta y = 0.0025$ m.

Fig. 10(b) shows the non-dimensional data for the front position as a function of non-dimensional time for all the experiments. The position of the gravity currents from the left wall is non-dimensionalised as x_f/x_0, and the time, t, is non-dimensionalised as t/t_c, where $t_c = x_0/\sqrt{g_0' h_0}$. $g_0' = g(\rho_d - \rho_l)/\rho_d$ (Adduce et al., 2011). The model was able to reasonably reproduce the observed data. The gap between the simulated results and observed data might be due to the gate effect.

Using higher resolution in Run 3, where the density difference was smaller, led to better results such that the difference between the leading position of the heavy current in the two simulated resolutions was five percent.

3.4. Boussinesq lock-exchange in a porous medium

The last example combines the previous cases by considering a multi-fluid flow over and within a porous medium. An experiment described in Thomas et al. (2004) was used for this test case. In the experiment, a tank 3 m long, 0.6 m deep, and 0.2 m wide was used as shown in Fig. 11. An amount of dense salt water was released from behind a gate into the tank initially filled up with fresh water. The density of the salt and fresh water were $\rho_d = 1075$ kg m^{-3} and $\rho_l = 1000$ kg m^{-3}, respectively. The gravity current generated by the salt water moved over and through a saturated porous medium with thickness of $D_p = 0.12$ m composed of glass spheres with a nominal diameter of $D = 0.00286$ m. An empty space was left between the porous medium and the tank's right wall to let the drained fresh water move upward through the opening. The kinematic viscosity of the salt water was given as $\nu_d = 1.1 \times 10^{-6}$ m^{2}s^{-1}, and it was assumed to be $\nu_l = 10^{-6}$ m^{2}s^{-1} for fresh water. The porosity of the porous medium was $\epsilon = 0.375$, and the permeability was calculated as $\kappa = 6.14 \times 10^{-9}$ m^2 using the Carman–Kozeny equation (Phillips, 1991). The initial depth and width of the salt water behind the gate were $h_0 = 0.26$ m and $x_0 = 0.2$ m, respectively.

In the simulation, the section underneath the salt water was not simulated, since the left wall of the container holding the

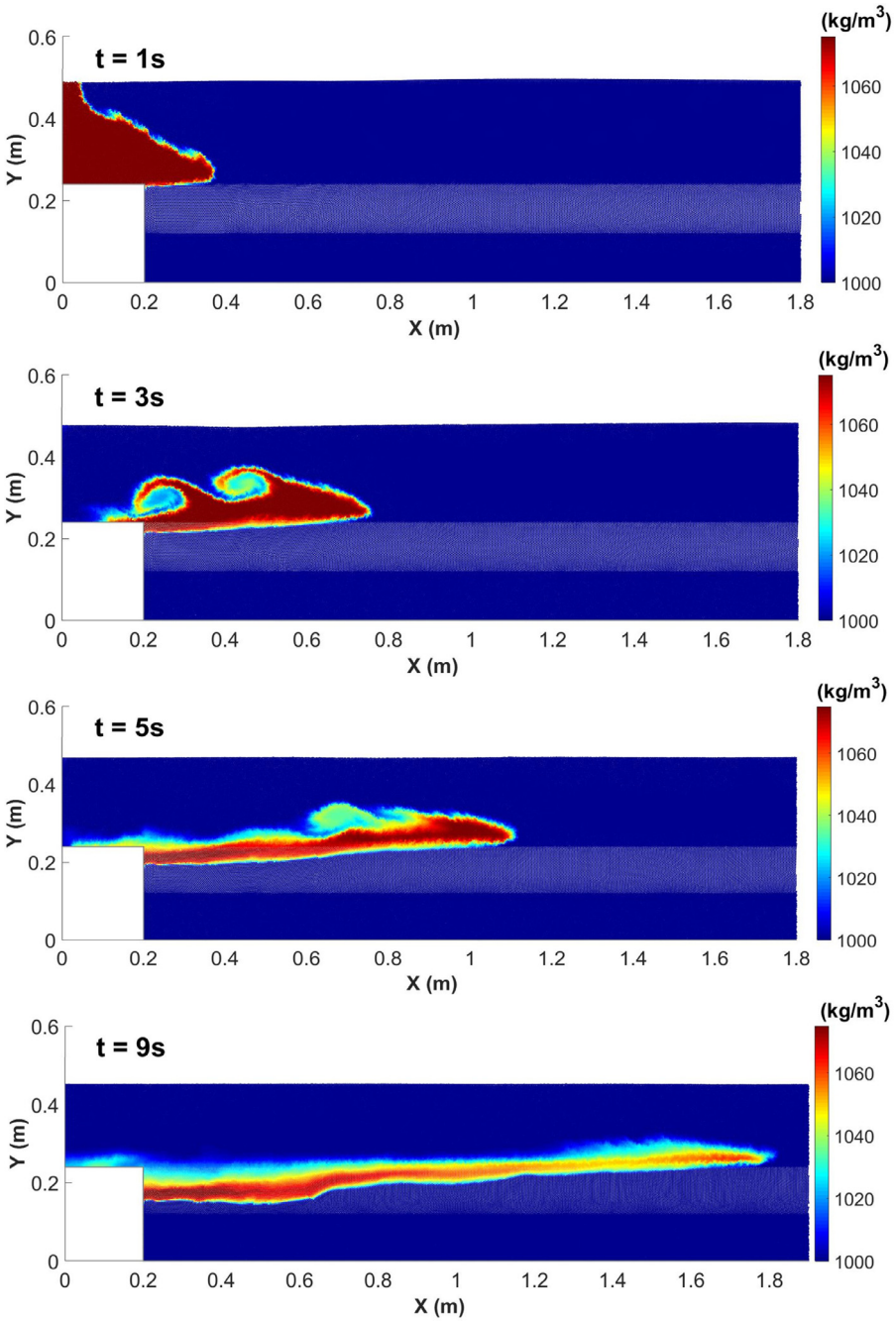

Fig. 12. Density evolution and the current propagation over and within the porous medium (Section 3.4), with $c_F = 2.67$ (Brinkman, 1949).

porous medium was impermeable (Fig. 11) and there was no salt water penetrating from the porous medium to underneath the salt water tank. The Euler integration algorithm was used. The initial spacing between fluid particles ($\Delta x = \Delta y$) was set to 0.0025 m in the fluid domain, and $0.0025/\sqrt{\epsilon}$ m in the porous medium, such that all the particles had the same mass. Consequently, 199,710 fluid particles were used. The smoothing length, h, was set to $1.2\Delta x$, and the time step was 5×10^{-5} s. The modified no-slip boundary conditions were imposed at solid boundaries. The dynamic viscosities for the salt and fresh water were set to $\mu_d = 1.18 \times 10^{-3}$ Pa · s and $\mu_l = 10^{-3}$ Pa · s, respectively. The pore scale Reynolds number was $Re \approx 12$; therefore, in addition to the linear term the quadratic drag term in Eq. (5) was also considered to account for the inertial drag. The porosity and the permeability were set to $\epsilon = 0.375$ and $\kappa = 6.14 \times 10^{-9}$ m^2, respectively. To investigate the sensitivity of the results to the Forchheimer coefficient, three values, $c_F = 2.67$ (Brinkman, 1949), $c_F = 1.2$ (Joseph et al., 1982), and $c_F = 0.2$ (Irmay, 1958), were used. The coefficient of molecular diffusivity was assumed to be $D_m = 2 \times 10^{-9}$ m^2 s^{-1} (Lide, 2004). The Reynolds number associated with the current over the porous medium was $Re = uh_c/\nu = 15,000$, h_c being the current head's height; therefore, a turbulent eddy diffusivity was also considered and a value within an approximated range from Jackson and Rehmann (2003) was used ($D_t = 10^{-5}$ m^2 s^{-1}). The flow within the porous medium was laminar; therefore, the turbulent eddy diffusivity was set to zero for particles within the porous medium. Using a transition layer for porosity and permeability led to unrealistic results so that the penetration of the current into the porous medium was significantly slow; this necessitates further study in simulating the interface under saturated con-

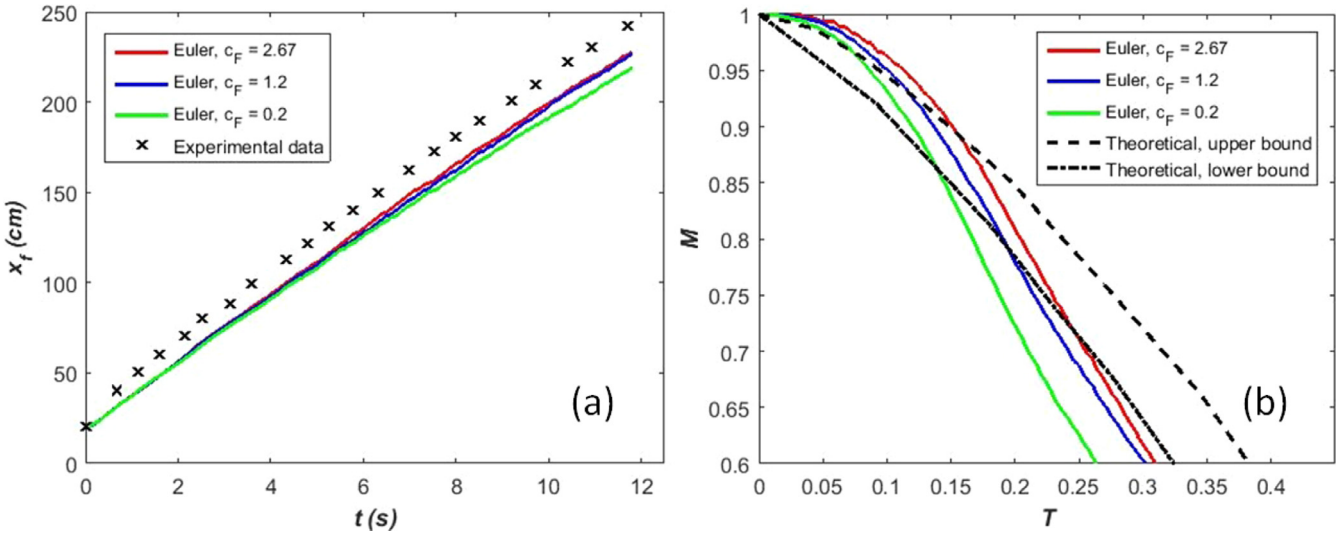

Fig. 13. (a) Evolution of the front position, and (b) non-dimensional remaining mass of the current over the porous medium. The variable x_f is the current position from the left wall, $T = t/\tau_d$, with $\tau_d = \nu_d D_p/\kappa g'_o$, and $M = m/m_0$.

ditions. Therefore, a sharp change of porosity and permeability at the external surfaces of the porous layer was considered in this case study.

Fig. 12 shows the density evolution and current propagation over and within the porous medium. The qualitative form of the current is comparable to the experiments with the salt water current front being deeper than the current following behind the front. Similar to the experiment, mixing occurred at the interface between the two fluids. The salt water percolated through the porous layer reaching larger depths near the gate than at the front. Fig. 13(a) shows the front position from the left wall, x_f, as a function of time, t. The slight difference between the simulated and experimental results might be due to the effects of removal of the gate. It is observed that using smaller Forchheimer coefficients caused a lower front speed. This might be due to the higher mass loss from above the porous medium (Fig. 13(b)) that decreased the driving force of the current. Fig. 13(b) shows the non-dimensional remaining mass of the current above the porous medium, $M = m/m_0$, as a function of non-dimensional time, $T = t/\tau_d$, where $\tau_d = \nu_d D_p/\kappa g'_o$ (Thomas et al., 2004). The remaining mass of the current over the porous medium was calculated as the ratio between the number of the salt water particles remaining above the porous medium and the total number of salt water particles. The results associated with the mass loss were compared to the results of a theoretical model developed by Thomas et al. (2004), since all the experimental results collapsed between two theoretical curves. It is evident that using a smaller Forchheimer coefficient led to the higher mass loss due to lower quadratic drag.

One of the possible sources of the errors might be related to the simulation of the interface between domains with different porosities. An error might arise in the calculation of the summation of the kernel function and its derivative at the interface between two media, because the kernel's support domain at the interface sits between different media, and the numbers of particles inside the support domain that belong to different media are different. We are now working on improving the modeling approach near the interface.

It is also reminded here that there is a controversy in the value of κ and c_F in the case of porosity values close to $\epsilon = 1/3$ (Joseph et al., 1982); this has led to different values of κ and c_F obtained from a series of experiments (Brinkman, 1949; Irmay, 1958; Joseph et al., 1982). This might be a potential source of the discrepancy in Fig. 13(b) that requires further study. In addition, the uncertainty in choosing a proper value for other parameters such as coefficient of turbulent eddy diffusivity might be another source of error.

4. Conclusions

An EISPH scheme, solved using two different time integration algorithms, was employed to simulate multi-fluid flows in porous media with a spatially varying porosity. Four cases, including percolation of a single fluid in a porous medium, gravity current over a porous medium, Boussinesq lock-exchange over both an impermeable bed and a porous medium, were simulated.

The two time integration methods led to comparatively similar results in the test cases, likely due to the small time steps used.

For the first two cases, the comparison of the EISPH results of the flows in the porous media against the experimentally observed data, which has rarely been done in the literature, showed the reliability of the model applied to this application.

According to the third case, the simulated front position of the lock-exchange flow over the impermeable bed was reasonably in agreement with the experimental data. In addition, the qualitative form of the currents was reproduced.

In the fourth case, a multi-fluid flow over and within a porous medium was simulated using the EISPH model and tested successfully for the first time against experimental data, where the EISPH approach captured the qualitative behaviour of the inertial wave over and within the porous medium. The variation of the mass of the current above the porous medium was compared with the experimental data, with discrepancies that requires further studies. The results of the speed of the current agreed with the experiment reasonably. In addition, a sensitivity analysis was performed for a model parameter, i.e. Forchheimer coefficient, using the values available in literature. Although using different values for the parameters led to expected changes in the results, it showed the importance of selecting the parameters appropriately to simulate experimental results. This usually seems to be an issue in other SPH studies that employ *ad hoc* values for parameters.

In some cases with flow infiltrating a porous medium, the use of a transition layer for porosity appeared to be beneficial in cases with dry porous media and problematic in the case with saturated porous medium. The modelling of the flow near the surface of the medium thus requires further improvement.

In closing, it is highlighted and stressed how important it is to provide sufficient details in experimental work to allow the reproduction of laboratory experiments. Although many experiments were found in the literature, only few had enough details to be successfully used in this study.

Acknowledgements

The authors thank J. J. Monaghan, H. H. Bui, and Nomeritae for useful discussions.

Appendix A. Heun algorithm

In the Heun integration algorithm, velocity and position of the particles were solved in two stages at each time step. In the first stage, a value of velocity, $\vec{\tilde{u}}_i^{n+1}$, and position, $\vec{\tilde{x}}_i^{n+1}$ at the new time step were predicted using the first order Euler method as

$$\vec{\tilde{u}}_i^{n+1} = \vec{u}_i^n + \left(\frac{d\vec{u}}{dt}\right)^n_{i[x^n,\epsilon^n,u^n,p^n,\rho^n]} \Delta t, \tag{A.1}$$

$$\vec{\tilde{x}}_i^{n+1} = \vec{x}_i^n + \left(\frac{\vec{u}_i^n}{\epsilon_i^n}\right)\Delta t \;\Rightarrow \tilde{\epsilon}_i^{n+1} = f\left(\vec{\tilde{x}}_i^{n+1}\right). \tag{A.2}$$

The variables inside the bracket in Eq. (A.1) were used in the corresponding stage. In the second stage, the values of the variables were updated as

$$\vec{u}_i^{n+1} = \vec{u}_i^n + \frac{\left(\frac{d\vec{u}}{dt}\right)^n_{i[x^n,\epsilon^n,u^n,p^n,\rho^n]} + \left(\frac{d\vec{u}}{dt}\right)^{n+1}_{i[\vec{x}^{n+1},\tilde{\epsilon}^{n+1},\tilde{u}^{n+1},p^{n+1},\rho^n]}}{2}\Delta t, \tag{A.3}$$

$$\vec{x}_i^{n+1} = \vec{x}_i^n + \frac{\left(\frac{\vec{u}_i^n}{\epsilon_i^n}\right) + \left(\frac{\vec{u}_i^{n+1}}{\tilde{\epsilon}_i^{n+1}}\right)}{2} \Rightarrow \epsilon_i^{n+1} = f\left(\vec{x}_i^{n+1}\right), \tag{A.4}$$

and finally the concentration and density of the particles were updated as

$$C_i^{n+1} = C_i^n + \left(\mathcal{D}_e \nabla^2 C\right)_{i[x^{n+1},\epsilon^{n+1},C^n]} \Delta t, \tag{A.5}$$

$$\rho_i^{n+1} = C_i^{n+1}(\rho_d - \rho_l) + 0.5(\rho_d + \rho_l) \;\Rightarrow m_i^{n+1} = \rho_i^{n+1} V_{pi}. \tag{A.6}$$

Approximate prediction–correction method (See 2.2.2) was used to calculate du/dt and impose incompressibility at each stage.

Because the momentum and pressure steps must be calculated twice; therefore, the Heun algorithm is approximately twice as expensive as the Euler.

References

Acton, J.M., Huppert, H.E., Worster, M.G., 2001. Two-dimensional viscous gravity currents flowing over a deep porous medium. J. Fluid Mech. 440, 359–380.
Adduce, C., Sciortino, G., Proietti, S., 2011. Gravity currents produced by lock exchanges: experiments and simulations with a two-layer shallow-water model with entrainment. J. Hydraul. Eng. 138 (2), 111–121.
Akbari, H., 2014. Modified moving particle method for modeling wave interaction with multi layered porous structures. Coastal Eng. 89, 1–19.
Aly, A.M., Asai, M., 2015. Three-dimensional incompressible smoothed particle hydrodynamics for simulating fluid flows through porous structures. Transp. Porous Media 110 (3), 483–502.
Birman, V., Martin, J., Meiburg, E., 2005. The non-boussinesq lock-exchange problem. Part 2. high-resolution simulations. J. Fluid Mech. 537, 125–144.
Brinkman, H., 1949. A calculation of the viscous force exerted by a flowing fluid on a dense swarm of particles. Flow, Turbul. Combust. 1 (1), 27.
Bui, H.H., Sako, K., Fukagawa, R., 2007. Numerical simulation of soil–water interaction using smoothed particle hydrodynamics (SPH) method. J. Terramech. 44 (5), 339–346.
Cantero, M.I., Lee, J., Balachandar, S., Garcia, M.H., 2007. On the front velocity of gravity currents. J. Fluid Mech. 586, 1–39.
Coutinho, B.G., Marcondes, F., de Lima, A.G.B., 2008. Numerical simulation of oil recovery through water flooding in petroleum reservoir using boundary-fitted coordinates. Int. J. Model. Simul. Petrol. Ind. 2 (1), 17–34.
Crespo, A., Gómez-Gesteira, M., Dalrymple, R.A., 2008. Modeling dam break behavior over a wet bed by a SPH technique. J. Waterw., Port, Coast., Ocean Eng. 134 (6), 313–320.
Cummins, S.J., Rudman, M., 1999. An SPH projection method. J. Comput. Phys. 152 (2), 584–607.
Duman, T., Shavit, U., 2010. A solution of the laminar flow for a gradual transition between porous and fluid domains. Water Resour. Res. 46 (W09517). http://dx.doi.org/10.1029/2009WR008393.
Fourtakas, G., Rogers, B., 2016. Modelling multi-phase liquid-sediment scour and resuspension induced by rapid flows using smoothed particle hydrodynamics (sph) accelerated with a graphics processing unit (gpu). Adv. Water Resour. 92, 186–199.
Ghasemi V, A., Firoozabadi, B., Mahdinia, M., 2013. 2D numerical simulation of density currents using the SPH projection method. Eur. J. Mech.-B/Fluids 38, 38–46.
Grenier, N., Le Touzé, D., Colagrossi, A., Antuono, M., Colicchio, G., 2013. Viscous bubbly flows simulation with an interface sph model. Ocean Eng. 69, 88–102.
Hosseini, S., Manzari, M., Hannani, S., 2007. A fully explicit three-step SPH algorithm for simulation of non-newtonian fluid flow. Int. J. Numer. Methods Heat Fluid Flow 17 (7), 715–735.
Huppert, H.E., 2006. Gravity currents: a personal perspective. J. Fluid Mech. 554, 299–322.
Huppert, H.E., Woods, A.W., 1995. Gravity-driven flows in porous layers. J. Fluid Mech. 292 (1), 55.
Irmay, S., 1958. On the theoretical derivation of darcy and forchheimer formulas. Eos, Trans. Am. Geophys. Union 39 (4), 702–707.
Isdale, J., Spence, C., Tudhope, J., 1972. Physical properties of sea water solutions: viscosity. Desalination 10 (4), 319–328.
Jackson, P.R., Rehmann, C.R., 2003. Laboratory measurements of differential diffusion in a diffusively stable, turbulent flow. J. Phys. Oceanogr. 33 (8), 1592–1603.
Joseph, D., Nield, D., Papanicolaou, G., 1982. Nonlinear equation governing flow in a saturated porous medium. Water Resour. Res. 18 (4), 1049–1052.
Kunz, P., Zarikos, I., Karadimitriou, N., Huber, M., Nieken, U., Hassanizadeh, S., 2016. Study of multi-phase flow in porous media: comparison of SPH simulations with micro-model experiments. Transp. Porous Media 114 (2), 581–600.
Leroy, A., Violeau, D., Ferrand, M., Joly, A., 2015. Buoyancy modelling with incompressible SPH for laminar and turbulent flows. Int. J. Numer. Methods Fluids 78 (8), 455–474.
Lide, D.R., 2004. CRC Handbook of Chemistry and Physics, 85. CRC press.
Lind, S., Stansby, P., Rogers, B., Lloyd, P., 2015. Numerical predictions of water–air wave slam using incompressible–compressible smoothed particle hydrodynamics. Appl. Ocean Res. 49, 57–71.
Liu, G.-R., Liu, M.B., 2003. Smoothed Particle Hydrodynamics: A Meshfree Particle Method. World Scientific.
Lowe, R.J., Rottman, J.W., Linden, P., 2005. The non-boussinesq lock-exchange problem. Part 1. theory and experiments. J. Fluid Mech. 537, 101–124.
Marrone, S., Antuono, M., Colagrossi, A., Colicchio, G., Le Touzé, D., Graziani, G., 2011. δ-SPH Model for simulating violent impact flows. Comput. Methods Appl. Mech. Eng. 200 (13), 1526–1542.
Marrone, S., Colagrossi, A., Antuono, M., Colicchio, G., Graziani, G., 2013. An accurate sph modeling of viscous flows around bodies at low and moderate Reynolds numbers. J. Comput. Phys. 245, 456–475.
Mokos, A., Rogers, B.D., Stansby, P.K., Domínguez, J.M., 2015. Multi-phase sph modelling of violent hydrodynamics on gpus. Comput. Phys. Commun. 196, 304–316.
Monaghan, J., Rafiee, A., 2013. A simple SPH algorithm for multi-fluid flow with high density ratios. Int. J. Numer. Methods Fluids 71 (5), 537–561.
Monaghan, J.J., 1992. Smoothed particle hydrodynamics. Annu. Rev. Astron. Astrophys. 30, 543–574.
Monaghan, J.J., 1994. Simulating free surface flows with SPH. J. Comput. Phys. 110 (2), 399–406.
Monaghan, J.J., 2005. Smoothed particle hydrodynamics. Rep. Prog. Phys. 68 (8), 1703.
Monaghan, J.J., Lattanzio, J.C., 1985. A refined particle method for astrophysical problems. Astron. Astrophys. 149, 135–143.
Morris, J.P., 1996. Analysis of Smoothed Particle Hydrodynamics with Applications. Monash University Australia.
Morris, J.P., Fox, P.J., Zhu, Y., 1997. Modeling low Reynolds number incompressible flows using SPH. J. Comput. Phys. 136 (1), 214–226.
Nield, D.A., 2000. Modelling fluid flow and heat transfer in a saturated porous medium. Adv. Decis. Sci. 4 (2), 165–173.
Nomeritae, Daly, E., Grimaldi, S., Bui, H.H., 2016. Explicit incompressible SPH algorithm for free-surface flow modelling: a comparison with weakly compressible schemes. Adv. Water Resour. 97, 156–167.
Pahar, G., Dhar, A., 2016. Mixed miscible–immiscible fluid flow modelling with incompressible SPH framework. Eng. Anal. Bound Elem. 73, 50–60.
Pahar, G., Dhar, A., 2016. Modeling free-surface flow in porous media with modified incompressible SPH. Eng. Anal. Bound Element 68, 75–85.
Pahar, G., Dhar, A., 2016. A robust volume conservative divergence-free ISPH framework for free-surface flow problems. Adv. Water Resour. 96, 423–437.
Phillips, O.M., 1991. Flow and Reactions in Permeable Rocks. Cambridge University Press.

Price, D.J., Monaghan, J., 2004. Smoothed particle magnetohydrodynamics–ii. variational principles and variable smoothing-length terms. Mon. Not. R. Astron. Soc. 348 (1), 139–152.
Rafiee, A., Thiagarajan, K.P., 2009. An SPH projection method for simulating fluid-hypoelastic structure interaction. Comput. Methods Appl. Mech. Eng. 198 (33), 2785–2795.
Rottman, J.W., Simpson, J.E., 1983. Gravity currents produced by instantaneous releases of a heavy fluid in a rectangular channel. J. Fluid Mech. 135, 95–110.
Rotunno, R., Klemp, J., Bryan, G., Muraki, D., 2011. Models of non-boussinesq lock--exchange flow. J. Fluid Mech. 675, 1–26.
Shao, S., 2010. Incompressible SPH flow model for wave interactions with porous media. Coast. Eng. 57 (3), 304–316.
Shao, S., 2013. Smoothed particle simulation of gravity waves in a multifluid system. Proc. Inst. Civil Eng.: Eng. Comput. Mech. 166 (1), 32–39.
Shao, S., Lo, E.Y., 2003. Incompressible SPH method for simulating newtonian and non-newtonian flows with a free surface. Adv. Water Resour. 26 (7), 787–800.
Simpson, J.E., 1982. Gravity currents in the laboratory, atmosphere, and ocean. Annu. Rev. Fluid Mech. 14 (1), 213–234.
Simpson, J.E., 1997. Gravity Currents: In the Environment and the Laboratory. Cambridge University Press.
Simunek, J., Suarez, D.L., 1993. Modeling of carbon dioxide transport and production in soil: 1. model development. Water Resour. Res. 29 (2), 487–497.
Tartakovsky, A.M., Trask, N., Pan, K., Jones, B., Pan, W., Williams, J.R., 2016. Smoothed particle hydrodynamics and its applications for multiphase flow and reactive transport in porous media. Comput. Geosci. 20 (4), 807–834.
Thomas, L., Marino, B., Linden, P., 2004. Lock-release inertial gravity currents over a thick porous layer. J. Fluid Mech. 503, 299–319.
Ungarish, M., Huppert, H.E., 2002. On gravity currents propagating at the base of a stratified ambient. J. Fluid Mech. 458, 283–301.
Violeau, D., Rogers, B.D., 2016. Smoothed particle hydrodynamics (SPH) for free-surface flows: past, present and future. J. Hydraul. Res. 54 (1), 1–26.
Zhao, B., MacMinn, C.W., Szulczewski, M.L., Neufeld, J.A., Huppert, H.E., Juanes, R., 2013. Interface pinning of immiscible gravity-exchange flows in porous media. Phys. Rev. E 87 (2), 023015.
Zhu, Y., Fox, P.J., 2001. Smoothed particle hydrodynamics model for diffusion through porous media. Transp. Porous Media 43 (3), 441–471.

4.3 Additional results

Further investigations were carried out to improve the results of the case study of Boussinesq lock-exchange in a porous medium (section 3.4 of the paper). One of the possible sources of the error might be related to the insufficient number of particles inside the support of the kernel function in porous media due to the coarser resolution. Although using a quintic kernel with a larger support domain can be used to tackle this problem, this alone can not guarantee enough number of particles within a kernel. An alternative approach is to adjust the radius of the support of the kernel in accordance with the porosity of the domain (for a detailed description see section 3.2.2).

Therefore, the quintic spline kernel, used in the paper, was applied with a variable smoothing length. The initial spacing between fluid particles ($\Delta x = \Delta y$) was as in the paper, i.e. 0.0025 m in the fluid domain, and $0.0025/\sqrt{\epsilon}$ m in the porous medium. The smoothing length, h, was set to $1.2\Delta x$, with Δx varying in different media. Therefore, the smoothing length had an inverse ratio with the porosity; this led to a larger support domain of the kernel function in the porous medium.

Fig. 4.1 shows the non-dimensional remaining mass of the current above the porous medium, $M = m/m_0$, as a function of the non-dimensional time, $T = t/\tau_d$, where $\tau_d = \nu_d D_p/\kappa g'_o$ (*Thomas et al.*, 2004).

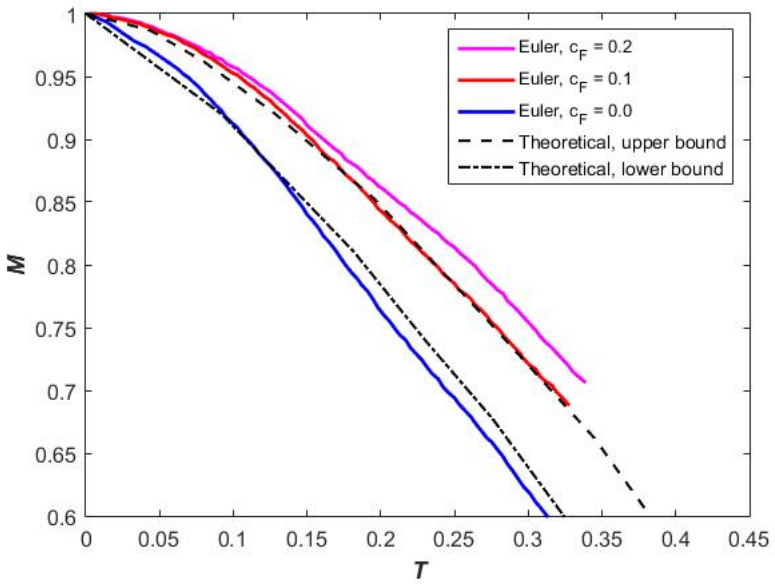

Figure 4.1: Non-dimensional remaining mass of the current over the porous medium, with smoothing length varying in different media

It is observed that there is an improvement in the rate of the loss of the mass. The rates of the mass loss in Fig. 4.1 are parallel to the theoretical bounds, in contrast to the rates in the paper where the rates are smaller than the theoretical ones at initial stages and larger at the final stages of the experiments.

It is observed that the value of the Forchheimer coefficient has a considerable effect on the results. According to *Joseph et al.* (1982) when spheres, consisting of a porous medium, are closely packed and porosity value is close to $\epsilon = 1/3$, the Forchheimer equation fails to reproduce close match with experiments. The results in this thesis appear to agree with their argument.

4.3.1 Comparing EISPH results with an analytical solution

In this section an analytical case study presented in *Peng et al.* (2017) and *Khayyer et al.* (2018) is simulated using EISPH to further validate the EISPH method. The case study presents a Darcy seepage flow through a porous layer, with a porosity equal to $\epsilon = 0.4$, as in Fig. 4.2. The fluid inside the U shape tube is water and it flows from left to right. The flow is driven by gravity due to the head difference, ΔH, between the left and right columns. ΔH is expected to gradually decrease until water levels in both sides are balanced. By applying the Darcy law, the evolution of ΔH can be calculated as

$$\Delta H = \frac{\Delta H_0}{\exp(2K_h t/L)} \tag{4.1}$$

where $\Delta H_o = 1.35$ m is the initial head difference between two sides, $L = 1.0$ m is the length of the porous medium and K_h is hydraulic conductivity of the porous medium.

In the simulation, similar to the cases in the published paper, the quintic spline kernel was used. The initial spacing between fluid particles ($\Delta x = \Delta y$) was set to 0.05 m ($\Delta x/\Delta H_0 = 27$) as in (*Peng et al.*, 2017; *Khayyer et al.*, 2018), and it was set to $0.05/\sqrt{\epsilon}$ m in the porous medium. The smoothing length, h, was set to $1.2\Delta x$, with Δx varying in different media. The time step was set to $\Delta t = 2.5 \times 10^{-4}$ s. The quadratic drag term of Eq. (3.4) is neglected as a linear Darcy seepage was assumed in Eq. (4.1) (*Peng et al.*, 2017; *Khayyer et al.*, 2018). The permeability is calculated as

$$\kappa = \frac{\mu K_h}{\rho g}. \tag{4.2}$$

The linear gradual change, as explained in section 3.4.4, was used to gradually change porosity from $\epsilon = 1$ in the free flow domain to $\epsilon = 0.4$ in the porous medium.

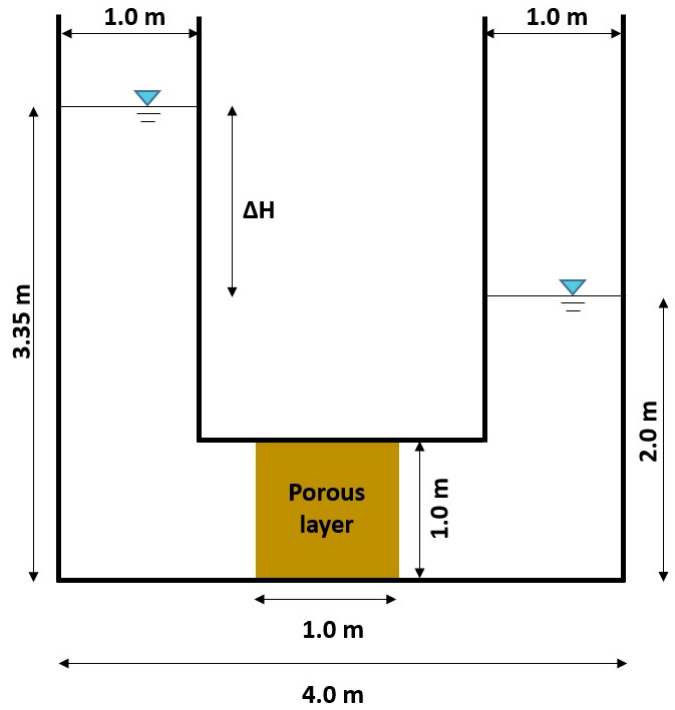

Figure 4.2: Schematic view of the case study in section 4.3.1 (*Peng et al.*, 2017; *Khayyer et al.*, 2018).

Fig. 4.3 shows the pressure distribution at different times for different hydraulic conductivity values. It is observed that the model was able to reproduce a smooth pressure distribution. Although the values for pressure is not mentioned in *Peng et al.* (2017) or *Khayyer et al.* (2018), the model appears to reproduce values close to hydrostatic pressure, which is expected due to low seepage velocity of the flow. Continuity of pressure at the interface between different media is also visible in all the cases.

Fig. 4.4 compares the time variation of ΔH calculated in EISPH with the analytical solution, WCSPH (*Peng et al.*, 2017) and the Enhanced ISPH results (*Khayyer et al.*, 2018). It is observed that EISPH closely reproduced the analytical solution.

The simulation for hydraulic conductivity of $K_h = 0.005$ was repeated for three different initial spacing between fluid particles. The simulation was tested for $\Delta x = \Delta y = 0.045, 0.055$, and 0.06 m. These particle spacing correspond to $\Delta x/\Delta H_0 = 30, 24.5$ and 22.5, respectively. Fig. 4.5 shows the time evolution of ΔH as a function of time for all the resolutions. It is observed that the results for all the particles spacing are in good agreement with the analytical solution.

Table. 4.1 shows the Root Mean Square Error (RMSE) for different particle spacing. It is observed that reducing particle spacing increased the accuracy of the results.

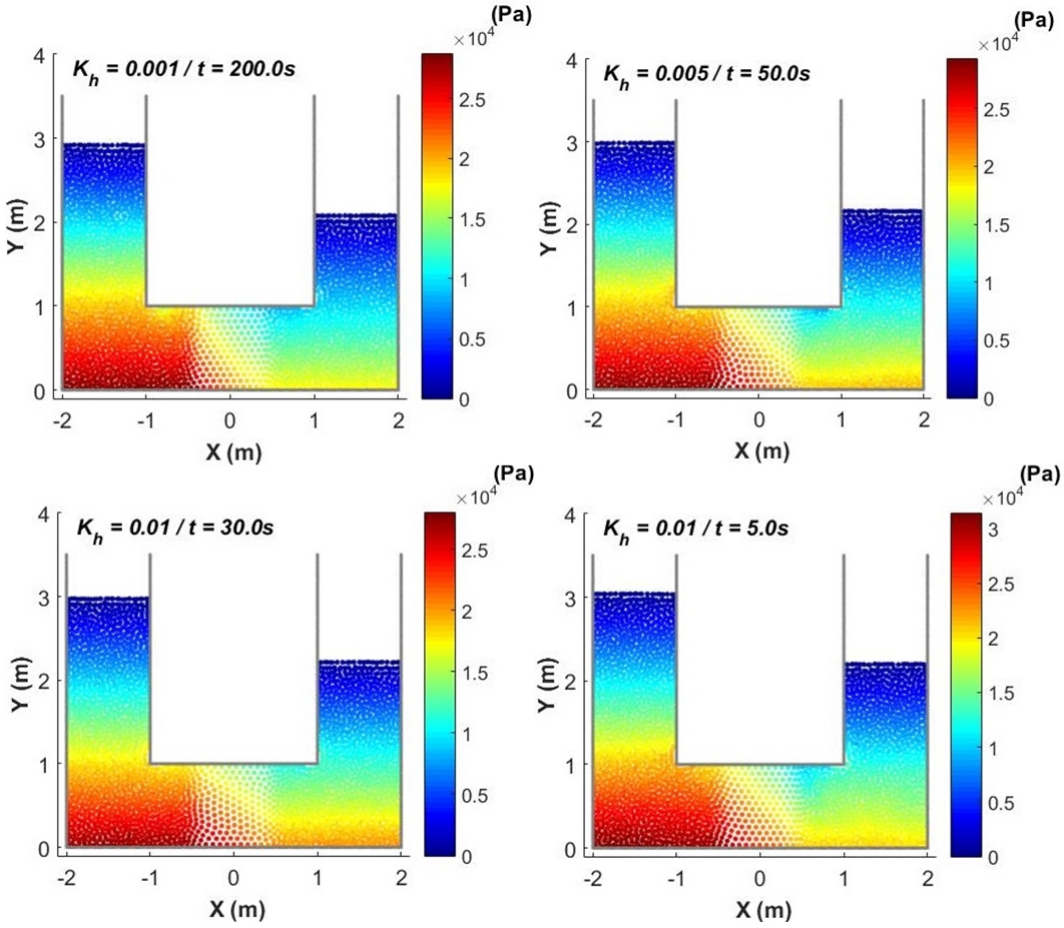

Figure 4.3: Pressure distribution for different hydraulic conductivity values, and at different times, section 4.3.1. (The snapshots are shown at different times for different hydraulic conductivities to present an equal head difference between the left and right tubes)

Table 4.1: Root Mean Square Error (RMSE) for the EISPH time evolution of the water level difference with different initial particle spacing.

$\Delta x = \Delta y$ (m)	0.045	0.05	0.055	0.06
RMSE (m)	0.0056	0.0076	0.0148	0.0341

4.3.2 Normal stress continuity

The continuity of stress at an interface between a porous medium and a free flow domain was investigated using the case in section 3.1 of the published paper in this chapter. The pressure distribution around the interface is illustrated at different times in Fig. 4.6. As observed in Fig. 4.6, the EISPH method was able to reproduce smooth pressure across

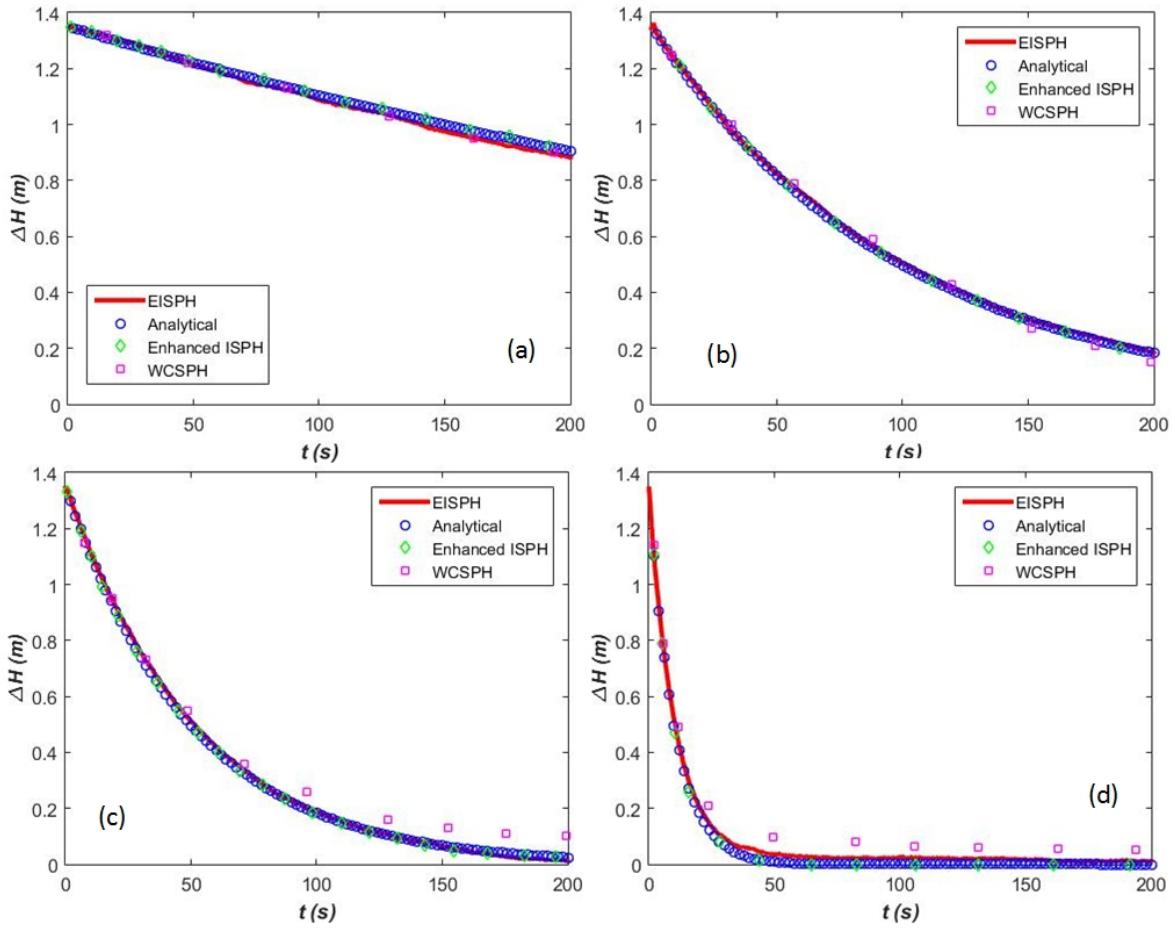

Figure 4.4: Comparison of the EISPH time evolution of the water level difference with the analytical solution in Eq. (4.1), Enhanced ISPH (*Khayyer et al.*, 2018) and WCSPH (*Peng et al.*, 2017), as a function of time for hydraulic conductivity of a) 0.001, b) 0.005, c) 0.01 and d) 0.05, section 4.3.1.

different media. The continuity of the normal stress (pressure) is qualitatively observed at the interface.

Fig. 4.7 shows a quantitative comparison of the averaged pressure value 1 mm above and below the interface. It is observed that these pressure values are generally equal to each other. The discrepancy at the start of the simulation is due to the passage of the free surface through the measurement level below the interface. When the free surface within the porous medium is close to the measurement point the pressure is not expected to be continuous, because of the way the pressure values in Fig. 4.7 were calculated. The pressure values were calculated as the average of the pressure values of the particles within a distance equal to the radius of the support domain of the kernel function above

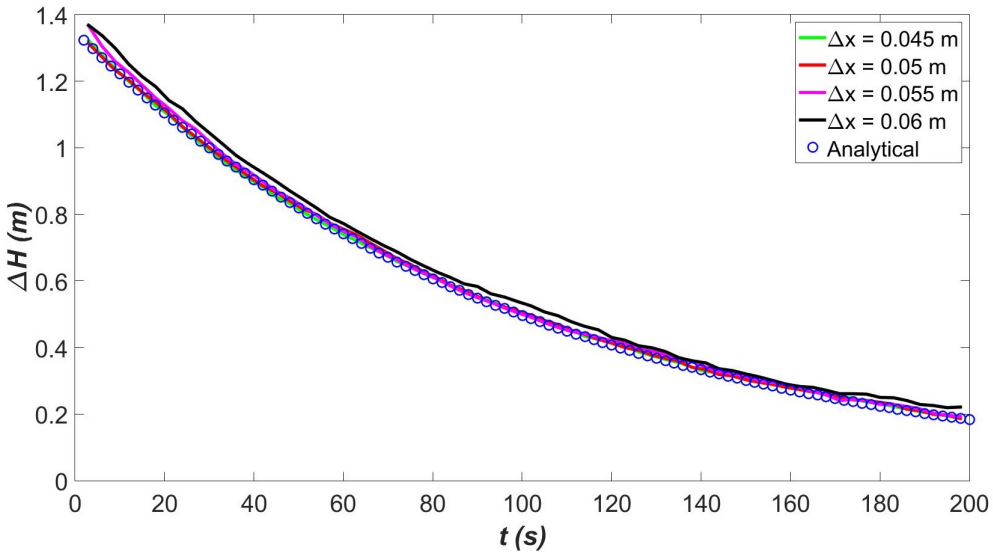

Figure 4.5: Comparison of the EISPH time evolution of the water level difference with the analytical solution in Eq. (4.1), as a function of time for different initial particle spacing, section 4.3.1.

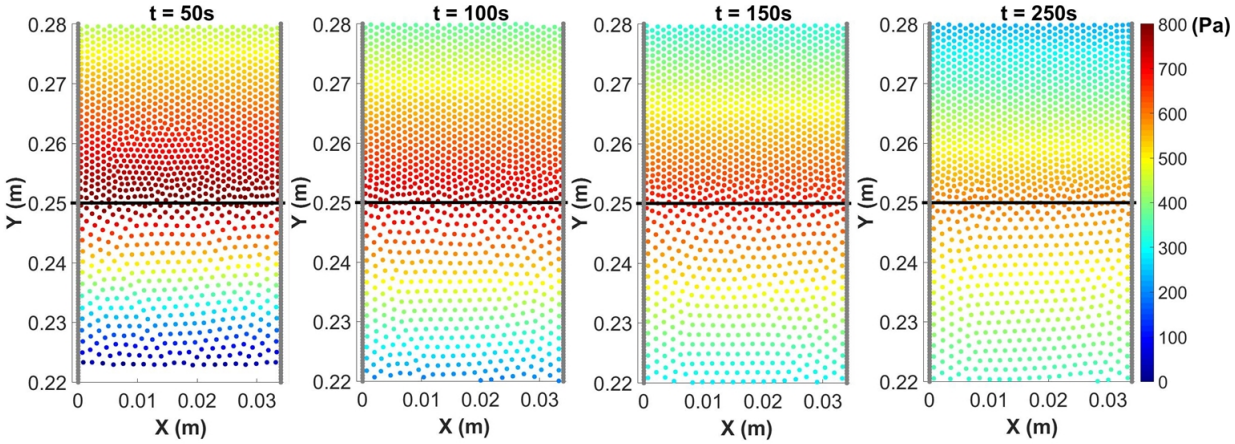

Figure 4.6: Pressure distribution around the interface between the free flow domain and the porous medium

and below the measurement level.

4.4 Conclusion

The two time integration methods led to comparatively similar results in the first two test cases, likely due to the small time steps used. Therefore, the Euler method was used

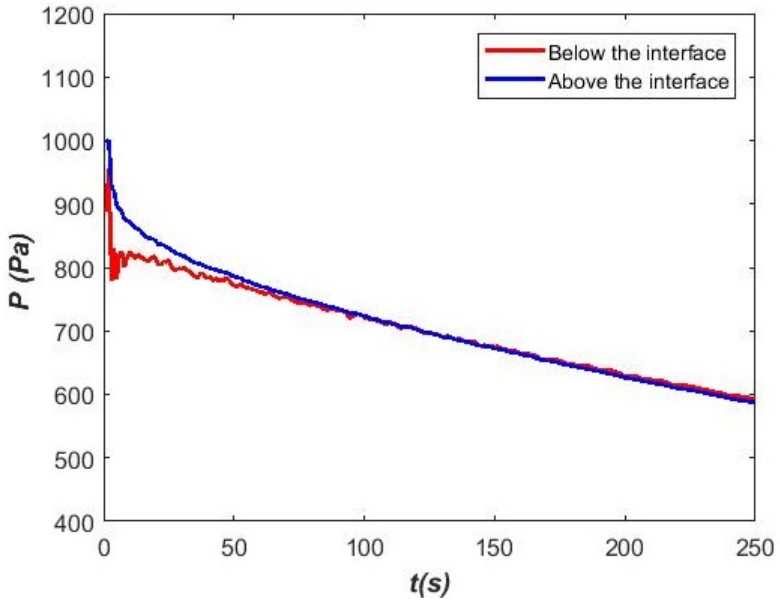

Figure 4.7: Time evolution of the pressure values 1 mm above and below the interface.

to simulate the subsequent simulations owing to its faster computational speed.

The EISPH results were compared to experimental observations and an analytical solution, which is often not done at a quantitative level in SPH investigations. The EISPH results associated with the first two experimental cases, showed the reliabilities of the model in simulating flow within and over porous media. The model reproduced a smooth pressure field in the both cases, with values close to the expected analytical pressures. According to the third case, the EISPH results of the multi-fluid lock-exchange flow over the impermeable bed were qualitatively and quantitatively comparable to the experimental data. In the fourth case, a multi-fluid flow over and within a porous medium was simulated and tested successfully for the first time against experimental data. The EISPH approach captured the qualitative behaviour of the current over and within the porous medium. The quantitative investigation showed a discrepancy in the results. Subsequent investigations showed that this could be further improved using a kernel with variable smoothing length, varying across different media with different porosities (see section 4.3). The use of the variable smoothing length considerably improved the infiltration rate of the current mass into the porous medium. In addition, a sensitivity analysis was conducted for the model parameters such as Forchheimer coefficient. The change of the parameters led to the expected changes in the results. However, this shows the importance of selecting a proper value for the model parameters, something that is usually ignored in SPH studies. Because the porosity of the porous medium in this

study was very small, where the Forchheimer equation fails to predict close match with experiments (*Joseph et al.*, 1982), there was uncertainty in determination of a suitable Forchheimer coefficient.

The EISPH model was further validated by simulating an anlytical solution of a Darcy flow. The invigorations showed that the model was able to reproduce the results such as seepage depth variation and stress continuity at the interface between free flow domain and the porous medium.

In conclusion, the model is able to reproduce multi-fluid flows in porous media with sufficient accuracy. However, the effects of experimental parameters such as coefficient of molecular diffusivity, turbulent eddy diffusivity, and Forchheimer coefficient require further study.

CHAPTER 5

Applications of the multi-fluid SPH solver in porous media

This chapter comprises the submitted paper:
Basser, H., Rudman, M., & Daly, E. Smoothed Particle Hydrodynamics modelling of fresh and salt water dynamics in porous media. Journal of Hydrology.

5.1 Introduction

The EISPH model employed in Chapter. 4 is applied to simulating sea water intrusion in a freshwater aquifer. The model is further developed to simulate pumping to model salt water upconing below freshwater extraction wells.

To simulate the pumping, three methods were developed to simulate a mass sink to account for the removal of mass required due to the extraction of water. To validate the results two laboratory scale experiments including formation of a freshwater lens in an island, induced by fresh water recharge, and salt water upconing in an experimental island were used.

The method used in this chapter is also explained in Chapter. 3 of this thesis.

5.2 Submitted paper

See the submitted paper starting from the following page.

Smoothed Particle Hydrodynamics modelling of fresh and salt water dynamics in porous media

Hossein Basser[a,*], Murray Rudman[b], Edoardo Daly[a]

[a] *Department of Civil Engineering, Monash University, VIC 3800, Australia*
[b] *Department of Mechanical and Aerospace Engineering, Monash University, VIC 3800, Australia*

Abstract

Seawater intrusion modelling is often used to assist with groundwater management in coastal areas and islands. Although Smoothed Particle Hydrodynamics (SPH) schemes are able to simulate multi-fluid flows in porous media, they have not been widely tested against experimental observations yet. Additionally, numerical methods for groundwater flow problems need to be able to simulate pumping, which is an unexplored area in SPH. In this study, an Explicit Incompressible SPH (EISPH) solver for multi-fluid flow in porous media is used to simulate the dynamics of freshwater lenses in small islands, and is further developed to simulate groundwater pumping and associated seawater upconing. Three methods to implement a sink term that models water pumping from an aquifer are proposed and compared. The model is successfully tested against data from published laboratory-scale experiments and other numerical models. The results of EISPH are comparable to other models. The inclusion of a sink for water particles to simulate pumping did not affect the stability of the simulations, although one of the three methods led to results that better compared to experimental data. Hence, SPH modelling of groundwater flows in porous media can be successfully achieved using the methods developed here.

*Corresponding author
Email address: hossein.basser@monash.edu (Hossein Basser)

Keywords: Smoothed particle hydrodynamics (SPH), Explicit Incompressible SPH (EISPH), freshwater lens, upconing, pumping, porous media, sink

1. Introduction

Seawater intrusion in groundwater aquifers is a global issue that threatens availability of potable freshwater in coastal zones. A naturally occurring process, seawater intrusion is often enhanced by changes in fresh groundwater levels caused by pumping through extraction wells and land-use change [1]. The change in groundwater levels causes reductions in the pressure exerted by overlying freshwater columns, leading to upward intrusion of underlying seawater [2]. The intrusion reduces freshwater storage volume and might contaminate freshwater extraction wells [1].

Seawater intrusion is also of great importance in oceanic islands, where fresh groundwater is often the only potable water source [3]. In oceanic islands, fresh groundwater often floats over underlying seawater due to the density difference. This floating body of freshwater is called a lens [3, 4]. Freshwater lenses in oceanic islands often have limited thickness and are separated from the underlying seawater by a mixing zone. Dynamics of the mixing zone at the interface between freshwater and seawater are governed by a density-dependent multi-fluid flow [5]. Factors associated with changes in rainfall regimes and excessive pumping of freshwater can reduce the thickness of these lenses as well as increase the possibility of seawater intrusion to extraction wells [3, 5].

To investigate the process of seawater intrusion and understand the vulnerability of fresh groundwater aquifers, numerous methods such as field monitoring techniques, analytical studies, and numerical models have been developed [1]. Field techniques, such as direct sampling and remote sensing [6], are used as the basis for empirical equations [5]. Analytical solutions have been developed

to predict the position of an interface between freshwater and seawater. These methods mostly assume a sharp interface between two immiscible fluids and are derived for simplified steady-state conditions in homogeneous aquifers [7, 8, 9]. Numerical methods have been developed to overcome the limitations of analytical solutions and are able to model transient development of the interface of miscible fluids in aquifers with spatial hydraulic heterogeneity. Numerical models mostly solve a variable density multi-fluid flow coupled with a solute transport equation [1]. The most commonly used codes are SUTRA [10] and SEAWAT [11], which solve the equations using finite-elements and finite differences, respectively. Readers are referred to [1] and [5] for a comprehensive review of common analytical and numerical studies.

Recently, particle methods, such as Smoothed Particle Hydrodynamics (SPH), have been used to simulate multi-fluid flow in porous media, with applications to lock-exchange [12, 13]. Further quantitative studies with applications to engineering problems are required to test the capability of SPH to simulate multi-fluid flow in porous media. Specifically, the simulation of problems including pumping from wells requires modelling a mass sink. SPH modelling of sinks are rare in the literature. One of the challenges associated with simulating a mass sink is tracking the particles around the sink point to ensure a well organised distribution of the particles, to ensure an accurate SPH approximation. Another challenge is defining how to remove mass associated with the extracted freshwater.

The aim of this study is thus to investigate the applicability of an SPH scheme, Explicit Incompressible SPH (EISPH) [12], to simulate freshwater lens formations in islands and sea water upconing due to pumping. An algorithm to simulate point mass sinks was developed and is presented here with applicability to water pumping.

2. Methods

2.1. Governing equations

The 2D governing equations for a flow of two or more incompressible fluids in saturated porous media with mass sinks and solute transport are [12, 14]

$$\nabla \cdot \vec{u} = -\Gamma, \tag{1}$$

$$\frac{D\vec{u}}{Dt} = -\frac{\epsilon}{\rho}\nabla p + \frac{\mu}{\rho}\nabla^2\vec{u} + \epsilon\vec{g} + \vec{R}, \tag{2}$$

$$\frac{DC}{Dt} = \nabla \cdot (\mathcal{D}_d \nabla C), \tag{3}$$

where Eqs. 1, 2 and 3 define mass, momentum and species conservation, respectively, $\vec{u}$ is the Darcian velocity equal to $\epsilon\vec{u}_f$, $\vec{u}_f$ being the fluid intrinsic velocity and ϵ porosity, Γ is a flux per unit of volume due to point sinks, p is pressure, μ is the dynamic viscosity, ρ is the density, $\vec{g}$ is the gravitational acceleration, $\vec{R}$ is the drag force imposed by porous media, $\mathcal{D}_d$ is the effective dispersion matrix of size 2 for the scalar, and C is scalar concentration.

2.2. SPH approximation

In SPH, the fluid domain is represented as an ensemble of Lagrangian particles. The variable values at each particle are interpolated using the neighbouring particles. Readers are referred to [15], [16] and [17] for a general description of the particle approximation; only key features of the model used in this study are presented here. The spatial volume, V, of particles in porous media with

spatially varying porosity is determined in accordance with the porosity of the media, such that, when a particle moves into a medium with lower porosity, the same amount of mass occupies a larger volume (i.e., $V = m/(\epsilon\rho)$, where m is the fluid mass of the particle) [12, 18].

The particle approximation of the governing equations reads [19, 20, 12]

$$\nabla \cdot \vec{u}_i = \sum_{j=1}^{N} \frac{m_j}{\epsilon_j \rho_j} (\vec{u}_j - \vec{u}_i) \cdot \nabla_i W_{ij} = -\Gamma_i, \tag{4}$$

$$\frac{D\vec{u}_i}{Dt} = \epsilon_i \sum_{j=1}^{N} \frac{m_j}{\epsilon_j} \left(\frac{p_i}{\rho_i^2} + \frac{p_j}{\rho_j^2} \right) \nabla_i W_{ij} + \sum_{j=1}^{N} \frac{4 m_j (\mu_i + \mu_j) \vec{u}_{ij} \cdot \vec{x}_{ij}}{\epsilon_j (\rho_i + \rho_j)^2 \left(|\vec{x}_{ij}|^2 + \eta^2 \right)} \nabla_i W_{ij} + \epsilon_i \vec{g} + \vec{R}_i, \tag{5}$$

with

$$\vec{R}_i = -\frac{\epsilon_i \mu_i}{\rho_i \kappa_i} \vec{u}_i, \tag{6}$$

$$\frac{DC_i}{Dt} = 2 \sum_{j=1}^{N} \frac{m_j}{\epsilon_j \rho_j} \left(\frac{e_{ij,1}^2}{\bar{\mathcal{D}}_{dij,11}} + \frac{e_{ij,2}^2}{\bar{\mathcal{D}}_{dij,22}} \right)^{-1} \frac{\vec{x}_{ij} \cdot \nabla_i W_{ij}}{|\vec{x}_{ij}|^2 + \eta^2} (C_i - C_j), \tag{7}$$

where i and j refer to the i^{th} and j^{th} particles, κ is the permeability of the medium, assumed to be constant, e_{ij} is a unit vector from i to j, $\bar{\mathcal{D}}_{dij}$ is the average of the effective dispersion matrices of particles i and j, the numbers in subscript of e_{ij} and $\bar{\mathcal{D}}_{dij}$ reference a particular element in the vector and the

matrix, respectively. Eq. (6) equals zero where there is no porous medium.

The EISPH method was used to solve Eqs. 1 - 3 [21]; a detailed description of the numerical scheme used here is presented in Appendix A.

2.3. Modelling a point sink

To carry out SPH simulations of problems including water extraction through wells, a method to describe a sink for the extraction of water mass must be developed.

In a point sink, such as suction or pumping acting at a point, the fluid surrounding the sink point moves toward the sink point. In SPH, this means that fluid particles should move toward the sink point and a portion of the fluid's mass should be removed at a rate equal to the sink rate. The extraction of the mass from a point is included in Eq. (1) [14] in the form of fluid flux per unit of volume, Γ, and is approximated as

$$\Gamma = \sum_{k=1}^{s} Q_k \delta(\vec{x} - \vec{x}_k), \tag{8}$$

where k is the k^{th} sink point, s denotes the number of sink points, Q is the sink rate and $\delta(\cdot)$ is the Dirac function. Eq. (8) describes fluid flux per unit volume due to sinks. The contributions of sinks for particle i is approximated as

$$\Gamma_i = \sum_{k=1}^{s} Q_k \delta(\vec{x}_i - \vec{x}_k) \approx \sum_{k=1}^{s} Q_k \zeta_k W_{ik}, \tag{9}$$

where ζ is a normalization factor equivalent to an approximation of constant 1 and defined as [22, 19]

$$\frac{1}{\zeta_k} = \sum_{j=1}^{N} \frac{m_j}{\epsilon_j \rho_j} W_{jk}. \tag{10}$$

In Eq. (9), sink points within a distance equal to the radius of the support of the kernel function from particle i are used to calculate Γ; therefore, a sink point directly affects the particles (sink particles hereafter) within a distance equal to the radius of the support domain of the kernel function from the sink point. The particles outside the direct influence of the sink point are indirectly affected through their interaction with the sink particles.

The term Γ contributes to the pressure Poisson equation (Eq. A.5), causing the pressure of the particles surrounding the sink point to change in a way that they move towards the sink point.

Each particle in SPH carries a certain amount of fluid mass and in order to account for the mass extraction due to the sink, it is unavoidable to reduce the particles mass and delete particles where and when necessary. Three different methods for deleting particles are proposed to investigate their advantages and disadvantages.

2.3.1. Solely Particle Removal (SPR)

In this method, the mass reduction due to the sink is handled by just deleting particles, while maintaining the total particle mass constant in between deletion. Individual particle mass still needs to be updated due to changes in scalar concentration according to Eq. (7). One particle is deleted after a certain number of time steps. The duration, t_p, required to delete one particle is determined using the volume of fluid in a particle and the sink rate, such that

$$t_p = \frac{\epsilon V}{Q}, \tag{11}$$

where V is a spatial volume (Section 2.2) associated with a particle, and ϵV is

the volume of fluid that each particle carries. Mass is reduced (i.e., one particle is removed) at every time step that is a multiple of t_p (i.e., at times $t = \alpha t_p$, α being an integer). Every time $t = \alpha t_p$, the particle closest to the sink point is removed (Fig. 1a).

Because the sink particles move toward the sink point due to the inclusion of Γ in the pressure Poisson equation (Eq. A.5), the particle deletion does not lead to a void in the vicinity of the sink point.

2.3.2. Mass Reduction and Particle Removal (MRPR)

Similar to *SPR*, one particle is removed every certain number of time steps. However, in contrast to *SPR*, the mass of sink particles is gradually reduced every time step before one particle is deleted. The amount of mass reduction in one time step is divided among the sink particles and subtracted from each sink particle's mass. The mass required to be removed is partitioned between sink particles in two ways: (1) in accordance to the kernel value ($MRPR_K$), so that the particles closer to a sink point lose more mass than the distant ones, or (2) evenly ($MRPR_E$). Therefore, the amount of mass extracted from each particle is determined using the sink rate, time step value, kernel value (used in $MRPR_K$), and number of sink particles (used in $MRPR_E$). When the time required to delete one particle, αt_p, is reached, the closest particle to the sink point is removed and the mass of the remaining sink particles is set back to their initial mass value (Fig. 1b).

2.3.3. Constant Mass Reduction (CMR)

In this method, the mass of the sink particles is gradually reduced every time step, as in $MRPR_E$. The reduction in mass of the sink particles continues until the mass of a sink particle drops below a cut-off value, which here is set to 1% of particles initial mass value, at which time the particle is removed (Fig. 1c).

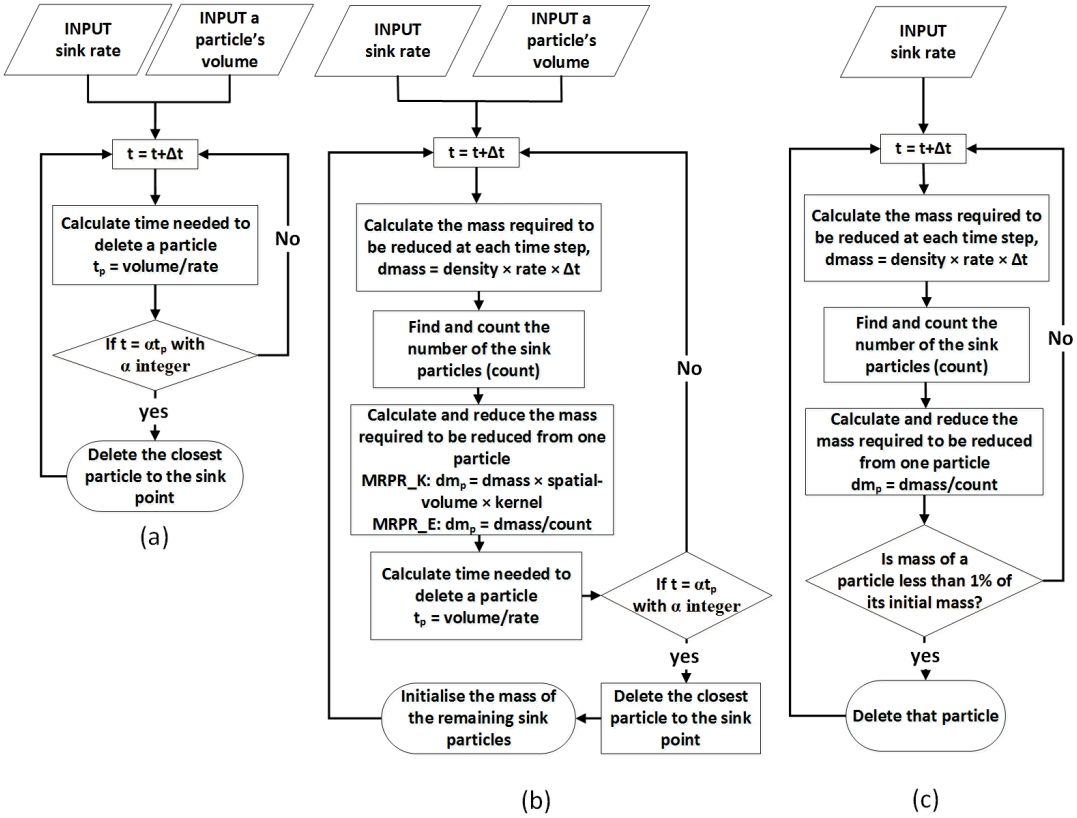

Figure 1: The procedure for the reduction of mass due to a sink point using (a) Solely Particle Removal (SPR) (Section 2.3.1), (b) Mass Reduction and Particle Removal (MRPR) (Section 2.3.2) and (c) Constant Mass Reduction (CMR) (Section 2.3.3).

The reduction of mass in accordance to the kernel value (as in $MRPR_K$) was found problematic as continuous reduction of particles mass causes clumping of particles close to a sink point; this is further explained in section 3.2.

2.4. Choice of kernel

The selection of a kernel function and smoothing length in a problem in media with different porosities should be handled carefully. The spatial volume that an SPH particle occupies within a porous medium represents both fluid

and solid phases volume. Therefore, a fluid particle with a given mass within a porous medium has a larger spatial volume than a particle in a free flow domain with the same mass. Having a larger spatial volume causes the particles to move apart from each other, leading to a loss of resolution inside the porous medium. Therefore, the number of particles inside the support domain of the kernel function reduces and might not be sufficient to accurately approximate the variable values and derivatives. To tackle this problem, a kernel function with a larger support domain should be used or the smoothing length should be adjusted [18]. The former approach might lead to an excessive smoothing of the variable values at the free flow domain. Furthermore, using a larger support domain increases the number of interactions in the free flow domain, leading to a higher computational cost. Here we use a variable smoothing length. Additional terms associated with the derivative of smoothing length are added to the momentum equation [23]; however, these terms are neglected here.

A cubic spline weighting function [24], with a variable smoothing length, was used here and is given by

$$W(q,h) = \alpha_d \times \begin{cases} \frac{2}{3} - q^2 + \frac{1}{2}q^3 & 0 \le q < 1 \\ \frac{1}{6}(2-q)^3 & 1 \le q < 2 \\ 0 & q \ge 2, \end{cases} \tag{12}$$

where α_d is a normalisation constant equal to $1/h$, $15/(7\pi h^2)$, or $3/(2\pi h^3)$ in one-, two- and three-dimensional domains, respectively, and $q = |\vec{x}_i - \vec{x}_j|/h = |\vec{x}_{ij}|/h$. In 2D we choose the smoothing length to be inversely proportional to square root of porosity, so that in a medium with lower porosity value the smoothing length is larger.

Because the same value of smoothing length should be used for a pair of in-

teracting particles to conserve momentum, the smoothing length for interacting particles i and j is calculated as $h_{ij} = (h_i + h_j)/2$ [25].

2.5. Boundaries

2.5.1. Solid boundaries

A single layer of virtual particles is used to impose the impermeable boundaries at walls. Virtual particles interact with fluid particles and prevent them from penetrating the walls by exerting a Lennard-Jones repulsive force given by [16]

$$F(\vec{x})_{ij} = \begin{cases} V_L \left[\left(\frac{r_c}{|\vec{x}_{ij}|} \right)^{c_1} - \left(\frac{r_c}{|\vec{x}_{ij}|} \right)^{c_2} \right] \frac{1}{|\vec{x}_{ij}|} & \frac{r_c}{|\vec{x}_{ij}|} \geq 1, \\ 0 & \frac{r_c}{|\vec{x}_{ij}|} < 1, \end{cases} \tag{13}$$

with c_1 and c_2 equal to 4 and 2 respectively, V_L is the square of the largest velocity in a flow, and r_c represents a cut off distance which is set to 0.8 times the initial distance between virtual particles. The virtual particles are fixed in their position and never move. The initial distance between the virtual particles is set to half the initial distance between the fluid particles to ensure the impermeability of the walls.

2.5.2. Free/no-slip boundaries

Ghost particles are used to impose free-slip and no-slip boundary conditions. Ghost particles are created by mirroring the fluid particles within a distance of $2h$ from the solid boundaries [24]. A ghost particle carries the same properties of the associated fluid particle. To impose no-slip boundary condition both components of velocity, parallel and normal, are reversed, while for free-slip conditions only the normal component is reversed [26].

2.5.3. *Inflow boundaries*

Inflow particles are used to simulate inflow of fluid into the domain [27]. The thickness of the zone occupied by inflow particles, i.e., the inflow zone, is set to be larger than the radius of the support domain of the kernel function. Inflow particles within the inflow zone are moved with a constant velocity determined by the inflow rate. Once an inflow particle moves outside the inflow zone, it is turned into a fluid particle and moves according to the governing equations. The inflow particles' velocity and pressure are used in approximating the hydrodynamics of the fluid particles in a domain but not vice versa [28].

2.5.4. *Free surface boundaries*

A pressure $p = 0$ is assigned to free surface particles. The free surface particles are detected using fluid particles' densities as in [12].

3. Results

The model is applied to two experimental studies to test different aspects of the method and validate it. The experimental coastal freshwater lens in an isotropic porous medium studied in [3] is simulated to check the capability of the model to reproduce the dynamics of fresh and salt water in a porous medium. The experiment of salt water upconing induced by fresh water pumping studied in [29] was simulated to validate the proposed sink algorithm and demonstrate the capability of the SPH scheme to reproduce upconing of salt water in groundwater aquifers.

3.1. *Laboratory-scale coastal freshwater lens*

An experiment of formation of a coastal freshwater lens in a cone shape strip island was presented in [3]. In the experiment, a cone shape submerged island 1.8 m long, 0.3 m deep, and 0.05 m wide was utilized (Fig. 2). The porosity

and mean hydraulic conductivity of the porous medium were given as $\epsilon = 0.39$ and $K = 4.5 \times 10^{-3}\,\mathrm{m\,s^{-1}}$, respectively. The salt and fresh water densities were $\rho_s = 1021.2\,\mathrm{kg\,m^{-3}}$ and $\rho_f = 997.4\,\mathrm{kg\,m^{-3}}$, respectively. Initially the island was saturated up to $y = 0.3$ m with salt water to represent the ocean. Freshwater was recharged, with a rate equal to $q = 1.33 \times 10^{-5}\,\mathrm{m\,s^{-1}}$, through a set of drips above the sand cone. The recharged fresh water penetrated into the porous medium (i.e., island) and formed a freshwater lens as shown in Fig. 2. As the experiment progressed, an amount of freshwater discharged from the island to the surrounding salt water representing the ocean. This water was skimmed from the salt water surface (Fig. 2) to maintain a constant salt water level [3].

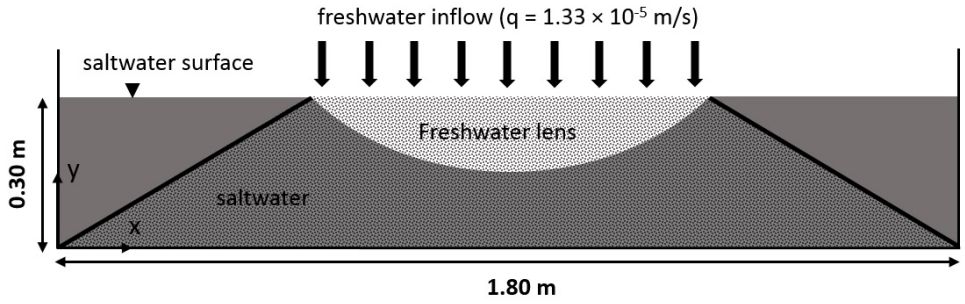

Figure 2: The experimental tank used in [3] (Section 3.1).

In the simulation, a plane of symmetry was assumed requiring only half of the experimental domain to be simulated; this is similar to the numerical study performed in [4]. The left side of the island was simulated, and a free-slip boundary condition was used on the right wall of the domain to satisfy the symmetry of the flow. The initial spacing between fluid particles ($\Delta x = \Delta y$) was set to 0.005 m in the ocean, and $0.005/\sqrt{\epsilon}$ m in the island. The smoothing length, h, was set to $1.2\Delta x$, with Δx varying in the ocean and island. The time step was set to 2×10^{-4} s. The dynamic viscosity for the

fresh water was set to $\mu_f = 10^{-3}$ Pa $\cdot$ s and it was assumed to be $\mu_s = 1.05 \times 10^{-3}$ Pa $\cdot$ s for the salt water [30]. The calculated permeability was $\kappa = 4.6 \times 10^{-10}$ m^2, using the properties of freshwater and hydraulic conductivity. No-slip boundary conditions were imposed on the left and bottom solid boundaries. The longitudinal and transverse dispersivity, included in Eq. (A.16), were set to $d_l = 5 \times 10^{-4}$ m and $d_t = 5 \times 10^{-5}$ m, and the coefficient of molecular diffusivity was set to $D_m = 10^{-9}$ m^2 s^{-1} [4]. The freshwater recharge at the surface of the island was simulated using an inflow boundary condition (Section 2.5.3). The pressure within the inflow zone was set to be hydrostatic at every time step. Outside the island, particles that moved above $y = 0.3$ m, were deleted to keep the water level constant and mimic the experimental procedure.

Fig. 3 shows the freshwater lens and the pressure distribution at different times. The coarser resolution of particles in the porous medium is due to the definition of spatial volume, that changes in accordance to porosity of the medium. Experimental or numerical pressure measurements are not available and a qualitative discussion is reported here. The value of maximum pressure in the porous medium is higher than that of the free flow domain; this is due to the extra pressure imposed by the inflow particles over the surface of the island. It was found that changing the thickness of the inflow zone, which changed the hydrostatic pressure at the surface of the island accordingly, affected the maximum thickness of the lens predicted numerically. Our investigations showed that the thickness of the inflow zone should be equal to the radius of the support domain of the kernel function. The definition of pressure at inflow boundary condition in SPH is still an open issue, with examples [27] showing the need to adjust the size of inflow zone to reproduce experimental data.

Oscillations in pressure values occurred at the interface between the free flow domain and the porous medium (Fig. 3). This might be due to the fact that

for a support domain with its centre located right over the interface there are different numbers of particles within it from the two media. Our investigations showed that these oscillations do not significantly affect the numerical results.

It was found that with the proper boundary arrangements, the transient formation as well as the maximum thickness of the lens were reasonably reproduced. The numerical maximum thickness of the lens occurred close to the right boundary which is in agreement with the experimental and numerical results in [3, 4]. Fig. 4a shows the comparison of the experimental and numerical transient development of the lens thickness. The maximum depth predicted numerically was 16 cm and occurred in the middle of the island after 200 min; this was close to the maximum thickness measured experimentally, 15 cm, that occurred at the same time.

It is observed in Fig. 3 that the density of salt water in the free flow domain, at the interface between the free flow domain and the porous medium and close to the free surface, is lower than the salt water density. This was due to a horizontal flow within the lens, from the symmetry boundary toward the left; this was observed in the experiment [3] and numerical benchmark by [4]. It was also found that an amount of the discharged fresh water into the ocean moved back to the island, and again converged with the horizontal flow of lens water into the salt water surface (Fig. 3, $t = 200$ min). This represents the direction of the salt water flow from the free flow domain into the porous medium. A similar flow direction was observed in the simulation of [4].

It is observed that the thickness of the transition between freshwater and salt water is larger close to the symmetry boundary; likely due to the higher vertical velocity of particles close to the symmetry boundary as the effective dispersion matrix is proportional to the velocity of particles.

The simulation was repeated for four other recharge rates and the maximum

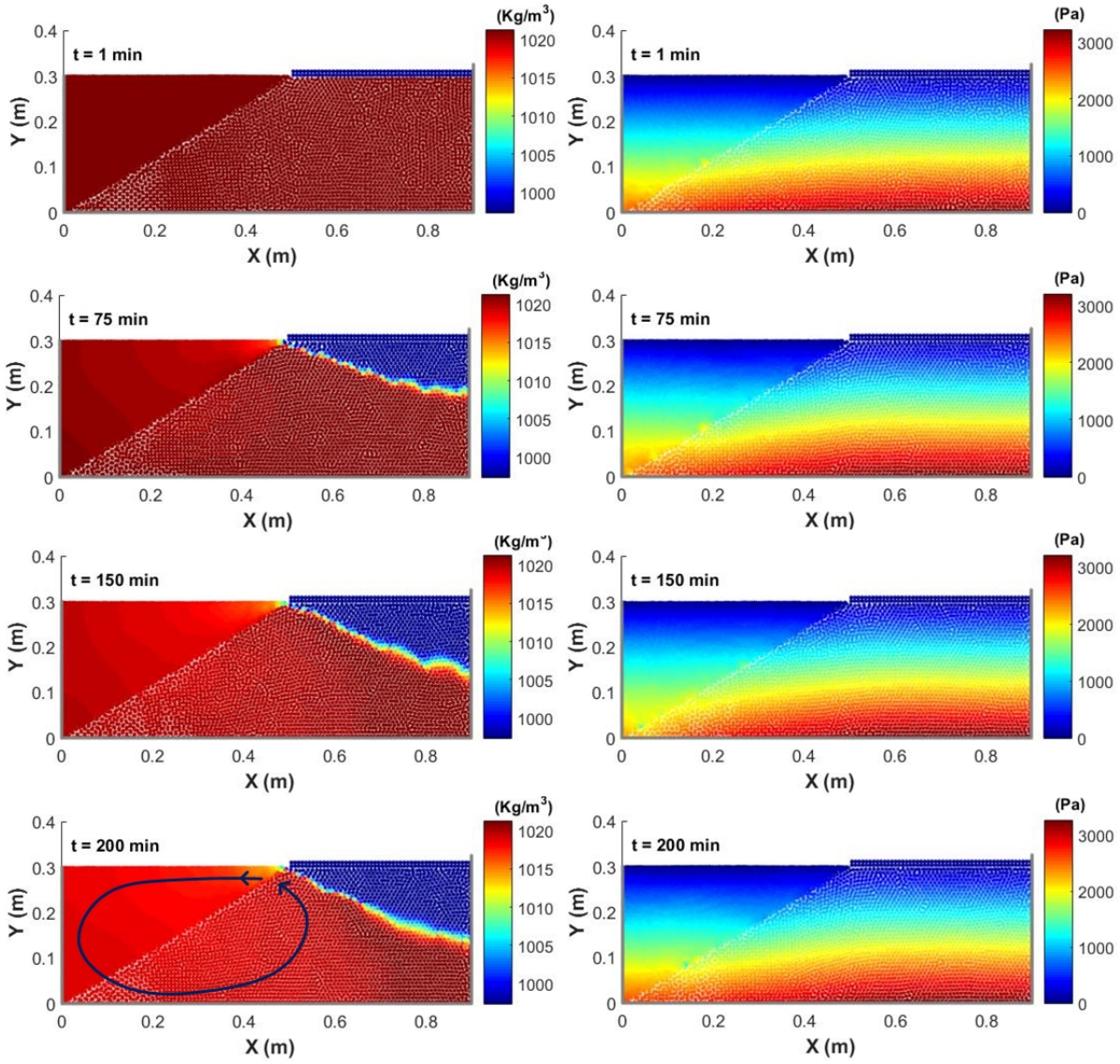

Figure 3: Distribution of fluid density (left) and pressure (right) at different times (Section 3.1).

lens thickness was compared to numerical and analytical solutions [3, 8, 7] to investigate the capability of the model to predict the maximum thickness as a function of recharge rate. As observed in Fig. 4b, the EISPH results are in good agreement with the numerical and analytical results.

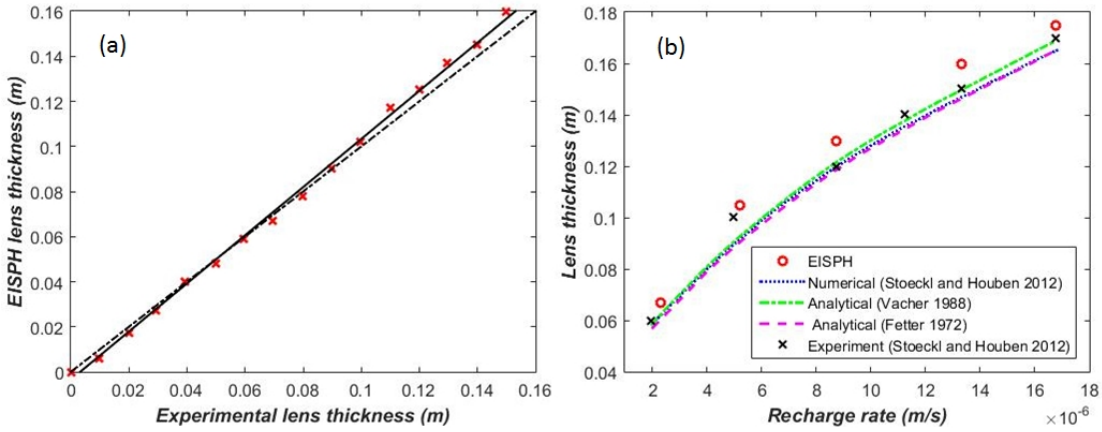

Figure 4: Comparison of the EISPH results against experimental data for (a) transient maximum lens thickness development (each cross sign represents numerical vs experimental maximum lens thickness at a specific time, continuous line represents the best fit for the cross signs, and the dashed line represents an exact match) and (b) maximum lens thickness as a function of recharge rate (Section 3.1).

The results show that the EISPH can be used to well simulate applications associated with multi-fluid flows in porous media.

3.2. Salt water upconing in a two-dimensional aquifer

A series of experiments of salt water upconing were presented in [29] and their experiment 2 was used for comparison of the simulations here. In the experiment, a tank 1.18 m long, 1.2 m deep, and 0.053 m wide was used, as shown in Fig. 5. Four pipes fed freshwater and one pipe fed salt water to the tank from both sides. The conductance (i.e., resistance of the porous medium against the inflow) was measured as $M_f = 2.84 \times 10^{-6}$ m^2 s^{-1} and $M_s = 1.62 \times 10^{-6}$ m^2 s^{-1} for the fresh water and salt water, respectively [31]. Initially the

tank was filled up to 0.15 m with salt water and 1 m depth of fresh water was filled over the salt water leading to an overall depth $H_b = 1.15$ m (i.e., the fresh water head measured from the base of the tank). Fresh water was extracted, using an extraction well with diameter equal to 0.012 m, at the rate $Q_p = 7 \times 10^{-5}\ \mathrm{m^2\,s^{-1}}$. The well was placed in the middle of the tank at a depth of 0.65 m from the top of the tank so that the distance between the well bottom to the initial interface of freshwater and salt water was 0.4 m [31]. The freshwater inflow to the well occurred at the lower 0.1 m of it. The porosity and hydraulic conductivity were given as $\epsilon = 0.38$ and $K = 1.6 \times 10^{-3}\ \mathrm{m\,s^{-1}}$, respectively. The density of the salt and fresh water were $\rho_s = 1025\ \mathrm{kg\,m^{-3}}$ and $\rho_f = 998\ \mathrm{kg\,m^{-3}}$, respectively [29, 31]. Two manometers were attached at the boundaries at both sides to measure any drawdown in the fresh water and salt water head. As the freshwater and salt water head dropped at the boundaries, an inflow was induced to feed the domain with both freshwater and salt water. Therefore, the side boundaries acted as head dependent boundaries.

In the simulation, the initial spacing between fluid particles ($\Delta x = \Delta y$) was set to $0.005/\sqrt{\epsilon}$ m. The smoothing length, h, was set to $1.2\Delta x$ and the time step was 2×10^{-4} s. The dynamic viscosity for the fresh water was set to $\mu_f = 10^{-3}\ \mathrm{Pa \cdot s}$ and it was assumed to be $\mu_s = 1.05 \times 10^{-3}\ \mathrm{Pa \cdot s}$ for salt water [30]. The calculated permeability was $\kappa = 1.67 \times 10^{-10}\ \mathrm{m^2}$, using the parameters of salt water and hydraulic conductivity. The lower section of the well (dashed zone in Fig. 5), where freshwater was flowing into, was treated as a high permeability section (i.e., the drag force in Eq. 6 was set to zero), and its length was assumed to be 0.05 m [31]. The sink point location was set at the middle of the permeable zone. A no-slip boundary condition was imposed at the bottom solid boundary. The coefficient of molecular diffusivity was set to $D_m = 10^{-9}\ \mathrm{m^2\,s^{-1}}$, and the longitudinal and transverse dispersivity were set

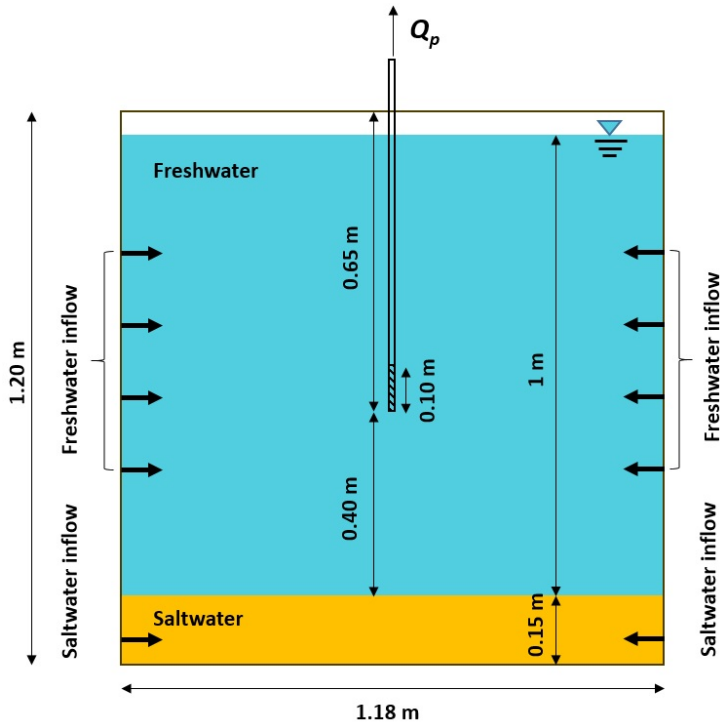

Figure 5: The view of the tank used in the experiment by [29] (Section 3.2).

to $d_l = 2 \times 10^{-3}$ m and $d_t = 1 \times 10^{-4}$ m [31].

The fresh water and salt water recharge were simulated using an inflow boundary condition (Section 2.5.3), with the rate of the inflow determined according to the boundaries' time dependent head. The inflow was simulated as a continuously distributed recharge rather than inflow nodes or pipes. This was due to the nature of SPH, as a kernel close to the boundaries needs to be filled with particles to result in an accurate approximation. The width of the inflow zones, on the left and right boundaries, were set to 0.04 m, which was larger than the radius of the support of the kernel function. The inflow rate for fresh water, q_f ($\mathrm{m\,s^{-1}}$), and salt water, q_s ($\mathrm{m\,s^{-1}}$), was calculated using the conductance, initial boundary head (H_b), and time dependent internal head at

the boundaries (H_t) as [31]

$$q_f = M_f(H_b - H_t)/(((H_b - 0.15)/4) \times 0.053), \tag{14}$$

and

$$q_s = M_s(H_b - H_t)/(0.15 \times 0.053), \tag{15}$$

where H_t was assumed to be the average of the freshwater heads on the left and right boundaries, to ensure a symmetrical inflow, as it was observed in the experiment [29].

Fig. 6 shows the numerical and experimental density distribution and transient development of the upconing below the extraction well using the method *SPR* (See section 2.3). The qualitative observation is generally in agreement with the experiment in [29]. The larger dispersion of salt water near the sides of the tank might be caused by salt water particles inside the tank and close the inflow zones that were allowed to interact with the freshwater particles in the inflow zones. Our investigations showed that using a smaller values for longitudinal and transverse dispersivity did not considerably affect the dispersion zone width. A thicker dispersion zone, but with smaller extent, was also observed in the simulations of [31]. This thicker dispersion zone might also be related to the assumption in the SPH approximation of the diffusion equation (see Eq. A.15 - A.18).

Fig. 7 illustrates the upconing height as a function of time. The numerical height of the upconing was determined based on the simulated 50% salinity contour [31]. It was observed that the *SPR* method led to results comparatively closer to the experimental observations. The *CMR* method considerably overes-

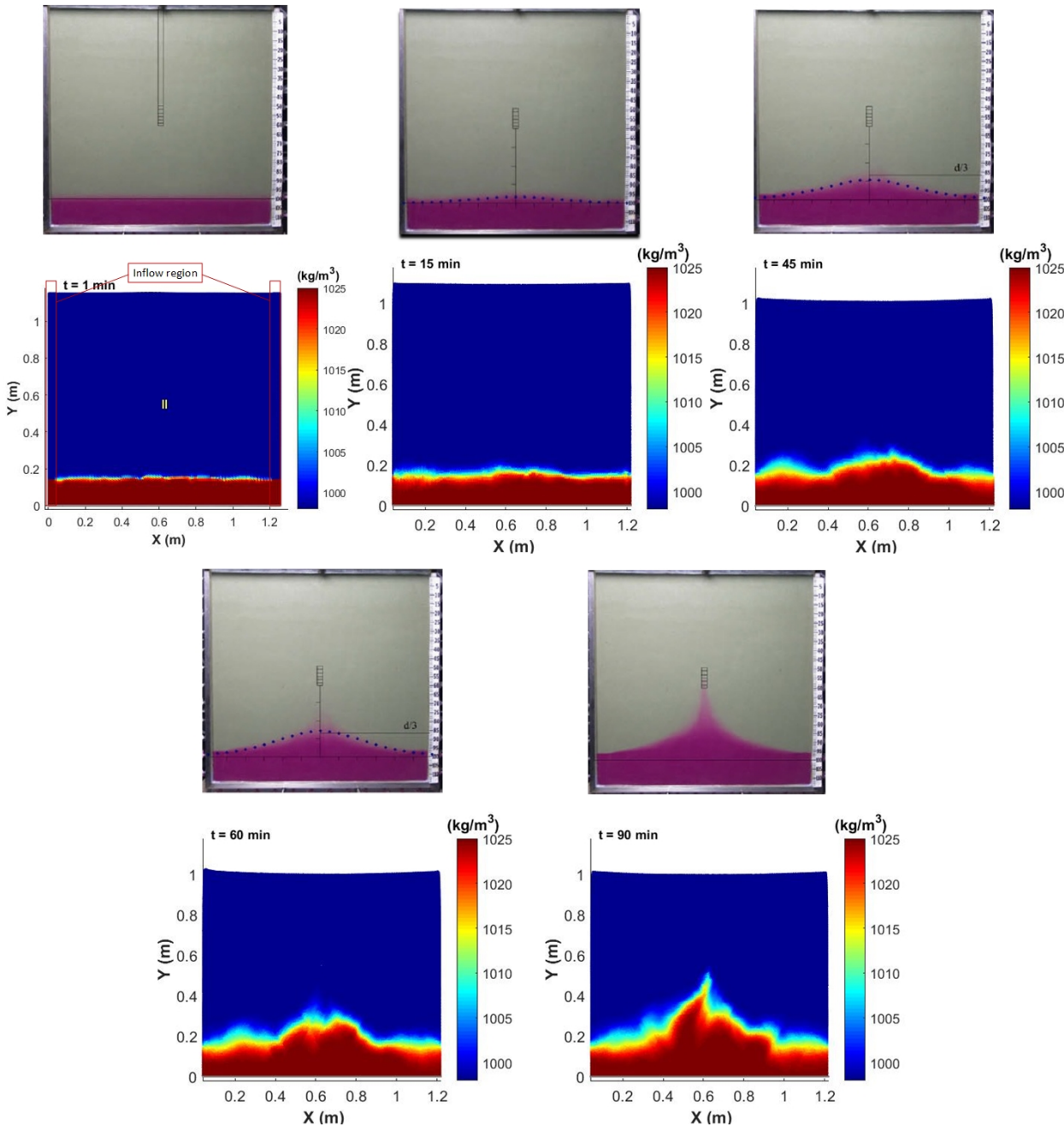

Figure 6: Numerical and experimental transient development of the salt water upconing below the single sink point using method *SPR* (the yellow lines, representing the bottom (high permeable) section of the well, are only shown for visualisation purpose) (Section 3.2) [29].

timated the upconing heigh, possibly because of the particle distribution pattern around the sink point. Fig. 8a shows the particles and their density around the sink point for the three methods. The particles have an ordered distribution around the sink point in *SPR*, while the particles are clumped for *CMR*. The clumping in *CMR* is due to the continuous reduction of mass for the sink particles, until their mass drops to zero. With the density of the particles around the sink point staying constant, the reduction in mass causes the particles to get closer to the sink point. Therefore, any support domain of kernels located in the vicinity of the sink area might be truncated causing an error in the particle approximations. The clumping was also observed in the method *MRPR*, to a smaller extent, especially when implementing $MRPR_K$, because particles mass were set to their initial value when a particle was removed. Fig. 8b shows the pressure distribution around the sink point. The sudden removal or mass reduction of sink particles have not caused unphysical pressure distribution around the sink point. Fig. 8c shows the velocity vectors around the sink point. It is observed that the particles generally move toward the sink point in the three methods. As the particles enter the area that is affected by the sink point, the velocity of the particles increase considerably. It is observed that velocity vectors have relatively organised distribution in $MRPR_K$ and SPR. Detailed investigation of the velocity values for the sink particles requires further study.

The stability of the simulations and the qualitative and quantitative results show the capability of the sink algorithms to reproducing fresh water pumping in aquifers.

4. Conclusion

Application of SPH schemes to multi-fluid flows in porous media with different porosities are not very common. In this paper, an EISPH numerical scheme

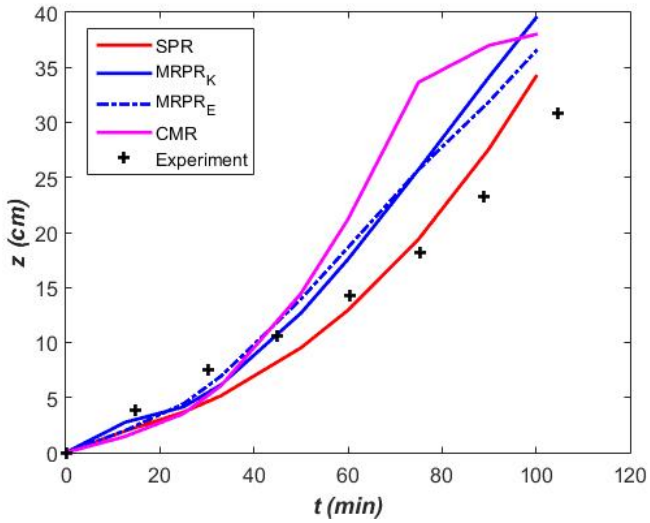

Figure 7: Comparison of upconing height, apex rise, from the observed data and numerical model (Section 3.2).

was used to investigate its applicability to seawater intrusion problems. The focus was on the dynamics of buoyant freshwater lenses in islands and salt water upconing caused by pumping. The model was tested against published results from laboratory experimental and models.

In the case of the freshwater lens, the transient thickness and maximum depth of the simulated lens were in reasonable agreement with experimental data. The simulated maximum depth of the lens as a function of different recharge rates were in agreement with observed, analytical and other numerical results. The imposition of flow boundary conditions to simulate recharge still represents a challenge in SPH. The lens dimensions obtained with EISPH depended on the thickness of the inflow zone, as this controlled the value of hydrostatic pressure acting on the surface of the island. This depths was thus calibrated to best reproduce experimental data. The inclusion of pumping was the main challenge to model salt water upconing. A new procedure for implement-

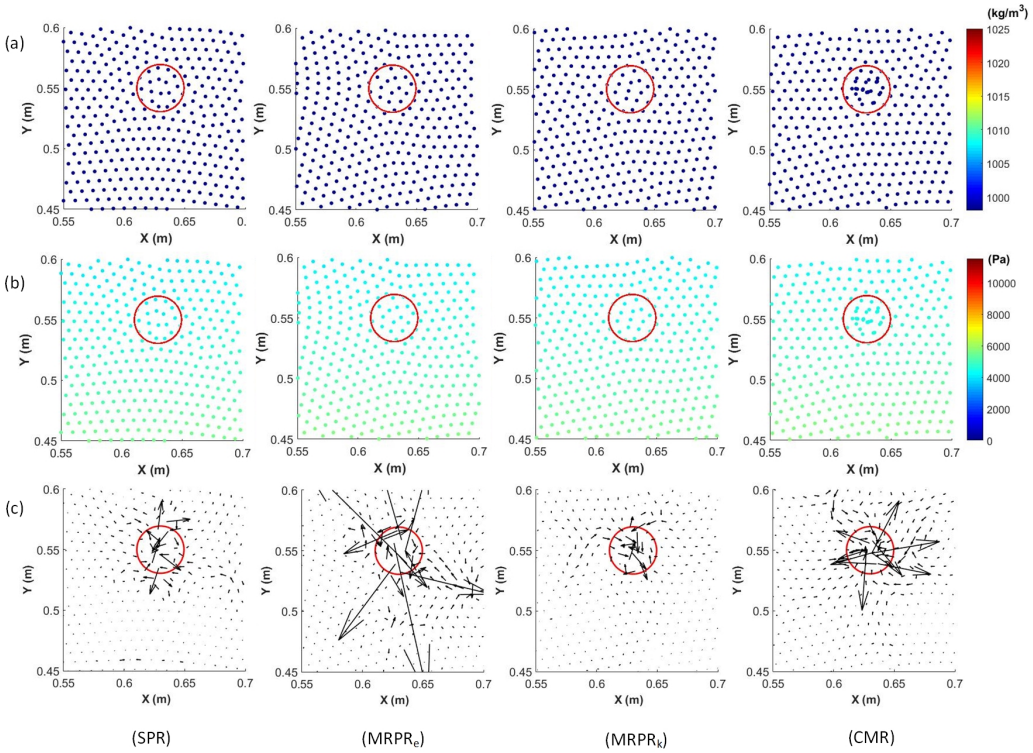

Figure 8: Distribution of particle (a) density, (b) pressure, and (c) velocity vectors around the sink point, $X = 0.63$ m and $Y = 0.55$ m, $t = 50$ min (Section 3.2).

ing a sink in SPH was developed. The divergence of the velocity for the particles in the vicinity of the sink point was adjusted in accordance with the pumping rate to make the particles move toward the sink. The extraction of mass was handled using three different methods indicated as *SPR*, *MRPR*, and *CMR*. *SPR*, where the mass reduction is handled solely through removal of particles, appeared to perform better when compared to experimental observations. The quantitative results of the cases studied here show the effectiveness of EISPH in simulating complex flow conditions and lay the foundation for the inclusion of mass sinks in SPH numerical schemes applied to water pumping. Although applied to 2D configurations, the algorithm developed is also applicable to 3D problems. To preserve reasonable computational times, future avenues to improve the method point toward the extension of the model to radial coordinates or, perhaps, the development of ad-hoc changes of the values of permeability and porosity to generate 2D domains equivalent to 3D axisymmetric problems (e.g., [11]).

Acknowledgements

The Authors thank V. Lemiale and A. Valizadeh for useful discussions.

Appendix A. EISPH scheme

This section presents a detail description of the numerical method used to solve Eqs. (1) - (3) with SPH. Parts of the method are also described in [12, 21].

The governing equations were solved with an EISPH scheme, which employs two steps [32]. The Poisson equation is approximately solved.

In the first step, viscous, gravity and drag forces contribute to the velocity

and position of particles as

$$\vec{u}_i^* = \vec{u}_i^n + \left(\frac{\mu}{\rho}\nabla^2\vec{u}\right)_i^n \Delta t + \epsilon_i^n \left(\vec{g} - \frac{\mu}{\rho\kappa}\vec{u}\right)_i^n \Delta t, \tag{A.1}$$

where $\vec{u}^*$ is intermediate velocity, $\vec{u}^n$ is particle velocity at time $n\Delta t$, with Δt kept constant in all the simulations.

The approximation of the viscous term reads

$$\left(\frac{\mu}{\rho}\nabla^2\vec{u}\right)_i^n = \sum_{j=1}^{N} \frac{4m_j^n(\mu_i + \mu_j)\vec{u}_{ij}^n \cdot \vec{x}_{ij}^n}{\epsilon_j^n(\rho_i^n + \rho_j^n)^2\left(|\vec{x}_{ij}^n|^2 + \eta^2\right)} \nabla_i {W_{ij}}^n, \tag{A.2}$$

where η is a small parameter included to make sure the denominator is non-zero ($\eta = 0.001h_{ij}$, with $h_{ij} = (h_i + h_j)/2$), and $\vec{u}_{ij}^n = \vec{u}_i^n - \vec{u}_j^n$. The gravitational acceleration and the drag term are explicitly calculated.

The intermediate particle positions ($\vec{x}^*$) are calculated as

$$\vec{x}_i^* = \vec{x}_i^n + \frac{\vec{u}_i^*}{\epsilon^n}\Delta t, \tag{A.3}$$

where $\vec{x}^n$ is particle position at time $n\Delta t$. Afterwards, the intermediate porosity of particles, ϵ^*, are assigned using the intermediate position of particles.

In the second step, the particle velocities are calculated at the new time step as

$$\vec{u}_i^{n+1} = \vec{u}_i^* - \frac{\epsilon_i^*}{\rho_i^n}\nabla p_i^{n+1}\Delta t, \tag{A.4}$$

where p^{n+1} is particle pressure at time $(n+1)\Delta t$. Eqs. (A.4) and (1) are

combined to form the pressure Poisson equation as

$$\nabla \cdot \left(\frac{\epsilon^*}{\rho^n} \nabla p^{n+1} \right)_i = \left(\frac{\nabla \cdot \vec{u}^* + \Gamma}{\Delta t} \right)_i , \tag{A.5}$$

where Γ is the contribution of the sink points around particle i (see Section 2.3).

The approximation of the divergence of the intermediate velocity reads

$$(\nabla \cdot \vec{u}^*)_i = \sum_{j=1}^{N} \frac{m_j^n}{\epsilon_j^* \rho_j^n} (\vec{u}_j^* - \vec{u}_i^*) \cdot \nabla_i W_{ij}^*. \tag{A.6}$$

The left hand side of Eq. (A.5) is a Laplacian operator and is approximated as

$$\nabla \cdot \left(\frac{\epsilon^*}{\rho^n} \nabla p^{n+1} \right)_i = \sum_{j=1}^{N} \frac{m_j^n}{\epsilon_j^* \rho_i^n \rho_j^n} \frac{\left(\epsilon_i^* + \epsilon_j^*\right) \vec{x}_{ij}^* \cdot \nabla_i W_{ij}^*}{|\vec{x}_{ij}^*|^2 + \eta^2} \left(p_i^{n+1} - p_j^{n+1} \right), \tag{A.7}$$

so that

$$\sum_{j=1}^{N} \frac{m_j^n}{\epsilon_j^* \rho_i^n \rho_j^n} \frac{\left(\epsilon_i^* + \epsilon_j^*\right) \vec{x}_{ij}^* \cdot \nabla_i W_{ij}^*}{|\vec{x}_{ij}^*|^2 + \eta^2} \left(p_i^{n+1} - p_j^{n+1} \right) = \left(\frac{\nabla \cdot \vec{u}^* + \Gamma}{\Delta t} \right)_i . \tag{A.8}$$

Eq. (A.8) is written for particle i as

$$p_i^{n+1} = \frac{B_i + \sum_{j=1}^{N} A_{ij} p_j^{n+1}}{\sum_{j=1}^{N} A_{ij}}, \tag{A.9}$$

with

$$A_{ij} = \frac{m_j^n}{\epsilon_j^* \rho_i^n \rho_j^n} \frac{\left(\epsilon_i^* + \epsilon_j^*\right) \vec{x}_{ij}^* \cdot \nabla_i W_{ij}^*}{|\vec{x}_{ij}^*|^2 + \eta^2}, \tag{A.10}$$

and

$$B_i = \left(\frac{\nabla \cdot \vec{u}^* + \Gamma}{\Delta t} \right)_i. \tag{A.11}$$

Eq. (A.9) is explicitly solved with an approximation that has been proven to lead to satisfactory results in flow in porous media [12] as well as other applications [21, 27]. It is assumed that the value of p_j^{n+1} on the right hand side of Eq. (A.9) is equal to p_j^n; this is a reasonable assumption as the time step is set to a sufficiently small value. In addition, the pressure field in the cases studied here does not change considerably. The pressure of each particle is thus approximated explicitly as

$$p_i^{n+1} = \frac{B_i + \sum_{j=1}^{N} A_{ij} p_j^n}{\sum_{j=1}^{N} A_{ij}}. \tag{A.12}$$

The pressure of free surface particles are set to zero. The calculated pressure values are used to calculate the pressure gradient as

$$\left(\frac{\epsilon^*}{\rho^n} \nabla p^{n+1} \right)_i = \epsilon_i^* \sum_{j=1}^{N} \frac{m_j^n}{\epsilon_j^*} \left(\frac{p_i^{n+1}}{\rho_i^{n2}} + \frac{p_j^{n+1}}{\rho_j^{n2}} \right) \nabla_i W_{ij}^*. \tag{A.13}$$

Afterwards, the velocity field at the new time step is calculated using Eq. (A.4).

The new position is calculated as

$$\vec{x}_i^{n+1} = \vec{x}_i^n + \frac{\left(\frac{\vec{u}_i^n}{\epsilon_i^n}\right) + \left(\frac{\vec{u}_i^{n+1}}{\epsilon_i^*}\right)}{2}\Delta t, \tag{A.14}$$

and new particle porosity, ϵ^{n+1}, is assigned. The particle concentration is calculated using Eq. (3) as

$$C_i^{n+1} = C_i^n + \left(\nabla \cdot \left(\mathcal{D}_d^{n+1}\nabla C\right)\right)_i \Delta t, \tag{A.15}$$

where the effective dispersion matrix, $\mathcal{D}_d$, is determined as [33]

$$\mathcal{D}_{di}^{n+1} = \mathcal{D}_{ei}^{n+1} I + d_{ti}|\vec{u}_i^{n+1}|I + (d_{li} - d_{ti})\frac{\vec{u}_i^{n+1} \otimes \vec{u}_i^{n+1T}}{|\vec{u}_i^{n+1}|}, \tag{A.16}$$

where d_l and d_t are longitudinal and transversal dispersivity, I is identity matrix of size 2, and $\mathcal{D}_e$ is effective diffusivity coefficient. In a saturated porous medium, $\mathcal{D}_e$ can be written as as [34]

$$\mathcal{D}_{ei}^{n+1} = D_{mi} \times (\epsilon_i^{n+1})^{4/3}, \tag{A.17}$$

where D_m is the coefficient of molecular diffusivity.

$\mathcal{D}_d$ in Eq. (A.16) is a non-diagonal matrix leading to complications with the SPH approximation [20]. To simplify the approximation procedure, $\mathcal{D}_d$ is reasonably assumed to be a diagonal matrix. The contribution of terms associated with non-diagonal elements of the dispersion matrix in Eq. (A.16) were checked in one time step and was found to be nearly three times smaller

than the contribution of the diagonal elements in the cases studied here. The variation of concentration is approximated as [20]

$$\left(\nabla \cdot (\mathcal{D}_d{}^{n+1} \nabla C)\right)_i = 2 \sum_{j=1}^{N} \frac{m_j^n}{\epsilon_j^{n+1} \rho_j^n} \left(\frac{e_{ij,1}^2}{\bar{\mathcal{D}}_{dij,11}^{n+1}} + \frac{e_{ij,2}^2}{\bar{\mathcal{D}}_{dij,22}^{n+1}} \right)^{-1} \frac{\vec{x}_{ij}^{n+1} \cdot \nabla_i W_{ij}^*}{|\vec{x}_{ij}^{n+1}|^2 + \eta^2} (C_i^n - C_j^n), \tag{A.18}$$

where $e_{ij} = \vec{x}_{ij}/|\vec{x}_{ij}|$ is the unit vector from i to j, and $\bar{\mathcal{D}}_{dij}$ is the average of the elements in the effective dispersion matrices of particles i and j. Afterwards, the particles density and mass are calculated as [35]

$$\rho_i^{n+1} = C_i^{n+1}(\rho_s - \rho_f) + 0.5(\rho_s + \rho_f), \tag{A.19}$$

$$m_i^{n+1} = \rho_i^{n+1} V_{pi}^{n+1}, \tag{A.20}$$

where V_p is volume of fluid a particle carries and is equal to $V_p = m_j/\rho_j$.

The time step value, Δt, is defined to satisfy the Courant stability and viscous diffusion conditions as

$$\Delta t \leq min(\Delta t_{CFL}, \Delta t_{visc}), \tag{A.21}$$

with

$$\Delta t_{CFL} \leq 0.25 \frac{h}{u_{max}}, \tag{A.22}$$

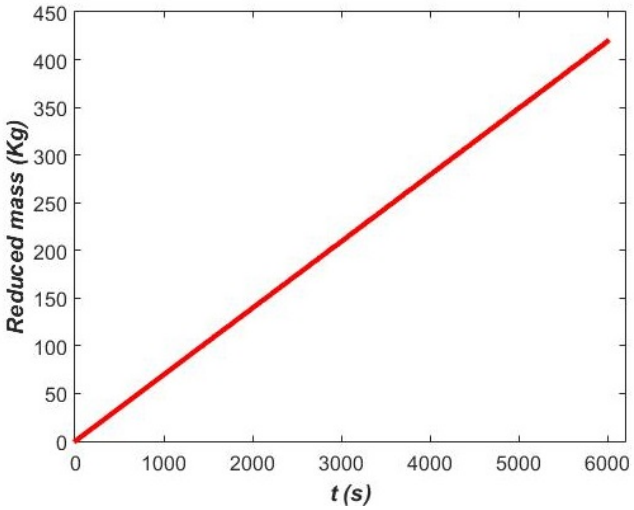

Figure B.9: Total mass reduction as a function of time using *CMR*, chapter 5, section 3.2.

and

$$\Delta t_{visc} \leq 0.125 \frac{h^2}{\nu}, \tag{A.23}$$

where ν is the kinematic viscosity and u_{max} is the maximum velocity predicted in the computations [36].

Appendix B. Mass reduction calculations in CMR

In *CMR*, mass of a sink particle is continuously reduced until it approaches zero (below 1% of its initial mass) and it is deleted. Total mass to be removed corresponds to Q_p (sink rate) and can be calculated as $\rho \times Q_p \times t$ at any time. Therefore, total mass to be removed in 100 minutes can be calculated as $\rho \times Q_p \times t = 998 \times 7 \times 10^{-5} \times 6000 = 419.2$ kg.

The total reduced mass in *CMR* was recorded and is presented in Fig. B.9

In addition to the reduced total mass, the mass of a sink particle was also tracked during a simulation before it was deleted. Fig. B.10 shows the time

evolution of mass of a sink particle. According to the method *CMR*, mass of a sink particle is reduced until it drops below the cut off value (0.01 m_0). The initial mass of one particle in the simulation in section 3.2 of chapter 5 was set to 0.02495 kg. As observed in Fig. B.10, the mass of the particle drops until it nearly approaches zero. The slope of the line is not straight because the number of sink particles at each time step differs; this is due to the movement of particles toward the sink point. As explained in section 3.8.3 and Fig 3.13 in Chapter 3, the total mass to be reduced at each time step is divided evenly among the sink particles. Therefore, if the number of the sink particles is different, the amount of the mass that is reduced from each particle is expected to vary at each time step. For the specific particle investigated here, the average of number of sink particles during 10.7 s was approximately 30. The following calculations show that the mass reduced from the particle corresponds to the sink rate.

Total mass removed in 10.7 s is

$\rho \times Q_p \times t = 998 \times 7 \times 10^{-5} \times 10.7 = 0.7475$ kg.

The specific particle investigated here was deleted after 10.7 s. In *CMR* total mass required to be reduced at each time step is divided evenly among the sink particles; therefore, the total mass (0.7475 kg) divided by 30 should be approximately equal to the initial mass of the sink particle.

$0.7475/30 = 0.024792$ kg.

References

[1] A. D. Werner, M. Bakker, V. E. Post, A. Vandenbohede, C. Lu, B. Ataie-Ashtiani, C. T. Simmons, D. A. Barry, Seawater intrusion processes, investigation and management: recent advances and future challenges, Advances in Water Resources 51 (2013) 3–26.

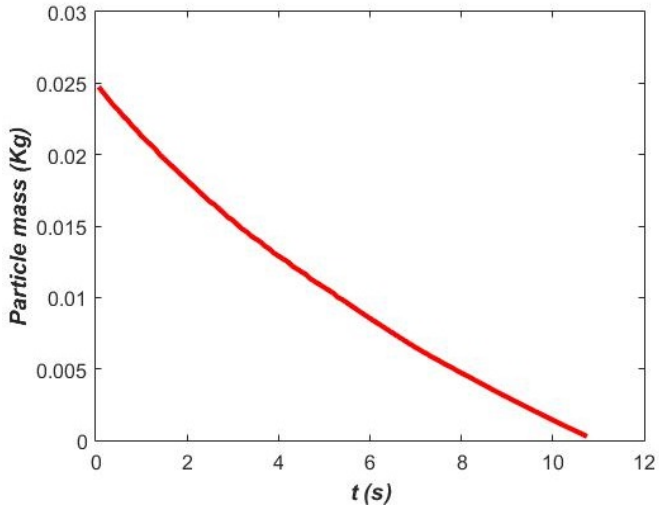

Figure B.10: Time evolution of mass of a sink particle in method CMR, chapter 5, section 3.2.

[2] E. Bertorelle, Laboratory experiments on the saltwater intrusion process, University of Padua, 2014.

[3] L. Stoeckl, G. Houben, Flow dynamics and age stratification of freshwater lenses: Experiments and modeling, Journal of Hydrology 458 (2012) 9–15.

[4] L. Stoeckl, M. Walther, T. Graf, A new numerical benchmark of a freshwater lens, Water Resources Research 52 (4) (2016) 2474–2489.

[5] A. D. Werner, H. K. Sharp, S. C. Galvis, V. E. Post, P. Sinclair, Hydrogeology and management of freshwater lenses on atoll islands: Review of current knowledge and research needs, Journal of Hydrology 551 (2017) 819–844.

[6] I. White, Fresh groundwater lens recharge, Bonriki, Kiribati, Paris: UNESCO, 1996.

[7] H. Vacher, Dupuit-ghyben-herzberg analysis of strip-island lenses, Geological Society of America Bulletin 100 (4) (1988) 580–591.

[8] C. Fetter, Position of the saline water interface beneath oceanic islands, Water Resources Research 8 (5) (1972) 1307–1315.

[9] G. Dagan, J. Bear, Solving the problem of local interface upconing in a coastal aquifer by the method of small perturbations, Journal of Hydraulic Research 6 (1) (1968) 15–44.

[10] C. I. Voss, A. M. Provost, G. S. (U.S.), Sutra, a model for saturated-unsaturated, variable-density ground-water flow with solute or energy transport, U.S. Dept. of the Interior, U.S. Geological Survey Reston, Va.

[11] C. D. Langevin, D. T. Thorne Jr, A. M. Dausman, M. C. Sukop, W. Guo, Seawat version 4: a computer program for simulation of multi-species solute and heat transport, Tech. rep., Geological Survey (US) (2008).

[12] H. Basser, M. Rudman, E. Daly, SPH modelling of multi-fluid lock-exchange over and within porous media, Advances in Water Resources 108 (2017) 15–28.

[13] G. Pahar, A. Dhar, On modification of pressure gradient operator in integrated ISPH for multifluid and porous media flow with free-surface, Engineering Analysis with Boundary Elements 80 (2017) 38–48.

[14] J. Bear, Y. Bachmat, Introduction to modeling of transport phenomena in porous media, Vol. 4, Springer Science & Business Media, 2012.

[15] J. J. Monaghan, Smoothed Particle Hydrodynamics, Annual Review of Astronomy and Astrophysics 30 (1992) 543–574.

[16] J. J. Monaghan, Simulating free surface flows with SPH, Journal of Computational Physics 110 (2) (1994) 399–406.

[17] J. Monaghan, Smoothed Particle Hydrodynamics and its diverse applications, Annual Review of Fluid Mechanics 44 (2012) 323–346.

[18] G. Pahar, A. Dhar, Modeling free-surface flow in porous media with modified incompressible SPH, Engineering Analysis with Boundary Elements 68 (2016) 75–85.

[19] J. J. Monaghan, Smoothed particle hydrodynamics, Reports on Progress in Physics 68 (8) (2005) 1703.

[20] T. Tran-Duc, E. Bertevas, N. Phan-Thien, B. C. Khoo, Simulation of anisotropic diffusion processes in fluids with smoothed particle hydrodynamics, International Journal for Numerical Methods in Fluids 82 (11) (2016) 730–747.

[21] Nomeritae, E. Daly, S. Grimaldi, H. H. Bui, Explicit incompressible SPH algorithm for free-surface flow modelling: A comparison with weakly compressible schemes, Advances in Water Resources 97 (2016) 156–167.

[22] J. J. Monaghan, H. E. Huppert, M. G. Worster, Solidification using smoothed particle hydrodynamics, Journal of Computational Physics 206 (2) (2005) 684–705.

[23] D. J. Price, J. Monaghan, Smoothed particle magnetohydrodynamics–ii. variational principles and variable smoothing-length terms, Monthly Notices of the Royal Astronomical Society 348 (1) (2004) 139–152.

[24] G.-R. Liu, M. B. Liu, Smoothed Particle Hydrodynamics: A Meshfree Particle Method, World Scientific, 2003.

[25] A. Rafiee, M. Manzari, M. Hosseini, An incompressible SPH method for simulation of unsteady viscoelastic free-surface flows, International Journal of Non-Linear Mechanics 42 (10) (2007) 1210–1223.

[26] S. Marrone, M. Antuono, A. Colagrossi, G. Colicchio, D. Le Touzé,

G. Graziani, δ-SPH model for simulating violent impact flows, Computer Methods in Applied Mechanics and Engineering 200 (13) (2011) 1526–1542.

[27] N. Nomeritae, H. H. Bui, E. Daly, Modeling transitions between free surface and pressurized flow with smoothed particle hydrodynamics, Journal of Hydraulic Engineering 144 (5).

[28] I. Federico, S. Marrone, A. Colagrossi, F. Aristodemo, M. Antuono, Simulating 2d open-channel flows through an SPH model, European Journal of Mechanics-B/Fluids 34 (2012) 35–46.

[29] A. D. Werner, D. Jakovovic, C. T. Simmons, Experimental observations of saltwater up-coning, Journal of Hydrology 373 (1) (2009) 230–241.

[30] J. Isdale, C. Spence, J. Tudhope, Physical properties of sea water solutions: viscosity, Desalination 10 (4) (1972) 319–328.

[31] D. Jakovovic, A. D. Werner, C. T. Simmons, Numerical modelling of saltwater up-coning: Comparison with experimental laboratory observations, Journal of Hydrology 402 (3) (2011) 261–273.

[32] S. J. Cummins, M. Rudman, An SPH projection method, Journal of Computational Physics 152 (2) (1999) 584–607.

[33] P. Salamon, D. Fernàndez-Garcia, J. J. Gómez-Hernández, A review and numerical assessment of the random walk particle tracking method, Journal of Contaminant Hydrology 87 (3-4) (2006) 277–305.

[34] J. Simunek, D. L. Suarez, Modeling of carbon dioxide transport and production in soil: 1. Model development, Water Resources Research 29 (2) (1993) 487–497.

[35] G. Pahar, A. Dhar, Mixed miscible-immiscible fluid flow modelling with incompressible SPH framework, Engineering Analysis with Boundary Elements 73 (2016) 50–60.

[36] J. P. Morris, P. J. Fox, Y. Zhu, Modeling low Reynolds number incompressible flows using SPH, Journal of Computational Physics 136 (1) (1997) 214–226.

5.3 Summary

In the freshwater lens formation, the qualitative and quantitative transient formation of the lens, induced by freshwater recharge, were in agreement with the experimental observations. The freshwater recharge was simulated using an inflow boundary condition.

The lens dimension as a function of recharge rate were investigated using available experimental, numerical and analytical data in literature.

For the case of salt water upconing below the extraction well, a new SPH procdeure was developed to describe a sink term to account for the freshwater extraction. Three methods were proposed and compared against the experimental observations. The flow dynamics around the sink was adjusted through changes in the source term of pressure Poisson equation.

CHAPTER 6

Conclusions

Multi-fluid flow over and within porous media occurs frequently in nature and engineering applications. Modelling of these flows are important to investigate engineering problems such as seawater intrusion in groundwater; however, this is complex due to possible travelling of the flow across media with different porosities and movement of the interface between different fluids. This study aims to improve the modelling of these flows; this is the overarching aim of this thesis. Given the presence of complex geometries and interface between different fluids and porous media, SPH was selected as the numerical method. A brief overview of the thesis is outlined in this paragraph and the detailed contributions are presented in the following paragraphs. The advantages and disadvantages of available SPH schemes in modelling fluid flow in porous media were investigated. Two schemes, i.e. Explicit Incompressible SPH (EISPH) and δ-SPH, were employed to simulate fluid flow in porous media with a spatially varying porosity. After selecting the most appropriate candidate, EISPH, the SPH scheme of flow in porous media was linked to a SPH scheme for multi-fluid flow to generate a model capable of simulating multi-fluid flow in media with porosity varying in space. The flexibility of the model to be used in practical applications, such as groundwater interaction with seawater and seawater upconing, was also tested. To address problems such as groundwater pumping, a method capable of simulating a mass sink in SPH was developed. Therefore, two key contributions of this thesis are the development of a SPH model for multi-fluid flow in porous media and an algorithm for the inclusion of sinks in SPH.

To compare the advantages and disadvantages of available SPH schemes in modelling fluid flow in porous media, EISPH and δ-SPH results were compared. A case study, i.e. an experiment of percolation of glycerine in a porous medium was used. It was found that the results associated with the kinematics of the flow, e.g. position of particles was comparable in both schemes, with EISPH resulting in pressure values closer to the theoretical values. Furthermore, as δ-SPH uses *ad-hoc* parameters in approximation of artificial viscous term and continuity equation; this was problematic as the parameters are needed to be tuned for fluids with different properties. In addition, employing a physical viscosity approximation by EISPH better takes into account the physical properties of fluids. Due to the mentioned reasons, EISPH was selected for flows of interest and were used in remainder of cases.

As mentioned earlier, multi-fluid flow across media with different porosities occurs in variety of engineering applications. EISPH was employed and validated to simulate multi-fluid flows in media with a spatially varying porosity. Experimental case studies were used to validate the model; something which is not often done at a quantitative level in SPH investigations. The case studies were: percolation of a single fluid in a porous medium, gravity current over a porous medium, Boussinesq lock-exchange over both an impermeable bed and a porous medium.

Two different time integration schemes were applied in the validation stage to investigate a possible effect of integration methods. The schemes included first order in time for velocity and second order in time for position (Euler) and second order in time for both velocity and position (Heun). The results of the two integration methods were comparable in the first two cases, likely due to the small time steps used. Therefore, the Euler method was employed in remainder of the cases due to the lower computational cost.

The comparison of the results of the first two cases with experimentally observed data showed the credibility of the model in reproducing pressure field and transient movement of the fluids in the porous media. The EISPH reproduced a smooth pressure field and the quantitative values of the simulated pressure well agreed with pressure values obtained from experimental observations and analytical solutions. It was also found that implementing a linear transition of porosity between media improved the results in the first two cases. According to the third case, the EISPH results of the multi-fluid lock-exchange flow over the impermeable bed were qualitatively comparable to the experimental data so that the Kelvin-Helmholtz instabilities were captured in the simulated current. The quantitative results, the position of the intruding current,

was also well agreed with the observed data. It was found that the boundary conditions had significant effect on the accuracy of the results, so that implementing the modified no-slip boundary condition, reproduced more accurate current velocity compared to the conventional no-slip boundary conditions. In the fourth case, a multi-fluid flow over and within a porous medium was simulated and tested successfully for the first time against experimental data. The qualitative behaviour of the current over and within the porous medium was well captured using the EISPH scheme. It was also found that using a high order kernel, quintic spline, reproduced the Kelvin-Helmholtz instabilities, while they were not reproduced using a cubic spline kernel. The quantitative investigation showed that using the linear transition layer at porous boundary was problematic in the fourth case; therefore, the modelling of the flow at the transition requires further study. A kernel with variable smoothing length, changing with porosity, was also tested for the fourth case that led to improvement of the results; this was due to the maintaining constant number of particles within support of the kernel function throughout the domain. A sensitivity analysis was performed for the model parameter, Forchheimer coefficient. Using different values of the parameter led to expected changes in the results; however, this showed the importance of selecting appropriate parameters such as Forchheimer coefficient, permeability and diffusion coefficients to reproduce experimental results. This usually seems to be an issue in other SPH studies that employ *ad hoc* values for parameters.

After validating the EISPH code, the scheme was used to investigate the flexibility of the model to be applied in practical problems. The cases simulated were the dynamics of a buoyant freshwater lens over seawater in islands and salt water upconing caused by pumping.

In the case of the freshwater lens, the model well reproduced the transient thickness and maximum depth of the experimental lenses. Furthermore, the ability of the model in reproducing the simulated maximum depth of the lens as a function of different recharge rates were successfully tested against observed, analytical and other numerical results. It was found that the simulated lens dimensions depended on the thickness of the inflow zone, as this controlled the value of hydrostatic pressure acting on the surface of the island. The best inflow thickness, to reproduce the lens dimensions, was found to be equal to the radius of the support domain of the kernel function.

In the case of the upconing induced by pumping, a new procedure was developed to implement a sink term. The procedure was consisted of two main steps; making the particles surrounding a sink point move toward it and delete mass of fluid due to the

pumping. To induce the movement of the particles toward a sink point, the divergence of the velocity for the particles in the vicinity of the sink point was adjusted in accordance with the pumping rate in the pressure Poisson equation. To delete the mass, three different methods indicated as *SPR*, *MRPR*, and *CMR* were developed. *SPR*, where the mass reduction is handled solely through removal of particles, appeared to reproduce better results compared to experimental observations.

The results of this study show the effectiveness of the EISPH scheme in simulating multi-fluid flow in porous media. The study also lay a foundation to for the inclusion of mass sink in SPH and facilitates applying SPH in problems associated with pumping.

6.1 Thesis limitations

The limitations of this study are

1. *High computational time.* Although, SPH is advantageous in the problems associated with free surfaces and multi-fluid flows, its high computational time is one of its main drawbacks, as variables on each particle are calculated via interpolation from surrounding particles. Due to the larger computational time, it was necessary to focus on problems that require relatively small number of particles. Therefore, the case studies were only limited to the laboratory scale experiments. Furthermore, the CPU time of the simulated experiments, in some cases, were relatively long; this caused long waiting time to analyse the results. This limitation can be ameliorated with a parallel version of the code.

2. *Insufficiency of details of the experiments found in the literature.* Although many experiments were found in the literature, only few presented enough details about how the experiments were carried out, to be successfully used in this study. For instance, values of Forchheimer coefficient, in modelling flow in porous media, is usually assumed in literature.

3. *Simulating the interface between media with different porosities.* Although using variable smoothing length, changing with porosity, provided sufficiently reasonable results, this requires future study. The problem occurs due to the irregular distribution of particles inside a kernel located at the interface. The kernel's support domain at the interface sits between different media, with different numbers of particles belonging to the media. This causes an error in the calculation of the summation of the kernel function and its derivative.

4. *Simulation of the salt water upconing under a pumping well.* This phenomenon naturally occurs in cylindrical coordinates and an SPH model in cylindrical framework

is recommended to be used. Therefore, an experiment was selected with nearly two dimensional nature. Further study is required to investigate the sink simulation with an SPH model in cylindrical framework, as analytical solutions have been mostly presented in cylindrical coordinates.

6.2 Future works

6.2.1 Interface between media with different porosities

Further development is recommended to improve the modelling of the interface between media with different porosities. The problem occurs because there is a jump in the number density of particles at the interface. This happens because the distance between particles is inversely proportional to porosity of media and the numbers of particles inside the kernel that belong to different media are thus different.

To show this problem, two simulations are presented here. A set of particles that are fixed at their positions were used to calculate the summation of the kernel at each particle as

$$W_s = \sum_{j=1}^{N} \frac{m_j}{\epsilon_j \rho_j} W_{ij}, \tag{6.1}$$

where m_j, ρ_j, and ϵ_j are mass, density, and porosity of particle j, respectively, and W_{ij} is the kernel value associated with particles i and j. The cubic spline weighting function was used here (*Liu and Liu*, 2003).

In the simulations a set of particles fixed in their positions inside a square box were simulated. The left half of the domain was set to have $\epsilon = 1$, and the right half was a porous medium with $\epsilon = 0.5$. The distance between particles on the left was $\Delta x_f = \Delta y_f = \frac{L}{42}$, and inside the porous medium was $\Delta x_p = \Delta y_p = \frac{L}{42\sqrt{\epsilon}}$. Two scenarios were simulated, 1) one with constant smoothing length (Fig. 6.1a) and one with variable smoothing length (Fig. 6.1b). For the first scenario the smoothing length was set to $h = 1.2\Delta x_f$ for all the particles, while for the latter the smoothing length was set to $h = 1.2\Delta x_p$.

As it is observed in Fig. 6.1a, the kernel summation value in the two domains is not constant throughout the domain. This is because the number of particles inside the support domain of the kernel in the porous medium is not sufficient. This issue was observed in the second scenario (Fig. 6.1b) with a less extent where the smoothing length

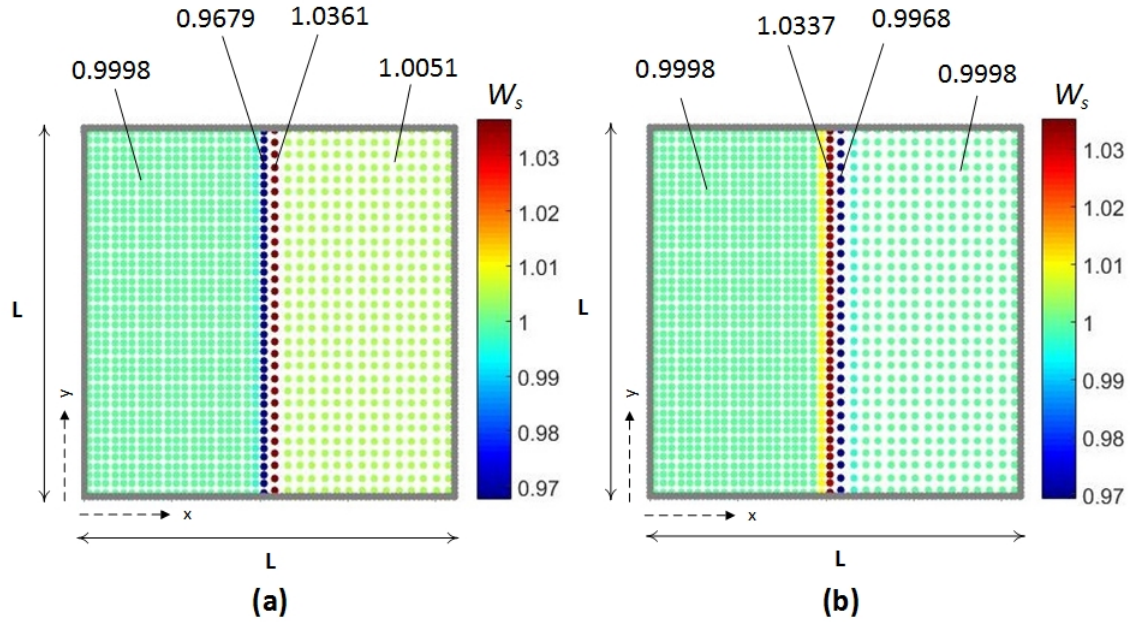

Figure 6.1: Kernel function summation (W_s) for the scenario with (a) constant smoothing length, (b) variable smoothing length.

was assigned according to the porosity of the media and the number of particles inside the support domain was constant in the whole domain except at the interface.

For both cases, and for the particles close to the interface, it is observed that the value of the summation was not accurately approximated. The reason for this is the irregular distribution of particles inside a support domain of the kernel that falls over the interface. This error occurs across a wider region in the second scenario (Fig. 6.1b). Because the same value of smoothing length should be used for a pair of interacting particles to conserve the momentum, the effective smoothing length for a pair of interacting particles was calculated as the average of their smoothing lengths (*Rafiee et al.*, 2007). This especially is necessary for the particles at the interface between two media. The averaging caused the particles on the left close to the interface to have a larger support domain compared to the other particles on the left. This led to the inclusion of more particles from the porous medium inside the support domain; that possibly is the reason for the error in more layers in the second scenario.

It can be concluded from the simulations that using a variable smoothing length increases the accuracy of the results by assuring sufficient number of particles inside a support domain. However, the error at the interface requires further study and improvement.

6.2.2 Sink simulations

In coastal aquifers, when a larger amount of groundwater is abstracted through a pumping well, seawater upconing can dramatically pollute drinking water. Although many modelling and experimental studies have focused on studying the seawater upconing, the SPH modelling of this phenomenon has not been conducted in the literature. Due to the advantage of SPH in modelling multi-fluid flow with complex geometries and ease of adding new physics, it is beneficial to further study the SPH modelling of seawater upconing.

It is recommended to further investigate the particle distribution around a point sink. Although, the observed clumping of particles around a point sink was expected due to the constant reduction of the sink particles' mass while keeping density constant, it is beneficial to investigate the effect of particle regularisation techniques such as Particle Shifting (PS) and Dynamic Stabilization (DS) on improvement of the results (*Lind et al.*, 2012; *Tsuruta et al.*, 2013; *Khayyer et al.*, 2017b).

It is recommended to further investigate the modelling of the point sink using cylindrical SPH as the flow pattern especially around the sink is cylindrical. The study can be started by simulating the simple hydrodynamic problem of a point sink as shown in Fig. 6.2. The analytical radial velocity of the fluid moving toward the origin is

$$u_r = \frac{q}{2\pi r}, \tag{6.2}$$

where u_r is the radial velocity, q is the flow rate or the sink intensity per unit thickness, and r is the radial distance from the sink (*Nakayama*, 2018). The tangential velocity, u_θ, is zero in this case.

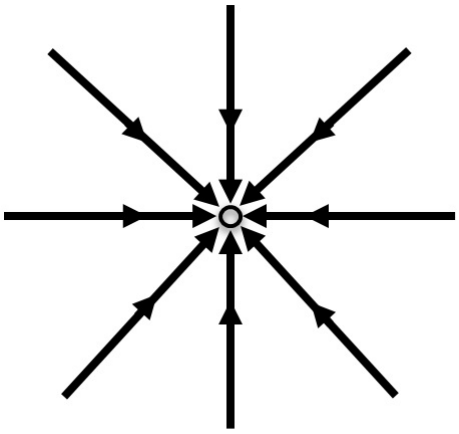

Figure 6.2: A sink at the origin (*Nakayama*, 2018).

Bibliography

Acton, J. M., H. E. Huppert, and M. G. Worster (2001), Two-dimensional viscous gravity currents flowing over a deep porous medium, *Journal of Fluid Mechanics*, *440*, 359–380.

Adduce, C., G. Sciortino, and S. Proietti (2011), Gravity currents produced by lock exchanges: experiments and simulations with a two-layer shallow-water model with entrainment, *Journal of Hydraulic Engineering*, *138*(2), 111–121.

Akbari, H. (2014), Modified moving particle method for modeling wave interaction with multi layered porous structures, *Coastal Engineering*, *89*, 1–19.

Akbari, H., and M. M. Namin (2013), Moving particle method for modeling wave interaction with porous structures, *Coastal Engineering*, *74*, 59–73.

Aly, A. M., and M. Asai (2015), Three-dimensional incompressible smoothed particle hydrodynamics for simulating fluid flows through porous structures, *Transport in Porous Media*, *110*(3), 483–502.

Antuono, M., A. Colagrossi, S. Marrone, and D. Molteni (2010), Free-surface flows solved by means of SPH schemes with numerical diffusive terms, *Computer Physics Communications*, *181*(3), 532–549.

Association, G. P., et al. (1963), *Physical properties of glycerine and its solutions*, Glycerine Producers Association.

Barcarolo, D. A. (2013), Improvement of the precision and the efficiency of the SPH method: theoretical and numerical study, Ph.D. thesis, Ecole Centrale de Nantes (ECN), Nantes, France.

Bear, J. (2013), *Dynamics of fluids in porous media*, Courier Corporation.

Bear, J., and Y. Bachmat (2012), *Introduction to modeling of transport phenomena in porous media*, vol. 4, Springer Science & Business Media.

Beavers, G. S., and D. D. Joseph (1967), Boundary conditions at a naturally permeable wall, *Journal of fluid mechanics*, *30*(1), 197–207.

Birman, V., and E. Meiburg (2006), High-resolution simulations of gravity currents, *Journal of the Brazilian Society of Mechanical Sciences and Engineering*, *28*(2), 169–173.

Birman, V., J. Martin, and E. Meiburg (2005), The non-boussinesq lock-exchange problem. part 2. high-resolution simulations, *Journal of Fluid Mechanics*, *537*, 125–144.

Bonometti, T., and S. Balachandar (2008), Effect of schmidt number on the structure and propagation of density currents, *Theoretical and Computational Fluid Dynamics*, *22*(5), 341.

Brennen, C. E., and C. E. Brennen (2005), *Fundamentals of Multiphase Flow*, Cambridge university press.

Britter, R., and P. Linden (1980), The motion of the front of a gravity current travelling down an incline, *Journal of Fluid Mechanics*, *99*(3), 531–543.

Bui, H. H., and G. D. Nguyen (2017), A coupled fluid-solid sph approach to modelling flow through deformable porous media, *International Journal of Solids and Structures*, *125*, 244–264.

Bui, H. H., K. Sako, and R. Fukagawa (2007), Numerical simulation of soil–water interaction using smoothed particle hydrodynamics (sph) method, *Journal of Terramechanics*, *44*(5), 339–346.

Bui, H. H., R. Fukagawa, K. Sako, and S. Ohno (2008), Lagrangian meshfree particles method (SPH) for large deformation and failure flows of geomaterial using elastic–plastic soil constitutive model, *International Journal for Numerical and Analytical Methods in Geomechanics*, *32*(12), 1537–1570.

Coutinho, B. G., F. Marcondes, and A. G. B. de Lima (2008), Numerical simulation of oil recovery through water flooding in petroleum reservoir using boundary-fitted coordinates, *International Journal of Modeling and Simulation for the Petroleum Industry*, *2*(1), 17–34.

Cummins, S. J., and M. Rudman (1999), An SPH projection method, *Journal of Computational Physics*, *152*(2), 584–607.

Dalrymple, R., and B. Rogers (2006), Numerical modeling of water waves with the SPH method, *Coastal engineering*, *53*(2), 141–147.

del Jesus, M. (2011), Three-dimensional interaction of water waves with coastal structures, Ph.D. thesis, Ph. D. thesis. Universidad de Cantabria, Santander (Spain).

Del Jesus, M., J. L. Lara, and I. J. Losada (2012), Three-dimensional interaction of waves and porous coastal structures: Part i: Numerical model formulation, *Coastal Engineering*, *64*, 57–72.

Duman, T., and U. Shavit (2010), A solution of the laminar flow for a gradual transition between porous and fluid domains, *Water Resources Research*, *46*(9).

Étienne, J., E. J. Hopfinger, and P. Saramito (2005), Numerical simulations of high density ratio lock-exchange flows, *Physics of Fluids*, *17*(3), 036,601.

Federico, I., S. Marrone, A. Colagrossi, F. Aristodemo, and M. Antuono (2012), Simulating 2D open-channel flows through an SPH model, *European Journal of Mechanics-B/Fluids*, *34*, 35–46.

Firoozabadi, B., M. Mahdinia, et al. (2013), 2d numerical simulation of density currents using the sph projection method, *European Journal of Mechanics-B/Fluids*, *38*, 38–46.

Ghasemi, A., B. Firoozabadi, M. Mahdinia, et al. (2013), 2d numerical simulation of density currents using the SPH projection method, *European Journal of Mechanics-B/Fluids*, *38*, 38–46.

Gingold, R. A., and J. J. Monaghan (1977), Smoothed particle hydrodynamics: theory and application to non-spherical stars, *Monthly notices of the Royal Astronomical Society*, *181*(3), 375–389.

Gobin, D., B. Goyeau, and A. Neculae (2005), Convective heat and solute transfer in partially porous cavities, *International Journal of Heat and Mass Transfer*, *48*(10), 1898–1908.

Goharzadeh, A., A. Saidi, D. Wang, W. Merzkirc, and A. Khalil (2006), An experimental investigation of the brinkman layer thickness at a fluid-porous interface, in *IUTAM symposium on one hundred years of boundary layer research*, pp. 445–454, Springer.

Goyeau, B., D. Lhuillier, D. Gobin, and M. Velarde (2003), Momentum transport at a fluid-porous interface, *International Journal of Heat and Mass Transfer*, *46*(21), 4071–4081.

Grabe, J., and B. Stefanova (2014), Numerical modeling of saturated soils, based on smoothed particle hydrodynamics (sph), *geotechnik*, *37*(3), 191–197.

Grenier, N., D. Le Touzé, A. Colagrossi, M. Antuono, and G. Colicchio (2013), Viscous bubbly flows simulation with an interface sph model, *Ocean Engineering*, *69*, 88–102.

Hosseini, S., M. Manzari, and S. Hannani (2007), A fully explicit three-step SPH algorithm for simulation of non-Newtonian fluid flow, *International Journal of Numerical Methods for Heat & Fluid Flow*, *17*(7), 715–735.

Hu, K. C., S. C. Hsiao, H. H. Hwung, and T. R. Wu (2012), Three-dimensional numerical modeling of the interaction of dam-break waves and porous media, *Advances in Water Resources*, *47*, 14–30.

Huppert, H. E. (2006), Gravity currents: a personal perspective, *Journal of Fluid Mechanics*, *554*, 299–322.

Jiang, F., M. S. Oliveira, and A. C. Sousa (2007), Mesoscale sph modeling of fluid flow in isotropic porous media, *Computer Physics Communications*, *176*(7), 471–480.

Joseph, D., D. Nield, and G. Papanicolaou (1982), Nonlinear equation governing flow in a saturated porous medium, *Water Resour. Res*, *18*(4), 1049–1052.

Khayyer, A., H. Gotoh, Y. Shimizu, and K. Gotoh (2017a), On enhancement of energy conservation properties of projection-based particle methods, *European Journal of Mechanics-B/Fluids*, *66*, 20–37.

Khayyer, A., H. Gotoh, and Y. Shimizu (2017b), Comparative study on accuracy and conservation properties of two particle regularization schemes and proposal of an optimized particle shifting scheme in isph context, *Journal of Computational Physics*, *332*, 236–256.

Khayyer, A., H. Gotoh, Y. Shimizu, K. Gotoh, H. Falahaty, and S. Shao (2018), Development of a projection-based sph method for numerical wave flume with porous media of variable porosity, *Coastal Engineering*, *140*, 1–22.

Kothe, D., M. Williams, K. Lam, D. Korzekwa, P. Tubesing, and E. Puckett (1999), A second-order accurate, linearity-preserving volume tracking algorithm for free surface flows on 3-d unstructured meshes, in *Proceedings of the 3rd ASME/JSME Joint Fluids Engineering Conference, San Francisco, CA*, pp. 1–6, Citeseer.

Langevin, C. D., D. T. Thorne Jr, A. M. Dausman, M. C. Sukop, and W. Guo (2008), Seawat version 4: a computer program for simulation of multi-species solute and heat transport, *Tech. rep.*, Geological Survey (US).

Leroy, A., D. Violeau, M. Ferrand, and A. Joly (2015), Buoyancy modelling with incompressible sph for laminar and turbulent flows, *International Journal for Numerical Methods in Fluids*, *78*(8), 455–474.

Li, Y., J. Xu, and D. Li (2010), Molecular dynamics simulation of nanoscale liquid flows, *Microfluidics and nanofluidics*, *9*(6), 1011–1031.

Lind, S., R. Xu, P. Stansby, and B. D. Rogers (2012), Incompressible smoothed particle hydrodynamics for free-surface flows: A generalised diffusion-based algorithm for stability and validations for impulsive flows and propagating waves, *Journal of Computational Physics*, *231*(4), 1499–1523.

Liu, G.-R., and M. B. Liu (2003), *Smoothed Particle Hydrodynamics: A Meshfree Particle Method*, World Scientific.

Lowe, R. J., J. W. Rottman, and P. Linden (2005), The non-boussinesq lock-exchange problem. part 1. theory and experiments, *Journal of Fluid Mechanics*, *537*, 101–124.

Lucy, L. B. (1977), A numerical approach to the testing of the fission hypothesis, *The Astronomical Journal*, *82*, 1013–1024.

Marrone, S., M. Antuono, A. Colagrossi, G. Colicchio, D. Le Touzé, and G. Graziani (2011), δ-SPH model for simulating violent impact flows, *Computer Methods in Applied Mechanics and Engineering*, *200*(13), 1526–1542.

Marrone, S., A. Colagrossi, M. Antuono, G. Colicchio, and G. Graziani (2013), An accurate SPH modeling of viscous flows around bodies at low and moderate reynolds numbers, *Journal of Computational Physics*, *245*, 456–475.

Meiburg, E., S. Radhakrishnan, and M. Nasr-Azadani (2015), Modeling gravity and turbidity currents: computational approaches and challenges, *Applied Mechanics Reviews*, *67*(4), 040,802.

Molteni, D., and A. Colagrossi (2009), A simple procedure to improve the pressure evaluation in hydrodynamic context using the SPH, *Computer Physics Communications*, *180*(6), 861–872.

Monaghan, J., R. Cas, A. Kos, and M. Hallworth (1999), Gravity currents descending a ramp in a stratified tank, *Journal of Fluid Mechanics*, *379*, 39–69.

Monaghan, J. J. (1992), Smoothed particle hydrodynamics, *Annual Review of Astronomy and Astrophysics*, *30*(1), 543–574.

Monaghan, J. J. (1994), Simulating free surface flows with SPH, *Journal of Computational Physics*, *110*(2), 399–406.

Monaghan, J. J. (2005), Smoothed particle hydrodynamics, *Reports on Progress in Physics*, *68*(8), 1703.

Monaghan, J. J., and J. C. Lattanzio (1985), A refined particle method for astrophysical problems, *Astronomy and Astrophysics*, *149*, 135–143.

Monaghan, J. J., H. E. Huppert, and M. G. Worster (2005), Solidification using smoothed particle hydrodynamics, *Journal of Computational Physics*, *206*(2), 684–705.

Morris, J. P. (1996), *Analysis of smoothed particle hydrodynamics with applications*, Monash University Australia.

Morris, J. P., P. J. Fox, and Y. Zhu (1997), Modeling low reynolds number incompressible flows using SPH, *Journal of Computational Physics*, *136*(1), 214–226.

Nakayama, Y. (2018), *Introduction to fluid mechanics*, Butterworth-Heinemann.

Neale, G., and W. Nader (1974), Practical significance of brinkman's extension of darcy's law: coupled parallel flows within a channel and a bounding porous medium, *The Canadian Journal of Chemical Engineering*, *52*(4), 475–478.

Nield, D. (1991), The limitations of the brinkman-forchheimer equation in modeling flow in a saturated porous medium and at an interface, *International Journal of Heat and Fluid Flow*, *12*(3), 269–272.

Nield, D. A. (2000), Modelling fluid flow and heat transfer in a saturated porous medium, *Advances in Decision Sciences*, *4*(2), 165–173.

Nomeritae, E. Daly, S. Grimaldi, and H. H. Bui (2016), Explicit incompressible SPH algorithm for free-surface flow modelling: A comparison with weakly compressible schemes, *Advances in Water Resources*, *97*, 156–167.

Nomeritae, N., H. H. Bui, and E. Daly (2018), Modeling transitions between free surface and pressurized flow with smoothed particle hydrodynamics, *Journal of Hydraulic Engineering*, *144*(5), 04018,012.

Ochoa-Tapia, J. A., and S. Whitaker (1995), Momentum transfer at the boundary between a porous medium and a homogeneous fluid-I. theoretical development, *International Journal of Heat and Mass Transfer*, *38*(14), 2635–2646.

Pahar, G., and A. Dhar (2016a), Modeling free-surface flow in porous media with modified incompressible sph, *Engineering Analysis with Boundary Elements*, *68*, 75–85.

Pahar, G., and A. Dhar (2016b), A robust volume conservative divergence-free isph framework for free-surface flow problems, *Advances in water resources*, *96*, 423–437.

Pahar, G., and A. Dhar (2016c), Mixed miscible-immiscible fluid flow modelling with incompressible sph framework, *Engineering Analysis with Boundary Elements*, *73*, 50–60.

Pahar, G., and A. Dhar (2017), On modification of pressure gradient operator in integrated isph for multifluid and porous media flow with free-surface, *Engineering Analysis with Boundary Elements*, *80*, 38–48.

Panah, M., and F. Blanchette (2018), Simulating flow over and through porous media with application to erosion of particulate deposits, *Computers & Fluids*, *166*, 9–23.

Park, J. S., S. M. Kim, M. S. Kim, and W. I. Lee (2005), Finite element analysis of flow and heat transfer with moving free surface using fixed grid system, *International Journal of Computational Fluid Dynamics*, *19*(3), 263–276.

Peng, C., G. Xu, W. Wu, H.-s. Yu, and C. Wang (2017), Multiphase sph modeling of free surface flow in porous media with variable porosity, *Computers and Geotechnics*, *81*, 239–248.

Price, D. J., and J. Monaghan (2004), Smoothed particle magnetohydrodynamics–ii. variational principles and variable smoothing-length terms, *Monthly Notices of the Royal Astronomical Society*, *348*(1), 139–152.

Raeini, A. Q., M. J. Blunt, and B. Bijeljic (2012), Modelling two-phase flow in porous media at the pore scale using the volume-of-fluid method, *Journal of Computational Physics*, *231*(17), 5653–5668.

Rafiee, A., and K. P. Thiagarajan (2009), An SPH projection method for simulating fluid-hypoelastic structure interaction, *Computer Methods in Applied Mechanics and Engineering*, *198*(33), 2785–2795.

Rafiee, A., M. Manzari, and M. Hosseini (2007), An incompressible sph method for simulation of unsteady viscoelastic free-surface flows, *International Journal of Non-Linear Mechanics*, *42*(10), 1210–1223.

Ren, B., H. Wen, P. Dong, and Y. Wang (2016), Improved sph simulation of wave motions and turbulent flows through porous media, *Coastal Engineering*, *107*, 14–27.

Richardson, S. (1971), A model for the boundary condition of a porous material. part 2, *Journal of Fluid Mechanics*, *49*(2), 327–336.

Rottman, J. W., and J. E. Simpson (1983), Gravity currents produced by instantaneous releases of a heavy fluid in a rectangular channel, *Journal of Fluid Mechanics*, *135*, 95–110.

Rotunno, R., J. Klemp, G. Bryan, and D. Muraki (2011), Models of non-boussinesq lock-exchange flow, *Journal of Fluid Mechanics*, *675*, 1–26.

Salamon, P., D. Fernàndez-Garcia, and J. J. Gómez-Hernández (2006), A review and numerical assessment of the random walk particle tracking method, *Journal of contaminant hydrology*, *87*(3-4), 277–305.

Scarselli, D. (2013), Non modal stability of laminar channel flow over porous walls.

Serchi, F. G., J. Peakall, D. Ingham, and A. Burns (2012), A numerical study of the triggering mechanism of a lock-release density current, *European Journal of Mechanics-B/Fluids*, *33*, 25–39.

Shao, S. (2010), Incompressible SPH flow model for wave interactions with porous media, *Coastal Engineering*, *57*(3), 304–316.

Shao, S. (2012), Incompressible smoothed particle hydrodynamics simulation of multifluid flows, *International Journal for Numerical Methods in Fluids*, *69*(11), 1715–1735.

Shao, S., and E. Y. Lo (2003), Incompressible SPH method for simulating Newtonian and non-Newtonian flows with a free surface, *Advances in Water Resources*, *26*(7), 787–800.

Shobeyri, G., and M. Afshar (2010), Simulating free surface problems using discrete least squares meshless method, *Computers & Fluids*, *39*(3), 461–470.

Simpson, J. E. (1982), Gravity currents in the laboratory, atmosphere, and ocean, *Annual Review of Fluid Mechanics*, *14*(1), 213–234.

Simpson, J. E. (1997), *Gravity currents: In the environment and the laboratory*, Cambridge university press.

Simunek, J., and D. L. Suarez (1993), Modeling of carbon dioxide transport and production in soil: 1. Model development, *Water Resources Research*, *29*(2), 487–497.

Stoeckl, L., and G. Houben (2012), Flow dynamics and age stratification of freshwater lenses: Experiments and modeling, *Journal of hydrology*, *458*, 9–15.

Stoeckl, L., M. Walther, and T. Graf (2016), A new numerical benchmark of a freshwater lens, *Water Resources Research*, *52*(4), 2474–2489.

Tao, K., J. Yao, and Z. Huang (2013), Analysis of the laminar flow in a transition layer with variable permeability between a free-fluid and a porous medium, *Acta Mechanica*, *224*(9), 1943–1955.

Thomas, L., and B. Marino (2011), Inertial density currents over porous media limited by different lower boundary conditions, *Journal of Hydraulic Engineering*, *138*(2), 133–142.

Thomas, L., B. Marino, and P. Linden (2004), Lock-release inertial gravity currents over a thick porous layer, *Journal of Fluid Mechanics*, *503*, 299–319.

Tran-Duc, T., E. Bertevas, N. Phan-Thien, and B. C. Khoo (2016), Simulation of anisotropic diffusion processes in fluids with smoothed particle hydrodynamics, *International Journal for Numerical Methods in Fluids*, *82*(11), 730–747.

Tsuruta, N., A. Khayyer, and H. Gotoh (2013), A short note on dynamic stabilization of moving particle semi-implicit method, *Computers & Fluids*, *82*, 158–164.

Ungarish, M. (2007), A shallow-water model for high-reynolds-number gravity currents for a wide range of density differences and fractional depths, *Journal of Fluid Mechanics*, *579*, 373–382.

Valdés-Parada, F. J., J. A. Ochoa-Tapia, and J. Alvarez-Ramirez (2007), Diffusive mass transport in the fluid–porous medium inter-region: Closure problem solution for the one-domain approach, *Chemical Engineering Science*, *62*(21), 6054–6068.

Valdés-Parada, F. J., C. G. Aguilar-Madera, J. A. Ochoa-Tapia, and B. Goyeau (2013), Velocity and stress jump conditions between a porous medium and a fluid, *Advances in water resources*, *62*, 327–339.

Violeau, D., and B. D. Rogers (2016), Smoothed Particle Hydrodynamics (SPH) for free-surface flows: past, present and future, *Journal of Hydraulic Research*, pp. 1–26.

Voss, C. I., A. M. Provost, and G. S. (U.S.) (2008), Sutra, a model for saturated-unsaturated, variable-density ground-water flow with solute or energy transport, *U.S. Dept. of the Interior, U.S. Geological Survey Reston, Va.*

Werner, A. D., D. Jakovovic, and C. T. Simmons (2009), Experimental observations of saltwater up-coning, *Journal of Hydrology*, *373*(1-2), 230–241.

Werner, A. D., M. Bakker, V. E. Post, A. Vandenbohede, C. Lu, B. Ataie-Ashtiani, C. T. Simmons, and D. A. Barry (2013), Seawater intrusion processes, investigation and management: recent advances and future challenges, *Advances in Water Resources*, *51*, 3–26.

Werner, A. D., H. K. Sharp, S. C. Galvis, V. E. Post, and P. Sinclair (2017), Hydrogeology and management of freshwater lenses on atoll islands: Review of current knowledge and research needs, *Journal of Hydrology*, *551*, 819–844.

Whitaker, S. (1986), Flow in porous media i: A theoretical derivation of darcy's law, *Transport in porous media*, *1*(1), 3–25.

Whitaker, S. (1996), The forchheimer equation: a theoretical development, *Transport in Porous media*, *25*(1), 27–61.

Yeganeh-Bakhtiary, A., B. Shabani, H. Gotoh, and S. S. Wang (2009), A three-dimensional distinct element model for bed-load transport, *Journal of Hydraulic Research*, *47*(2), 203–212.

Zainali, A., N. Tofighi, M. S. Shadloo, and M. Yildiz (2013), Numerical investigation of newtonian and non-newtonian multiphase flows using isph method, *Computer Methods in Applied Mechanics and Engineering*, *254*, 99–113.

Zhao, B., C. W. MacMinn, M. L. Szulczewski, J. A. Neufeld, H. E. Huppert, and R. Juanes (2013), Interface pinning of immiscible gravity-exchange flows in porous media, *Physical Review E*, *87*(2), 023,015.

Zhu, Y., and P. J. Fox (2001), Smoothed particle hydrodynamics model for diffusion through porous media, *Transport in Porous Media*, *43*(3), 441–471.